8-2022

# A Bulk Driven Transimpedance CMOS Amplifier for SiPM Based Detection

Shahram Hatefi Hesari
hesari@vols.utk.edu

To the Graduate Council:

I am submitting herewith a thesis written by Shahram Hatefi Hesari entitled "A Bulk Driven Transimpedance CMOS Amplifier for SiPM Based Detection." I have examined the final electronic copy of this thesis for form and content and recommend that it be accepted in partial fulfillment of the requirements for the degree of Master of Science, with a major in Electrical Engineering.

Nicole McFarlane, Major Professor

We have read this thesis and recommend its acceptance:

Benjamin J. Blalock, Ahmedullah Aziz

Accepted for the Council:
Dixie L. Thompson

Vice Provost and Dean of the Graduate School

(Original signatures are on file with official student records.)

# A Bulk Driven Transimpedance CMOS Amplifier for SiPM Based Detection

A Thesis Presented for the

Master of Science

Degree

The University of Tennessee, Knoxville

Shahram Hatefi Hesari

August 2022

## Dedication

*To my beautiful wife, Farnaz, my family and friends.*

# Acknowledgments

I am extremely grateful to my advisor Dr. Nicole McFarlane for all of her valuable suggestions, guidance, and support during my master. I also thank Dr. Benjamin. J. Blalock and Dr. Ahmed Aziz for their help and support during my master program. I would like to thank all my labmates, including Ava Hedayatipour, Shaghayegh Aslanzadeh, Aminul Haque, Andalib Nizam, Farin Rahman, and Mattew Robert Smalley. I am also so thankful to Amine Benkechkache and Dr. Erik Lukosi for helpful discussions and sharing laboratory space.

# Abstract

The contribution of this work lies in the development of a bulk driven operational transconducctance amplifier which can be integrated with other analog circuits and photodetectors in the same chip for compactness, miniaturization and reducing the power. Silicon photomultipliers, also known as SiPMs, when coupled with scintillator materials are used in many imaging applications including nuclear detection. This thesis discuss the design of a bulk-driven transimpedance amplifier suitable for detectors where the front end is a SiPM. The amplifier was design and fabricated in a standard standard CMOS process and is suitable for integration with CMOS based SiPMs and commercially available SiPMs. Specifically, the amplifier was verified in simulations and experiment using circuit models for the SiPM.

The bulk-driven amplifier's performance, was compared to a commercially available amplifier with approximately the same open loop gain (70dB). Both amplifiers were verified with two different light sources, a scintillator and a SiPM. The energy resolution using the bulk driven amplifier was 8.6% and was 14.2% for the commercial amplifier indicating the suitability of the amplifier design for portable systems.

# Table of Contents

# List of Tables

# List of Figures

# Chapter 1

# Introduction

Today silicon photomultipliers are used in numerous applications, from environmental to science. Silicon photomultipliers, or SiPMs, are semiconductor based photodiodes that are extremely sensitive to light. With some other advantages such as immunity to magnetic field and low bias voltage, they have been used as a legitimate replacement for photomultiplier tubes (PMTs) [76, 77, 78].

SiPMs can be used as a photodetector in spectroscopic personal radiation detectors (SPRDs). SPRDs are devices defined by ANSI/IEEE N42.48 [79] and IEC 62618 [80] and are used to detect radioactive materials. SPRDs can record the gamma-ray energy spectrum and identify the isotope emitting the radiation. In addition, the SPRD neutron detection feature can help identify nuclear from other radioactive materials and naturally occuring gamma-ray sources. [81].

In this thesis, the focus is on the electronics for SiPM based nuclear readout. This specific application relies on the use of scintillators which could be, for example, LYSO (lutetium-yttrium oxyorthosilicate) coupled with custom or commercially available SiPMs. The role of a scintillator in the process is emitting the light when a particle such as gamma or neutron are incident on the scintillator surface. Depending on the SiPM type, scintillator material and application, various strategies may be employed to integrate the SiPM and scintillator. However, generally SiPMs and scintillators can be coupled with optical coupling grease. [82] provide more detail about the coupling materials. Thus, typical semiconductor based nuclear detection systems consists of a source, a scintillator that transduces the incoming particles such as neutrons and gammas to photons, a silicon photomultiplier as the photodetector, and readout electronics (Fig. 1.1) [1].

SiPM analog interfaces throughout literature indicate a number of different amplifier topologies, including voltage amplifier [37, 6], charge amplifier [16, 24], transimpedance amplifier [26, 30, 13], various types of current conveyors, current mirrors and current buffers. The information extracted from analog readout, with further processing provides the detail of energy, time and position of nuclear interactions (Fig. 1.2).

In this work, an integrated SiPM readout based on bulk-driven transimpedance amplifier, simulated and fabricated in a commercial 180 nm CMOS process is presented and compared with a commercially available discrete charge amplifier for its suitability as a SiPM front end amplifier. The novelty of this works lies in the design and assessment of the bulk driven OTA for SiPM readout and the demonstration of the amplifier with a SiPM, scintillator, and source [71, 1, 2].

## 1.1 Thesis Outline

This thesis focuses on an amplifier design strategy suitable for integrating with the SiPM in the same chip and demonstrates the resulting design experimentally. Chapter 2 surveys the literature on SiPM structures and SiPM readout strategies. Chapter 3 discusses the amplifier design approach for portable SiPM based detectors. Chapter 4 outlines the SiPM based sensor for a nuclear detection application and finally chapter 5 presents a summary of the work.

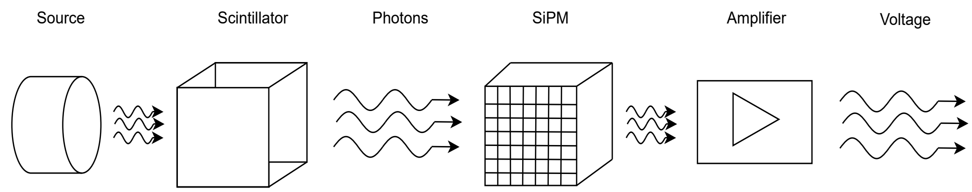


**Figure 1.1:** Scintillators convert nuclear particles into photons which are then transduced by the SiPM into electrons. These can be amplified and further processed using charge, current, or voltage based readout electronics [1].

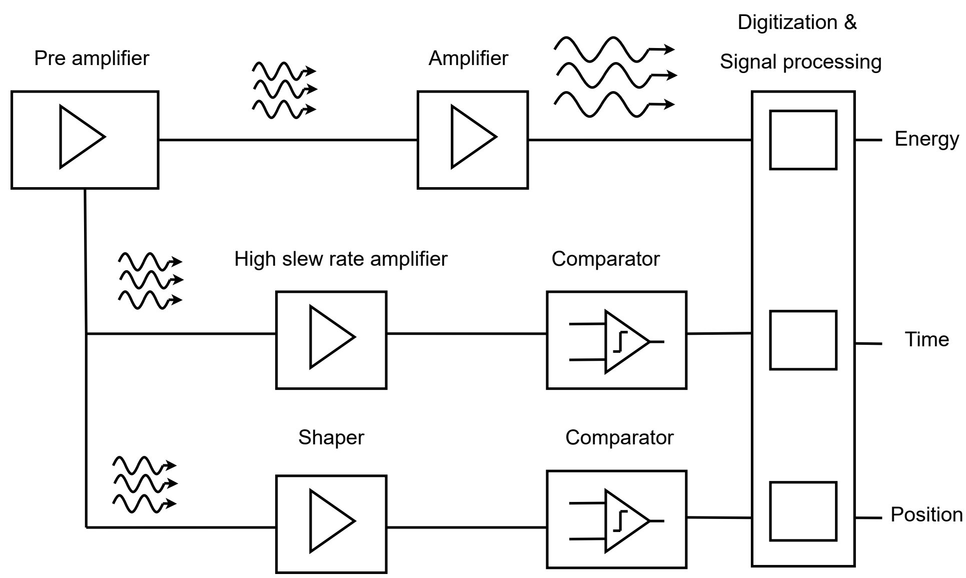


**Figure 1.2:** Typical readout in a nuclear imaging system requires various circuit topologies to extract time, energy, or position information [2].

# Chapter 2

# Literature Review

**Portions of this chapter were previously published as**

- A. Hesari, M. A. Haque, and N. McFarlane, "A Comprehensive Survey of Readout Strategies for SiPMs Used in Nuclear Imaging Systems," *Photonics* vol. 8, no. 7, p. 266, 2021.

## 2.1 SiPM applications

SiPMs are based on single photon avalanche diodes (SPADs) which are pn junction diodes which are biased in the reverse breakdown. These diodes can be implemented in any semiconducting material, such as the III-Vs (eg. InGaAs) or in Silicon. CMOS silicon foundries are commercially available and complex mixed signal circuits can be implemented in these processes for low cost. Thus, readout in designed in standard CMOS processes can be implemented directly alongside SiPMs in a single chip. This advantage make them a great choice in wide range of applications such as medical imaging [83, 84, 85, 86, 87], optical imaging systems [88, 89, 90, 91, 92], astrophysics and gamma detection [93, 94, 95, 96, 97, 98, 99, 100, 101, 102] and fluorescence imaging [103, 104, 105]. where they used in many experiments [106, 107, 108].

Imaging system based on SiPMs can be developed around discrete electronic component off the shelf or custom designed systems on printed circuit boards [109]. However, this is at the cost of higher parasitics which leads to lower the system speed. Moreover, this approach suffers from low spatial resolution due to optical dead zones. By integration of the SiPM with the readout circuits, the parasitics are potentially reduced. In addition, power and size can be significantly reduced. In complex multistage readouts, the overall fill factor may be affected, where the fill factor is defined as the optically PN junction active area vs non optical area. An example of the integration of silicon photomultiplier and the dedicated readout on the same chip can be found in [110, 111]. One approach of such a integration is separating the layer of SiPM and readout in a 3D integration process which affords the benefit of higher fill factor in comparison with regular 2D integration [112, 113].

In nuclear applications, silicon photomultipliers are coupled with the scintillator materials. Scintillator materials vary widely in light yield and sensitivity to various particles. With further processing, energy, time, and position of interaction can be quantified. The raw SiPM output signal is influenced by the scintillator material and thickness [114]. In addition, since the scintillator is the front-end transducer, its properties will limit the overall imaging system characteristics regardless of the sensitivity of the subsequent readout. Fig. 2.1, shows examples of nuclear readout circuit topologies and scintillators.

## 2.2 SiPM SPICE Model

SiPMs array are based on SPAD (single-photon avalanche diodes) along with quenching resistor. The SPADs are biased in reverse breakdown with a series resistor. When a photon is incident on a SPAD, generated electron-hole pairs under high electric field are accelerated. Then, due to impact ionization, influenced by the high energy charges, an avalanche current is generated. In order to stop the process and prevent destruction of the device due to high current flowing in it, quenching devices, either passive devices (such as a resistor), or active devices (such as transistors), are placed in series with SPADs.

SiPMs systems are divided into two categories, digital or analog. The difference between these two types of SiPM is the readout strategies. For the analog SiPM, the current in all of the SPADs are summed and readout through a amplifier. The output signal is thus analog in nature. For the digital SiPM, each SPAD has its own circuitry, and the output can be a count rate and is an all or nothing signal typically using a comparator with a user defined threshold.

SiPMs can be implemented through custom or commercial fabrication process. For commercial foundries an initial fabrication is needed to extract parameters suitable for simulating the model and readout electronic. However at the moment, a few commercial foundries, such as XFAB, offer SPADs with device models as part of their fabrication options [115, 116, 110, 117].

A general SiPM SPICE model is shown in Fig. 2.2. This model does not account for the full probabilistic nature of avalanche process, but it is suitable for designing, simulating, and characterizing the SiPM readout electronics. Fig. 2.2 consists of avalanching vs non-avalanching cells, where each cell consists of parasitic devices [118, 119, 31]. In the model, $R_q$ is the quenching resistance, $C_d$ is photodiode capacitance of SiPM's micro-cell, $C_q$ is the small parasitic capacitance in parallel to $C_q$ and $C_g$ is the total parasitic capacitance which account for interconnections between all the micro-cells. For a SiPM with many number of micro-cells, $C_d$/(N-1), $C_q$/(N-1) and $R_q$/(N-1), show the load of the other N–1 micro-cells.

This model clearly indicates that, on one hand, $C_d$ and $C_q$ values and, on the other hand, the bias and the breakdown voltage of SiPM, as is shown in Eq. 2.1 affect the amount of charge produced by SiPM.

$$Q_{TOT} = (C_d + C_q)(V_{BIAS} + V_{BR}) = (C_d + C_q)(\Delta V) \tag{2.1}$$

$C_q$ and $C_d$ also provides two paths for the released charge by SiPM at the input of the readout circuit. These two paths provide a "slow" and "fast" component of the voltage generated at the input of the readout circuit. In order to analyze these two paths, the charge is generated due to $C_q$ and $C_d$ is required. In addition, the equivalent capacitance of the detector at low and high frequencies has to be determined. Since $Q_F$, is responsible for the fast component of charge generated by SiPM, using Eq. 2.2, the amount of charge that is almost instantaneously flowing in $C_q$ and reaches the input node very quickly. This charge is,

$$Q_F = Q_{TOT}.C_q(C_q + C_d) \tag{2.2}$$

without $C_q$, slow time constant $R_q.C_d$, would dominate high frequency component of charge collection at the input of preamplifier.

At high frequency, equivalent capacitance of detector can be calculated using Eq. 2.3.

$$C_{HF} = C_g + [N(C_dC_q)/(C_d + C_q)] \tag{2.3}$$

With $C_{HF}$ and $Q_F$, the fast component of generated charge at the input of readout circuit can be calculated with Eq. 2.4

$$V_{INF}(t) = \frac{Q_F}{C_{HF}} e^{\frac{-t}{\tau_F}} \tag{2.4}$$

where, $\tau_F$ is the time constant formed by $R_{IN}$ and the high frequency equivalent capacitance of detector $C_{HF}$.

$$\tau_F = R_{IN}C_{HF} \tag{2.5}$$

Note that $C_{HF}$ represents the high-frequency equivalent capacitance of the detector, which is valid for a few ns after the micro-cell is fired. Also, since typically the input capacitance of the readout circuit in comparison with $C_{HF}$, is quite small, the effect of the equivalent input capacitance of readout electronics on the fast component of charge released by SiPM can be neglected.

The second part of the charge that reaches the input of the readout circuit is due to the slow component of charge generated by SiPM. Slow components of charge are the discharge current released by $C_d$ in parallel connection of $C_q$ and $R_q$. The amount of charge that $C_d$ receives from the total charge and slow time constant formed by $R_q$, $C_q$ and $C_d$ can be calculated with Eq. 2.6 and 2.7 respectively.

$$Q_D = Q_{TOT}C_d/(C_d + C_q) \tag{2.6}$$

$$I_D(t) = \frac{Q_D}{\tau_R} e^{\frac{-t}{\tau_R}} \tag{2.7}$$

where $\tau_R$ is recovery time constant of SiPM.

$$\tau_R = R_Q(C_d + C_q) \tag{2.8}$$

$$\tau_S = \tau_R + R_{IN}(C_g + NC_d) = \tau_R + R_{IN}C_{LF} \tag{2.9}$$

Using the values of $R_{IN}$, $Q_D$ and the time constant of the fast and slow components, 2.5 and 2.9, the input voltage of the preamplifier $V_{INS}$(t) due to the effect of the slow component of charge released by SiPM can be calculated,

$$V_{INS}(t) = R_{IN}(t)\frac{Q_D}{\tau_S - \tau_F}[e^{\frac{-t}{\tau_{RS}}} - \frac{-t}{\tau_{RF}}] \tag{2.10}$$

which exhibits a rising time dominated by the fast time constant $\tau_F$ and a long tail dominated by the slow time constant $\tau_S$. At low frequencies, the equivalent capacitance of the detector is calculated using,

$$C_{LF} = (C_g + NC_d) \tag{2.11}$$

$V_{INF}$(t) and $V_{INS}$(t) indicate that while good timing performance can be achieved by fast components of the signal, slow components are poor relevance in this respect. Another element that affects the fast and slow components of $V_{IN}$(t) is the input impedance of the readout circuit. In [120], the effects of the variation of RIN on the fast and slow components of the signal $V_{IN}$(t) are shown and indicate that by decreasing the input impedance of the readout circuit, the fall time of $V_{INF}$(t) gets faster. The reason lies in the fact that, as the input resistance of the readout circuit decreases, $C_{HF}$ is able to discharge faster since a larger discharge current is able to flow into readout input resistance. On the other hand, increasing the readout input resistance reduces the rate of detected events due to possible pile-up effects.

These results indicate that, for the readout circuit of SiPM, low input impedance is preferred. Low input impedance also helps to limit voltage variation across the detector due to firing up the SiPM's microcells at different times, when it is coupled with a scintillator.

Another conclusion that can be made in this section, regarding the current flow into the readout circuit, is that lower values of $R_{IN}$, on one hand, correspond to shorter tails of $I_{INF}$(t) and $I_{INS}$(t) and on the other hand, on the slope of $I_{INF}$(t).

SiPM simulations in this work were performed using SPAD SPICE models in Cadence. The model was adapted from [32] and is shown in Fig. 2.3. This model simulated both the dynamic avalanche and quench process and the static current voltage characteristics. It uses capacitances, resistors and voltage sources to model the diode substrate capacitances, forward and reverse bias operations and breakdown voltage.

The model, characterize the SPAD above the breakdown using $V_{SPAD}$. During the time that SPAD is reverse biased and below $V_R$, $SF$ and $SR$ switches are open. If the SPAD is quiescent, the current-controlled switch $S_{SELF}$ and the voltage-controlled switch $S_{TRIG}$ are open. Thus, in this way, by the external electronics, the reverse voltage applied between the SPAD's cathode and anode.

In this model, voltage or current stimulus, may apply through $R1$ and $R2$. If positive input apply and exceed the threshold voltage of $S_{TRIG}$, the switch closes are closed to mimics the avalanche ignition. Then he threshold current level ($I_q$), of $S_{SELF}$ rises to few milliampere. Now, $S_{SELF}$ is able to self-sustain the avalanche current up to the point that the current lowers below $I_q$, even if $S_{TRIG}$ is released. Thus, the current pulse interruption is set by $S_{SELF}$. It is noticeable that since $S_1$ switch is controlled by the voltage between anode and cathode (threshold voltage $V_{TS1}$=$-V_B$(breakdown voltage)), the photon signal may drives $S_{TRIG}$ only if the reverse voltage is above breakdown.

The forward mode, is characterized with a DC voltage generator ($V_F$), resistor ($R_F$), and $S_F$ switch [32]. $V_F$ used in the reference is 0.6-0.9 V, however this is a function of the material properties of the diode such as doping, materials (eg. STI, buried layers) and shape and can vary for different photodiodes. If the anode voltage is larger than the cathode voltage and lower than $VF$, then $SF$ opens and prevents current from flowing in the circuit. $SF$ switch will be open if $V_{AC}$, and exceeds $VF$. The switch $SR$ will complete the loop if the reverse voltage $V_{AC}$ is larger in magnitude than the secondary breakdown value, $VR$. Then the SPAD is in permanent breakdown and switch $S2$, with the threshold set to $VR$, inhibits any new photon input similar to the dead time that occurs in a realistic device.

In order to obviate the need for a current-controlled switch, $S_{SELF}$ is replaced by a a resistor to sense the current and a switch that depends on a voltage signal. $V_{SPAD}$ was split into two namely a $V_{SPAD}$ and $R_{SPAD}$. With using these andthe passive devices such as resistors and capacitors, and sources (either voltage or current) the model can be accurately simulated by correctly applying Kirchoff's current and voltage laws as a combination of voltages at nodes, current in branches and including built in complex expressions. It should be noted that these complex expressions can also potentially be implemented using operational amplifier based circuits and transistor level circuits. In this specific model the static current voltage curve is derived in a piecewise linear manner which is reflected in the circuit model which is a resistor and voltage source. In this model, $C_{AC}$, $C_{CS}$ and $C_{AS}$ represents the stray and junction capacitances of SPAD. More details about the model can be find in [32].

## 2.3 Analog and Digital SiPMs

SiPMs are often divided into two major groups, analog and digital. In ref [115], an analog and digital SiPMs developed in 0.35 $\mu$m, CMOS technology is presented. In an analog SiPM, each SPAD is in series with device that reduces the absolute value of the voltage across the SPAD to below the absolute value of the breakdown voltage and in doing so quenches the avalanche process by limiting the current flow through the device. The combination of each SPAD and quenching resistor is called a microcell. Fig. 2.4 is an example of a SiPM structure with 16×16 microcells divided into 4 macro-pixels and provides more detail about microcell and pixel definition. From the figure, one can say that in this specific example, each pixel consists of 64 microcell pixels consists of 64 microcell (8×8 microcells).

In analog SiPMs, the output is the sum of the individual currents of all microcells. While in digital SiPMs, each SPAD has its own readout circuit and active quenching circuitry [121], plus an integrated one-bit memory cell to switch on and off any desired SPADs [115] which aids in optimizing the overall dark counts. In recent years, digital SiPMs coupled with scintillators have provided an ideal choice for time-of-flight (TOF) positron emission tomography (PET) detectors. Integrated Time-to-Digital Converters (TDC) with digital SiPMs, besides providing low noise timing information, enables the designer to build an extremely miniaturized PET detector.

As an example, multiple integrated TDCs called multi-channel digital SiPM (MD-SiPM) as part of a PET scanner are developed and tested in [122]. In either analog or digital SiPMs, for small array SiPM readout, each channel can be read out independently using dedicated amplifiers and data acquisition circuits [123, 124, 125, 126]. However, multiplexing is needed if dealing with larger arrays [127, 128, 129]. Multiplexing also aid in correcting pixel non-uniformities due to design or fabrication process variations [130].

## 2.4 SiPM Signal Generation

A SiPM's current pulse is proportional to the amount of charge due the incoming light and thus directly proportional to the source intensity (number and rate of incident particles) and scintillator (material type and light yield). Therefore, the equivalent circuit of SiPMs can be considered as a current source. In a similar way, the readout circuit, which can be generally termed as a preamplifier, has an effective input resistance, $R_a$, and capacitance, $C_a$. The arrangement of a SiPM in conjunction with the readout circuit and its equivalent circuit is shown in 2.5. Fig. 2.5 shows the total resistance (R) and capacitance (C) form an RC circuit with a time constant $\tau=$ RC. The current pulse from SiPM appears as a voltage pulse at the input of the readout circuit and its shape is a function of the RC time constant. Now, if the RC time constant in comparison with the duration of charge collection is small enough, then the SiPM's output current and the current flow into the readout circuit are almost identical and called a current pulse.

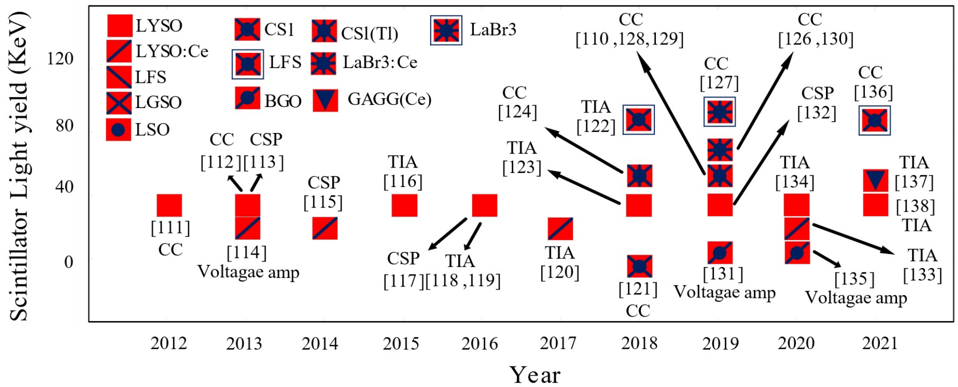


**Figure 2.1:** Readout circuits used in nuclear imaging with various scintillator materials, from 2012 to 2021 [3, 4, 5, 6, 7, 8, 9, 10, 11, 12, 13, 14, 15, 16, 17, 18, 19, 20, 21, 22, 23, 24, 25, 26, 27, 28, 29, 30].

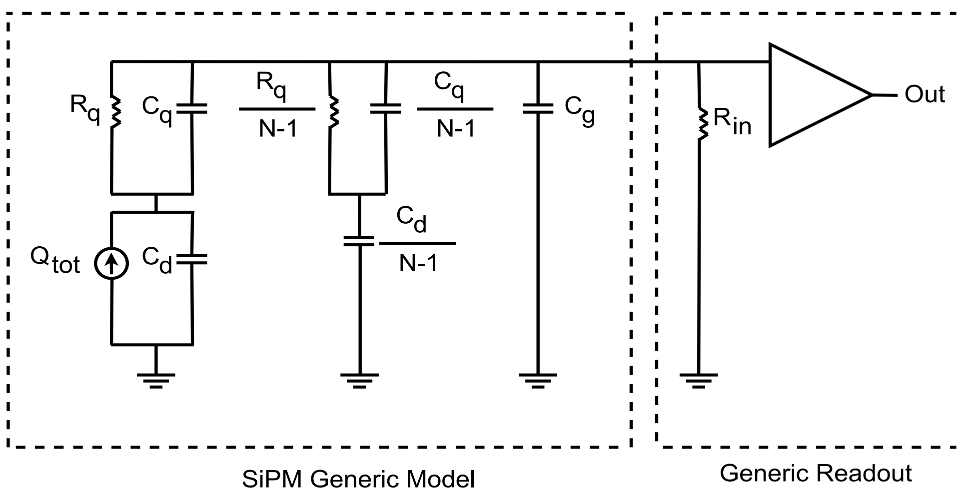


**Figure 2.2:** SiPM circuit model showing 1 avalanching cell and (N-1) non-avalanching cells [31].

**Table 2.1:** Minimal detectable signal with photodetectors

| Photodetector type | Minimum detectable photon signal | Gain |
|---|---|---|
| PIN photodiode (PD) | 200–300 photon | 1 |
| Avalnche Photodiode (APD) | 10–20 photon | 10–300 |
| Photomultiplier Tube (PMT) | 1 photon | $10^3$–$10^8$ |
| Silicon Photomultiplier (SiPM) | 1 photon | $10^4$–$10^7$ |

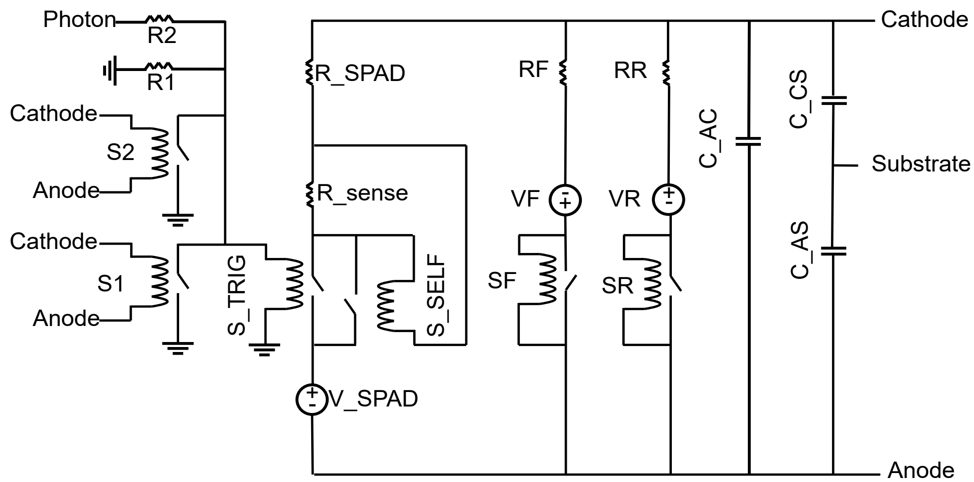


**Figure 2.3:** SPAD SPICE model used in simulations. [32].

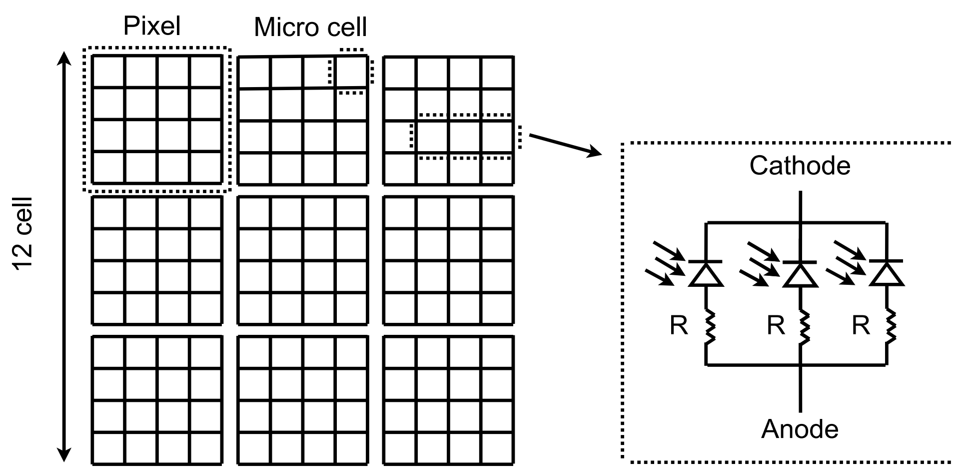


**Figure 2.4:** An example of 3×3 pixel SiPM (12×12 cell).

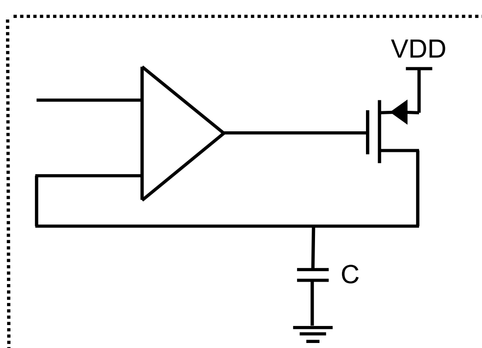


**Figure 2.5:** The arrangement of a photodetector (SiPM) in conjunction with readout circuit and its equivalent circuit [33].

But most of the time, the RC time constant is much longer than the duration of charge collection and the SiPM's output current is integrated into the equivalent capacitor. This pulse, which is called a charge pulse, eventually discharges the resistor and generates a voltage pulse [131].

The voltage pulse generated at the output of the readout circuit can carry different types of information out, such as the type of particle, timing, position, and the energy of the signal. The basic characteristics of a pulse detector are shown in Fig. 2.6.

Fig. 2.6 shows the SiPM's pulse, which in general consists of two parts, the leading edge and tailing edge. The leading edge is the time duration when the pulse reaches its maximum value and the tailing edge, is the time signal from the maximum value, falls to its initial value. Rise time, fall time, and peaking time are also shown in 2.6, and are defined as the time SiPM's pulse goes from 10% to 90%, goes from 90% to 10%, and the time it takes for the leading-edge to rise from zero to the maximum height, respectively. The SiPM's pulse width is generally measured in units of time and defines the distance between the 50% points on the leading and trailing edges. The other terms shown in Fig. 2.6 are baseline and offset. The baseline is translated to the voltage level at which the pulse starts and finishes.

Although in a general case, it is expected to see the baseline level at zero volts, the baseline, for various reasons such as fluctuations in the pulse shape, can start at a non-zero level voltage, and is referred to as an offset. The last term that is shown in Fig. 2.6, is pulse amplitude, which is defined as the difference between the pulse baseline and the maximum value of the pulse. In SiPM pulse processing applications, pulses can be considered "fast" or "slow". Generally, a pulse with less than a few nanoseconds rising in time is considered a fast pulse. As an example, a typical SiPM's output current has a rise time of less than a few nanoseconds while the duration of a pulse may extend to a few microseconds.

## 2.5 Energy measurements

Energy or pulse-height spectroscopy systems play a key role in many applications such as medical applications. The generated charge on a SiPM's electrodes is proportional to the incident light and thus to the source through the scintillation transducer function. Therefore, the readout pulse amplitude that is generated by a couple of building blocks of electronic circuits, represents the distribution of energy deposition in SiPM. The basic structure of such a system is shown in Fig. 2.7.

The first stage of a typical energy spectroscopy readout is usually a charge-sensitive preamplifier, though in some cases, a current sensitive or voltage-sensitive preamplifier may be used. If a charge amplifier is used as the first stage, the SiPM's current is converted and amplified into a charge pulse. The charge pulses are then fed into a shaper which is sometimes also called a linear amplifier. The shaper, while amplifying the amplitude signal of the preamplifier stage, will help optimize the signal to noise of the readout circuit. Also, at high event rates, the shaper, by reducing the decay time of events, is better able to separate the events.

As shown in Fig. 2.7, a typical shaper is comprised of a low pass (also called integrator) and a high pass filter (also called differentiator). A high pass filter limits the noise at smaller frequencies. A low pass filter influences the equivalent noise bandwidth. The band-pass filter frequency response function is designed for optimized signal-to-noise ratio. The next building block of energy spectroscopy is a multi-channel analyzer (MCA). The MCA sorts the amplitudes of hte pulses into user defined bins and produces a spectrum of pulse heights. A typical MCA consists of three building blocks, an analog-to-digital converter (ADC), a histogram memory, and a monitor display. The resolution of the ADC affects the number of channels (typically ranges from 512 to 65536) displayed in the spectrum.

Ideally, for the same amount of energy, one may expect to see the same amplitude (or channel number) as measured by a spectroscopy system. However, in practice, the amplitude of pulses corresponds to the same amount of energy that varies from each other. In a real scenario, a real pulse-height spectrum has a finite width for a constant energy value. Therefore, the energy resolution is defined as the full width at half maximum (FWHM) of the Gaussian function. The energy resolution of a radiation detector is given by Eq. 2.12 and is shown in Fig. 2.8,

$$R = \frac{\Delta H_{fwhm}}{H_0} \tag{2.12}$$

In Fig. 2.8, $H_0$ is the related the average of the particle's energy. Producing vibration in the crystal lattice, SiPM's size and electronic noise are the major sources of fluctuation in the amplitude of pulses in response to the same amount of energy. Among these, electronic noise can be decreased with a proper choice of circuit frequency response design that removes the out-of-band noise.

A shaper produces an output pulse with an amplitude proportional to the amplitude of the input pulse. However, any variation in the input port of the shaper due to fluctuation in SiPM's output current, will result in variation in the amplitude of the shaper's output pulses and affect the energy resolution [33]. Energy resolution may also be affected by pulse pileup, which implies an inability to separate pulses from their source. Pulse pileup due to a high detection rate and/or width of the pulses can be divided into tail and head pileups. When two or more pulses have a shorter time interval than the time constant of the filters, it is known as head pileup. In this case, the readout sees all the pulses as a single pulse and is unable to accurately quantify the signal's amplitude.

Another phenomenon that can affect energy resolution is baseline fluctuations. SiPM's leakage current, pulse processing errors, and thermal drift of the readout circuit are the major sources of baseline variations. In nuclear readout circuits, random distribution of events will result in variation in the average DC voltage which consequently results in a shift of the baseline and degradation of energy resolution that is proportionals to the count rate. There are also some other phenomena that can have a negative effects on energy resolution, such as a change in performance of SiPM and scintillator due to aging, temperature, and humidity [132, 133].

The photon energy of an event (defined as photons being incident on the SiPMs), is proportional to the SiPM's charge or current pulse, and is an important characteristic. The peak signal provides information on the energy of the photons. Energy resolution may affected by type of scintillator material and physical mechanisms such as ballistic deficit, pulse pileup, or baseline fluctuation [134, 135, 136, 137, 138, 98].

Table 2.2 shows a relative comparison of the energy resolution using different scintillator materials.The total photon absorption depends on the type and thickness of material and incident energy of photons. For example, four different scintillators, CsI(Tl), NaI(Tl), LaBr3(Ce) and GAGG(Ce), showed a direct relationship between energy resolution and material type and thickness [114]. Thus, it is important to take the scintillator material into account when characterizing the full system.

## 2.6 Timing Measurements

In many fields such as nuclear science and medical imaging eg. positron emission tomography (PET), the measurement of time intervals between events is of great importance. Each detected event is corresponds directly with an output pulse [33]. Therefore difference between the arrival times of pulses from the corresponding SiPMs can translate to time intervals between the events which range from a few ps up to few $\mu$s [75].

In addition to energy, the time of arrival of pulses, corresponding to events, is also of interest [139]. Fig. 2.9 shows the response of various types of events. Time of flight measurements determine the distribution of the time difference between events. Uncorrelated signals will have a flat time difference distribution.

Correlated signals, such as those which occur in prompt coincidence, delayed coincidence, or time of flight experiments, show a delta or spike shaped distribution [33, 140, 141]. Noise in time of flight is controlled by the coincidence resolving time [142]. Time domain information can always be converted to frequency domain. This can be done either in software or in hardware using either analog, digital, or a combination of analog and digital techniques.

Fig. 2.9, provides some examples of transient measurements that can be seen with SiPMs output pulses in response to an input source. In Fig. 2.9(a), shows that if two uncorrelated particle hit the surface of two SiPM, the time difference between the two is a random value. Therefore, the time distribution between the events shows a flat profile and does not provide any useful information.

Fig. 2.9(b) is an example of prompt coincidence events. In an prompt coincidence event, two particle are produce at the same time. Now if this particle hits the surface of the two SiPMs, they can initiate pulses at the same time and the time distribution will have a delta function shape. Delayed coincident measurement is another type of time measurement that is represented in Figure 2.9(c). Delay time between gamma particles is a key factor in half-life of the nuclear state measurements [33].

And finally Fig. 2.9(d) presents an example of time-of-flight(ToF) measurement. ToF indicates the traveling time of photons between two SiPMs. ToF has a direct relationship with the speed or velocity of particles. Some information such as type of particles can be achieve using ToF measurement.

The block diagram of a typical time spectrometer is shown in Fig. 2.10 [33]. In this Figure, the start label refers to the detector that is chosen to be as the reference detector and the stop label refers to the second detector where the time difference of which is measured in comparison with the reference detector. The signal pulses from each detector are fed into a comparator or discriminator. The discriminator generates a logic pulse with leading edge (LE) of few hundreds of pico seconds, corresponding to the time of occurrence of an event. The output signal of the discriminator is fed into a time to amplitude converter or TAC. The TAC generates an output voltage whose amplitude is directly proportional (and linear) to the time interval between input start and stop pulses [143]. Generally, the stop signals are followed by a delay building block, to ensure that the stop signal will be received after the start signal. Finally, a multi-channel analyzer measures the time spectrum which define as time interval between the start and stop pulses and generates a spectrum that gives the number of event versus time interval length [33].

There is always a level of uncertainty with the results of a time measurement in an actual event. For example a prompt coincidence time spectrum is shown in Fig. 2.9(b). In reality, the spectrum follows a Gaussian distribution as shown in Fig. 2.11.

All timing measurements are compared using the timing resolution which is defined as the FWHM of a prompt coincidence time distribution [144]. In general, higher the resolution is better. Achieving higher resolution requires narrower peaking time that enables the system to separate two closely spaced events. Timing resolution in general can be affected by pulse processing system and type of detector and particles.

Timing discriminators are part of timing measurement building blocks that are able to generate a logic pulse in response to the arrival time of detector input pulse that features very fast leading edge. An ideal timing discriminator at the arrival time of input pulses, should produce a logic pulse [33]. However, in practical timing discriminators, due to noise of electronic circuits, logic pulses will produce a constant and precise delay time in regard to arrival time of input pulses. There are two different approach to implement a time pick-off circuit such as, Leading-Edge Discriminator and Constant-Fraction Discriminator which are consider as high accuracy timing measurements [145]. However, in some applications that timing accuracy does not play a key role, there are some other approach such as using Timing single-Channel analyzer, provide a roughly approximation of arrival time of input pulses [146]. All these approach are briefly described in the following sections.

The most simple type of timing discriminator are leading edge discriminator (LED). In this approach, If the input signal goes above a preset threshold level, LE, generate a logic signal. A typical LE, can be built with a very fast comparator that compares the input signal coming from detector with a threshold level [147]. The output signal of the comparator, usually fed into a mono-stable multivibrator to provide short width logic pulses that is needed by coincidence circuit. One of the serious problem with this type of discriminator is Time-Walk. Generally Time-Walk define as time movement of logic pulse produced by LE, in response to variation in amplitude and shape of input pulses [148]. Constant-Fraction Discriminator (CFD) is another type of timing discriminator that can address this challenge.

In a Constant-Fraction Discriminator (CFD), the discrimination level is not fixed and change based on input pulse amplitude. Both LE and CFD approaches that are described in previous sections, are considered as high accuracy timing measurements that involve multiple building blocks for the timing measurement. However, if in a particular application the main focus is not the timing, a timing single-channel analyzer (TSCA) is able to provide a raw estimation of timing. TSCA provides information about both energy and timing of the input pulses [149]. The energy information extracted from the peak amplitude of the pulses while timing information can be obtained from zero-crossing time of a pulse shaping amplifier. The dependency of the time pick-off on the shape of input signal and poor slop to noise ratio in comparison with other type of time pick-off method are the disadvantage of this approach in regards to timing measurement.

Typical TACs are designed with a buffer, capacitor, current source, and switches. Generally the output signal of the TAC is fed through an MCA or an ADC for further software processing and generation of a time spectrum [150]. The most easiest and straight forward method of TAC signal digitization is to use an time to digital converter (TDC) [151]. However this not a fast and low cost method for applications that are ed with number of channels or need to perform a fast and quick digital TAC signal.

Fig. 2.12 (a) shows the use of a discriminator (comparator) to determine if an event occurred [152, 153]. Delay units to enable proper comparison of the time stamps [154, 155], time to amplitude converters (TAC) [156], and multi-channel analyzers [157, 158] are required to accurately report the timing. Fig. 2.12(b) filters the events within some range before the discriminator and improves the signal to noise [35]. Each of these approaches can be implemented using discrete off the shelf components or implemented using custom integrated circuits fabricated in commercial foundries. In all cases, the analog modules contain amplifiers and filters, along with the digital and quasi-digital blocks, such as comparators, and encoders [40, 159, 160, 161, 162, 163]. Depending on the scintillator type and material, such as LGSO, LYSO, GAGG, LuAG, YAG, LSO, and LFS, various types of SiPMs may have different time resolution [164].

The required resolution depends on application, where, for example, in PET, sub 10 ps is a research target. The maximum achievable coincidence time resolution (CTR), based on scintillator statistics, can be estimated using [165],

$$CTR = \alpha\sqrt{\frac{\tau_r \tau_f}{n}} \tag{2.13}$$

where $\tau_r$ and $\tau_f$ are the scintillation rise and fall time, n is the number of photons, and $\alpha$ is a constant. For example, for an output light of between 27.9 and 49.5 kphoton/MeV measured upon gamma CS173 excitation, the best achievable CTR with Cerium-doped GAGG:Ce scintillator was 87±2 ps [152].

The other factor that has an influence on time resolution is the readout electronic noise. A passive compensation circuit for device capacitance to reduce the effect of electronic noise on time resolution is discussed in [139]. This technique provided no injection of noise from the SiPM to the readout circuit and improved the single photon time resolution.

In some other work, different time resolution, ranging from less than 80 ps [164] up to more than 330 ps FWHM [166] can be found. In [167, 168], improved time resolution is achieved by connecting multiple SiPMs in series creating multiple scintillation counters. For a readout circuit, consist of N counter, the resolution improves by factor of $1/\sqrt{N}$.

To determine the time of an event, comparators and digital gates may be used [169, 170]. Comparators type (or discriminators) can be constant fraction (CFD) or leading edge (LED) [171]. However at lower threshold, LED provide better time resolution [172, 173]. Comparators can have errors due to jitter, long term and short term drift, and variation in the shape and amplitude of the input pulse [174]. This can be compensated by 1-D techniques such as linear or logarithmic compensation or 2-D compensation techniques like artificial neural network and polynomial [147, 175].

Time resolution is determined with the full width half maximum of the time spectrum [176]. To achieve the best time resolution, [36] suggest to set the shaping time at 61% of pulse amplitude. where the peaking time needs to be approximately of 3 to 5 times, grater than the shaping time (Fig. 2.12 (c)).

Delays can be generated using coaxial cables, active circuits or lumped elements [177, 178, 179]. However, the use of coaxial cables may also attenuate, frequency shift, or reflect the signal.

Time to amplitude converters (TAC) generate an analog output whose amplitude is proportional to the measured time interval. They may be implemented using a purely analog, digital, or mixed signal approach [180, 181, 34]. The time resolution is limited by the accuracy of the timing discriminators [36, 182]. As with the energy measurements, ADCs may be replaced by time to digital converters (TDC) [183, 184].

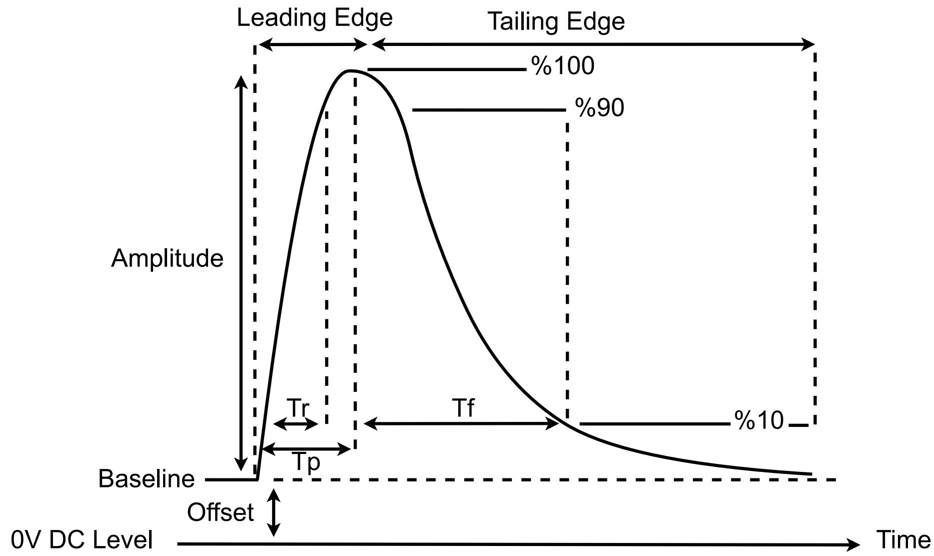


**Figure 2.6:** SiPM pulse Characteristic [33].

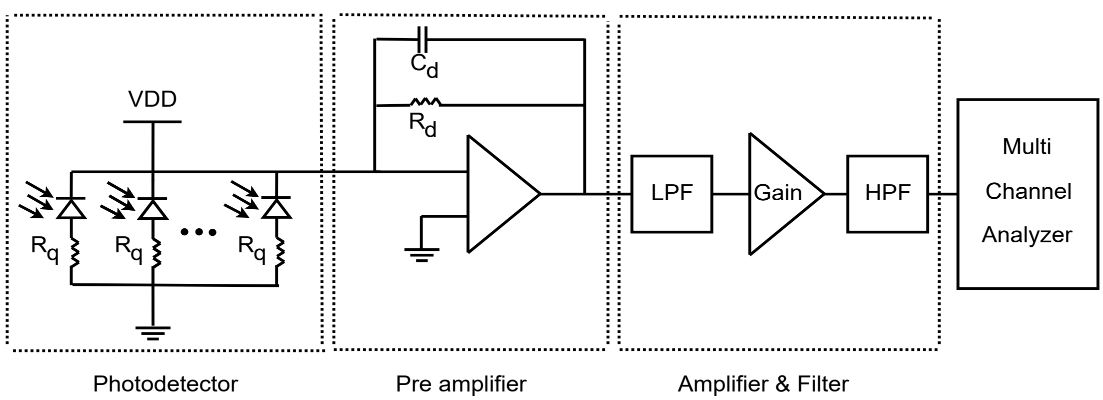


**Figure 2.7:** Energy spectroscopy building blocks [33].

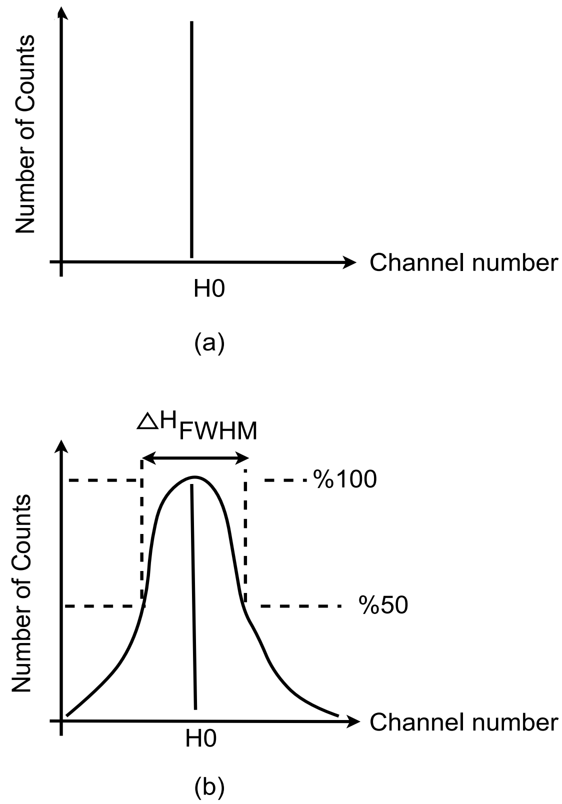


**Figure 2.8:** Energy resolution (a) Ideal case (b) Real case [33].

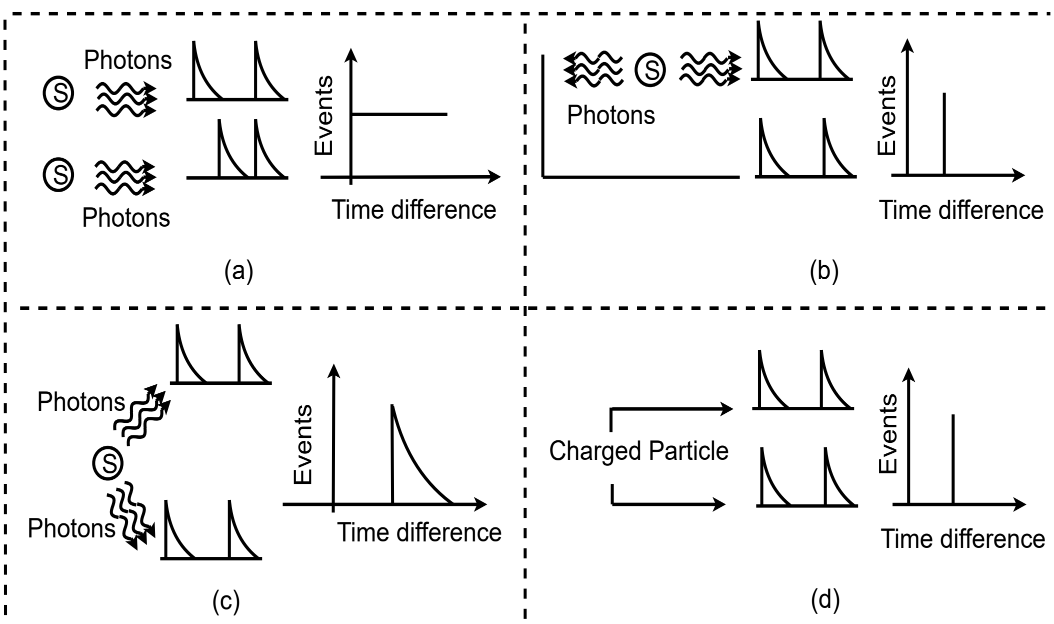


**Figure 2.9:** Time measurements due to a source or sources, (a) uncorrelated events (b) prompt coincidence (c) delayed coincidence (d) time of flight [33].

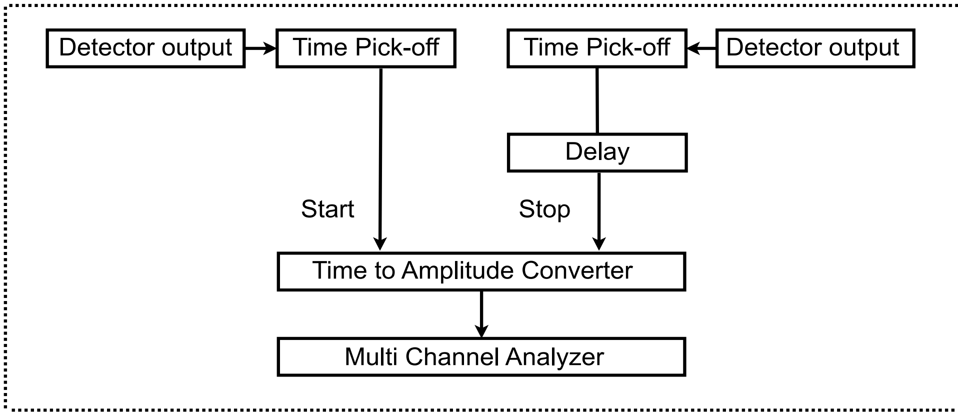


**Figure 2.10:** Typical time spectrometer building block [33].

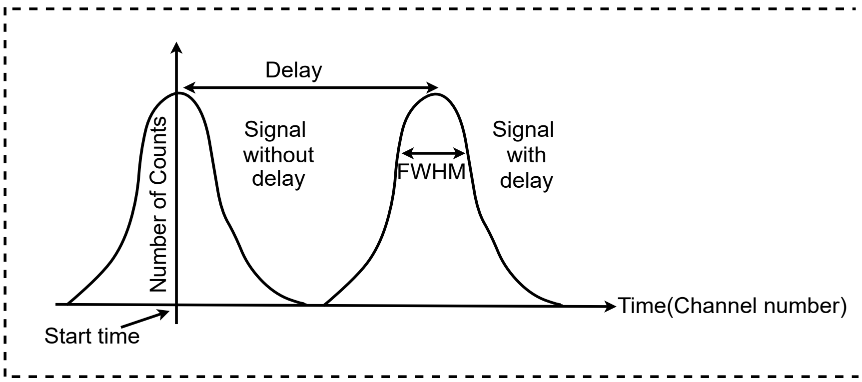


**Figure 2.11:** Coincidence time spectrum [33].

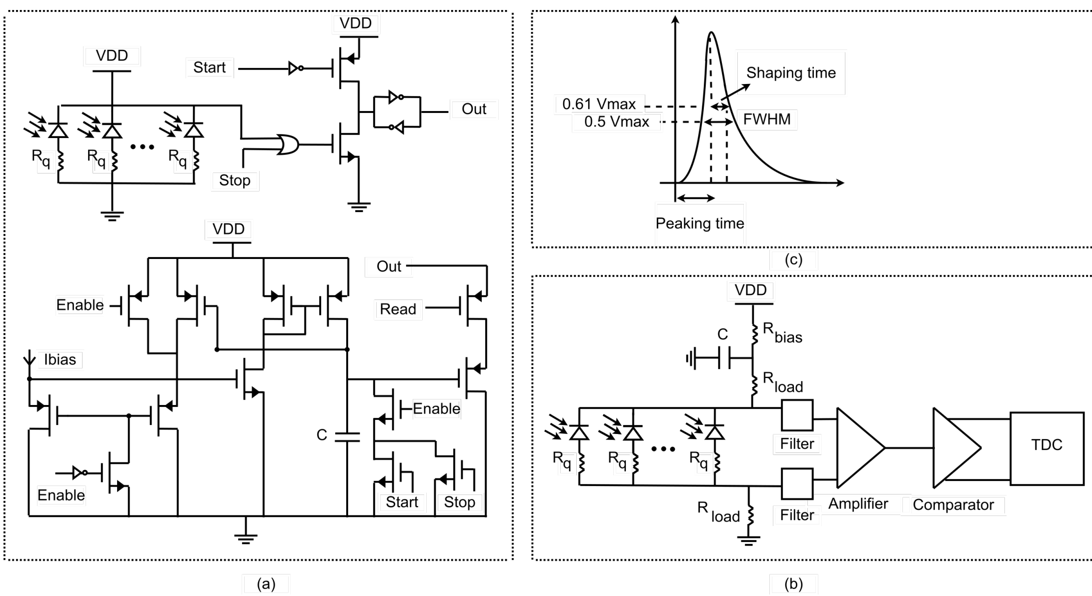


**Figure 2.12:** (a) Time to analog conversion [34], (b) time spectrometer with differential amplifier [35], and (c) definitions of the shaping and peaking times [36].

Both analog and digital readout approaches can have similar time resolution [185, 186, 187, 188]. Due to increased power consumption, large number of readout channels, and challenges in digital realization [189], analog SiPMs are more prevalent in nuclear imaging applications. Fig. 2.13, shows CTR and energy resolution for different front-ends.

## 2.7 Position Sensing

When implemented in integrated circuits, the inherently asynchronous and event-based nature of the signal make them suitable for employing the asynchronous readout such as address event representation (AER) protocol [190, 191, 192]. This has been implemented in a standard CMOS technology with a digital SiPM architecture [193]. By comparison of the arrival time of two or more pixels, from AER communication protocol, position information also can be extracted [194, 195].

In some work multiplexing method is used to reduce the number of signals for further processing (Fig. 2.14). In this approach, for each row and column in SiPM array, the anodes and cathodes are summed to form the row and column signals respectively. Then all row and column signal are need to be amplified and weighted proportional with their location. This approach is used by [38] where discrete amplifiers are used as an amplification stage.

## 2.8 SiPM ASIC Pulse Processing

Pulse processing of radiation imaging systems is generally carried out using an application specific integrated circuit(ASIC) pulse processing systems. A typical circuit schematic of such a readout circuit is shown in Fig. 2.15 and includes two section. The first part, which is known as front-end electronics, includes many analog building blocks, such as a preamplifier, amplifier, shaper, pole-zero cancellation circuit, comparator, sample and hold circuit, and buffer. The output signal of the front-end electronics are fed into a processing unit that can be an ADC or ToT (Time-over-Threshold) systems [33].

Since radiation particles, such as gammas or neutrons, can randomly incident onto the scintillator and transduced into light which is incident on the SiPMs, front-end readouts have to be able to detect the occurrence and the moment of an event. This ability is called self-triggering ability [196]. Usually a comparator compares the signal amplitude with a certain threshold voltage and produce a self-trigger signal. If two comparators are used at two different threshold voltages, then one is able to detect the events that are in a specific energy level that is set by threshold level of comparators [197].

### 2.8.1 ASIC Pole-Zero Cancellation

Usually a preamplifier output signal has a long decay time constant. This long decay output signal, if directly fed into amplifier stage, can cause undershoot at the output of amplifier. At high count rate, this phenomena can cause the output pulse of amplifier ride on the undershoot of previous pulses and eventually poor energy resolution. In this situations, pole-zero cancellation circuit are being used between the preamplifier and amplifier. A typical pole-zero cancellation circuit schematic which is frequently used in shaping amplifiers is depicted in Fig. 2.16 [33].

Pole-zero cancellation circuit using a relatively large feedback resistor is able to eliminate the negative effect of pulse undershoot. However an integrated large resistor consume large die area. One typical approach to implement such a large resistor is using a CMOS transistor in linear region [198]. However, large variation of preamplifier due to large variation of input signals, has a negative effect on linearity of the cmos transistor that is working in linear region. This negative effect which is known as nonlinearity of the preamplifier feedback element, eventually produce a non-exponential decay signal at the output of preamplifier stage. One approach to eliminate the negative effect of nonlinearity of the preamplifier feedback element is discussed in [39] which is depicted in Fig. 2.17.

Baseline restoration circuits are used to alleviate the negative effect of baseline fluctuation. The most basic type of a baseline restoration circuit is depicted in Fig. 2.18, can be designed with a switch and capacitor. The idea is to provide a large time constant to avoid baseline shifts and any undershoot associated with pulses. Proper choice of time constant plays a key role in designing baseline restoration circuits [199].

### 2.8.2 ASIC Pulse Shaper

The low level amplitude signal of the preamplifier stage needs to be amplified with an amplifier into a proper linear voltage signal and is needed for further signal processing. Using an amplifier will also help with optimization of shape of output pulses for the preamplifier stage. This optimization, results in on one hand, increased the SNR ratio and on the other hand minimized negative effect of pulse pileup and baseline variation. The shaper stage is made of an amplifier plus a band-pass filter. Band pass filter can be realized with combination of a LPF (Low Pass Filter) and HPF (High Pass Filter) [33].

The combination of a LPF (Resistor-Capacitor integrator) and HPF (Capacitor-Resistor differentiator) is the simplest pulse shaping stage [200]. However, these stages are area intensive if implemented in standard CMOS. The circuit schematic and output pulse of this structure is depicted in Fig. 2.19 .

However, while this structure may be a good choice for pulse shaping for low rate applications, a long tail output pulse at high rates can cause pileup problem. In order to eliminate the effect of pileup in high rate applications and still utilize a simple structure, an easy way to reduce the long tail of shaper output pulse is to use one differentiator and multiple integrator as shown in Fig. 2.20 [40].

In practice it has been shown that the maximum integrator that can be used to reduce the long tail of shaper's output pulse, is four integrators. A filter that is made of one differentiator and four integrator is called semi-Gaussian filter. Another type of differentiator and integrator which are more frequently used in shaper building block are active differentiator and integrators. Circuit schematic of these kind of filters are shown in Fig. 2.21 (a) and (b) respectively [41].

An ideal shaper needs to have an infinite number of low-pass filter which is impractical. However, combination of a high-pass filter with active low-pass filter with conjugate poles, will result in a good approximation of ideal pulse shaper. Circuit schematic of a Gaussian shaper made of a high-pass filter in conjunction with a second order active integrator is depicted in Fig. 2.22 [33].

The shaper stage (also known as shaper filters), which may be present in energy, timing, and position measurement [201, 40], are used to tackle the problem of pulse pileup. Gaussian based architectures are popular shaper implementations [202]. Frequency bandwidth limitations can improve the sSNR [203]. However, bandwidth limitation, may cause negative overshoot for large shaping parameter [201]. Quasi-Gaussian or trapezoidal shapers have also been implemented [40].

Low-pass filters, for example using a Sallen-Key filter, can calibrate for drift and improve signal-to-noise [204]. Shapers have also been implemented using digital $CR-RC^m$ [205]. The pulse pile up problem need to be investigated at high input rate application. This problem can be addressed by implementing pole zero cancellation circuits (PZC). An example of this type of circuit can be find in [206], where the PZC has been implemented by twenty PMOS transistors and a 24pF capacitor. In addition to tackle the problem of pile up, Pole zero cancellation eliminates the undershoot and allows for higher rate counting [40, 207, 208, 209].

The shaper's output signal is pass into a sample and hold circuit (also called a peak stretcher) to store the peak value of the signal before digitizing [210]. Analog to digital converters (ADCs) are also used in energy measurement systems. They range from successive approximation (SAR), delta-sigma, dual slope, pipelined, and flash architectures [178, 211, 212, 98]. These architectures offer various advantages in speed, resolution, power, and area on chip. ADCs in general are power hungry and can be area intensive on chip. Thus, other digitization and quasi-digitization strategies such as time-over-threshold (ToT) circuits may be employed [213]. In a ToT circuit, the difference between two time stamps where the signal crosses a pre-defined threshold is stored.

This can be implemented with time to digital conversion [214, 215]. Integration of readout electronics and digital SiPM, within a single chip can make them noisier than analog SiPMs. This is because the digital SiPMs will typically be in standard CMOS where no special efforts have been made to optimize the process for optical detection [216]. Many commercially available off the shelf SiPMs are analog and are optimized for optical response (which typically means that transistors implemented in the process are sometimes sub-optimal in charactersitics). For analog and digital SiPMs both implemented in CMOS, the noise of the optical detecting device remains the same and there are distinct advantages and disadvantages for the digital or analog approach. Customized analog SiPMs have better noise performance for energy measurements as the energy resolution depends on the optical performance i.e. the statistical properties of photon induced charge generation. [217].

A shaper is made of a high-pass and low-pass filters which in ASIC shapers, frequently built up with Gaussian filters with complex conjugate poles. The higher the order of shaper, will result in shorter pulse width which is a key parameter, specially at high count rate. But at the same time, the higher the order of shaper is translate to higher power consumption and consume more die area on chip which is a limit factor in portable applications. Two types of ASIC pulse shaper are discussed in [39] and [42] are depicted in Figure 2.23 (a) and (b) respectively.

### 2.8.3 ASIC Peak Detect Sample and Hold

Conversion of the output signal of front-end readout by ADCs in order to further processing, generally takes longer period of time in comparison with signal duration. Therefore there is a need for, detect, sample and hold the peak amplitude of pulses for a period of time, comparable with the conversion time of Analog to digital converter. Circuit schematic of a basic peak stretcher that is known as peak detect sample and hold and also peak detect and hold (PDH) is shown in Fig. 2.24 [43]. In this structure, a transconductance amplifier, charge a capacitor which is used to save the amplitude of input pulses. Every time that the input voltage of transconductance amplifier is higher that its output voltage, a current flow through the capacitor and the amplitude of pulses is saved on capacitor. Once the output voltage goes above the input voltage of transconductance amplifier, the diode blocks the discharge of capacitor, thus the maximum value of input pulses is hold on capacitor. Although this structure looks pretty easy ans simple for integration but in practice, to avoid the problem associate with parallel component with diode in integrated circuits, there are some other alternative PDH circuit that are being used in spectroscopy ASIC circuits. For positive pulses, [44] discuss a PDH circuit that can be a good choice of a PDH integrated circuit (Fig. 2.25).

The PMOS in Fig. 2.25 acts as both a charging and a switching element. The voltage difference due to the arrival of an input signal at the input port of amplifier, provides an inverting signal at the gate of PMOS and turns it on. As a consequence, the charge will be stored on capacitor, C, and increases the voltage level at the positive port of the amplifier. Once the input voltage fall below the voltage over the capacitor, the PMOS transistor will turn off and the capacitor, C, will hold the peak amplitude of the input signal.

### 2.8.4 ASIC ADC and ToT

Depending on application, one may need to digitize the output signal of PDH stage. Different type of ADCs such as SAR and wilkinson ADC, can be used to achieve this purpose. However, ADCs are generally power hungry building blocks and consume quite a large die are on chip. As an alternative for ADCs on chip, Time-over-Threshold circuits, are frequently used in spectroscopy systems [218]. Fig. 2.26, provide the detail of typical building blocks that are used in an ASIC readout circuit of a spectroscopy system that is include shaper, comparator and an encoder. The comparator, receive signal from the shaper and compare it with a preset threshold voltage. The comparator generate an output signal with a width equal to the time period that the shaper output signal exceed the comparator threshold level. This time period is called time over threshold (ToT). There is a non-linear relationship between the ToT and the amplitude of signals. Logic AND of the ToT signal with a reference clock provide a digital signal which help to count the number of pulses in digital domain. Non-linear relationship between the time width and amplitude of pulses can be resolved using some methods such as dynamic ToT that is discussed in [219].

## 2.9 SiPM Interface with ASIC

The preamplifier is the front-end analog readout between the raw SiPM readout and the signal processing electronics. Thus, its characteristics directly affect the performance of subsequent stages. The preamplifier stage can be implemented as either single ended or fully differential.

When implemented as a fully differential amplifier, a common-mode feedback stage is required to maintain the common mode at a known level [220].

Typical common mode approaches will take the difference of the average of the amplifier outputs with the common mode voltage to adjust the tail current or the currents in the active loads to move the common mode voltage up or down as required. Implementations of common mode feedback can use either diff amp based or switch capacitor based. Reference [58] describes an auxiliary amplifier-based common-mode feedback circuit (CMFB) that has a phase margin of 62.1° and gain margin of 25 dB.

The initial SiPM output signal must be amplified before further processed and digitized. The three typical approaches for front-end amplification that are used to readout the SiPM arrays consist of charge, transimpedance, or voltage amplification and are shown in Fig. 2.27.

A typical implementation using commercially available off the shelf parts may use the standard inverting or non-inverting configuration where the gain is a function of the resistive feedback network (Fig. 2.27(c)). The size of $R_{load}$, affects the input DC bias of the opamp [221]. The total input capacitance, formed by the parallel combination of parasitic capacitance of the SiPM and amplifier, $C_d$ and $C_{in}$ and the total input impedance, form a time constant that should be minimized such that the fastest input signal can be recognized [47].

### 2.9.1 Voltage-Sensitive Amplifiers

Robustness, simplicity, and ease of implementation and simulation, makes the voltage amplifier an ideal choice of readout circuit when dealing with unknown SiPMs. However, this is sometimes achieved at the cost of implementing a large shunt resistor, compared to the TIA design. Large shunt resistors, impose higher RC time constants which correspond with wider output pulses. In addition, the gain of this structure is depending on the signal size and the currents flow through the device [62].

Table 2.2: SiPM readout energy resolution based on Scintillator type.

| **Reference** | [222] | [223] | [224] | [19] | [19] |
|---|---|---|---|---|---|
| **Year** | 2016 | 2019 | 2017 | 2019 | 2019 |
| **Scintillator** | LaBr3:Ce | CeBr3 | LaBr3(Ce) | LaBr3(Ce) | LaBr3(Ce) co doped Sr |
| **SiPM** | Custom | SensL | FBK | FBK | FBK |
| **Resolution** | % 4 at 661 KeV | % 4.54 at 661 keV | % 3.19 at 661 keV | % 3.4 at 661 keV | % 2.6 at 661 keV |

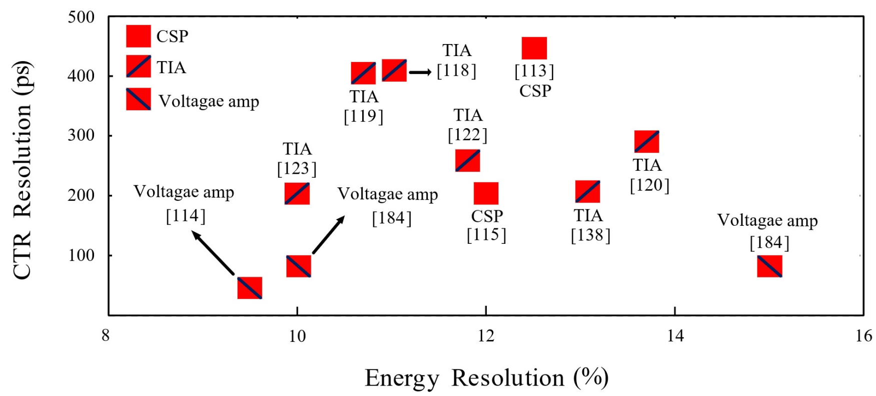


**Figure 2.13:** Time and energy resolution of different readout topologies (charge amplifier (CSP), transimpedance amplifier (TIA) and voltage amplifier [5, 6, 7, 10, 11, 13, 14, 37, 30].

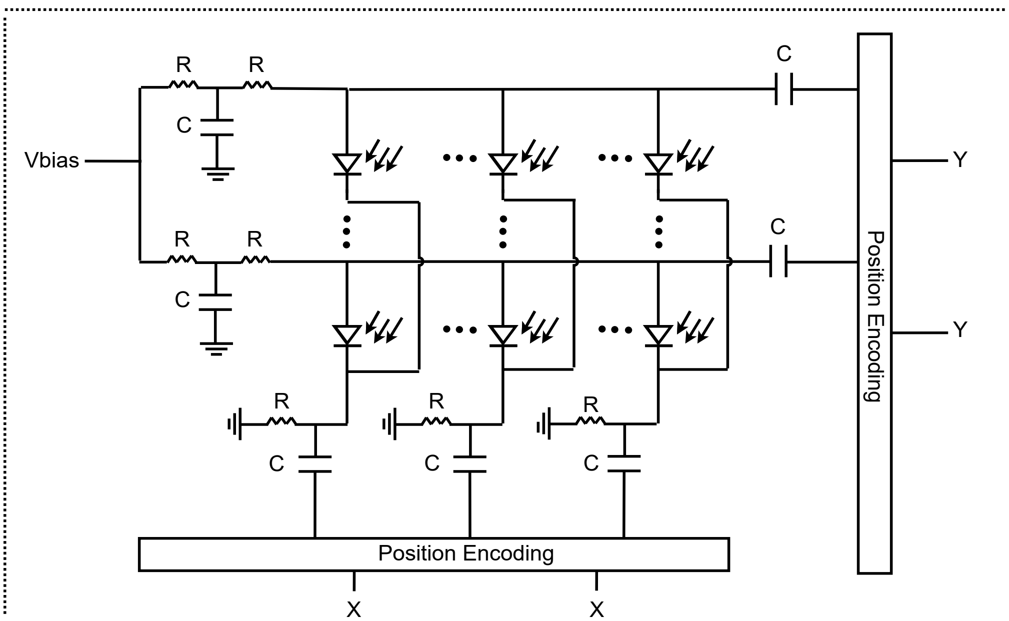


**Figure 2.14:** Position sensing readout based on multiplexing circuit [38].

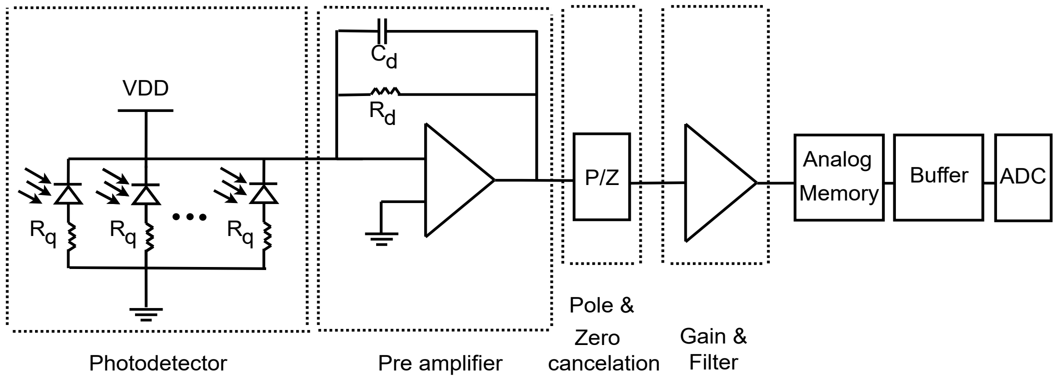


**Figure 2.15:** A typical Application Specific Integrated Circuit for imaging systems pulse processing [33].

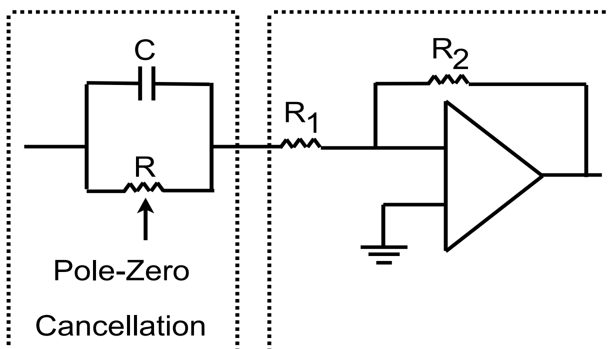


**Figure 2.16:** A typical pole-zero cancellation circuit schematic [33].

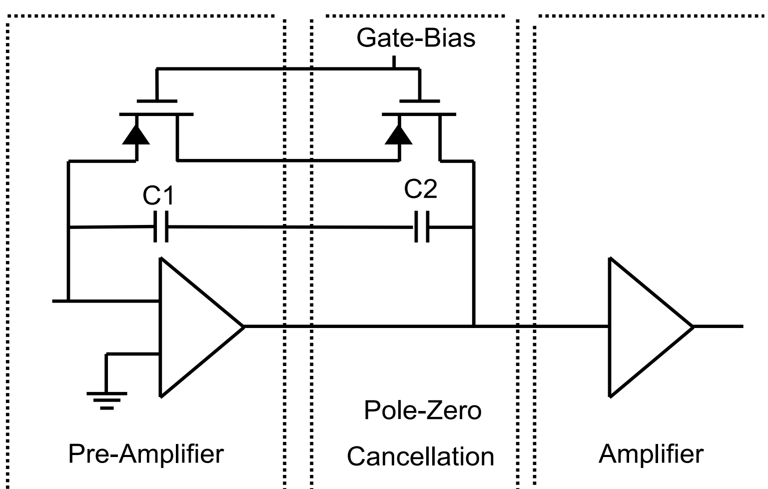


**Figure 2.17:** ASIC pole-zero cancellation schematic in [39].

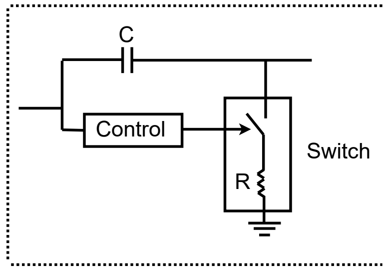


**Figure 2.18:** Baseline restoration circuit [33].

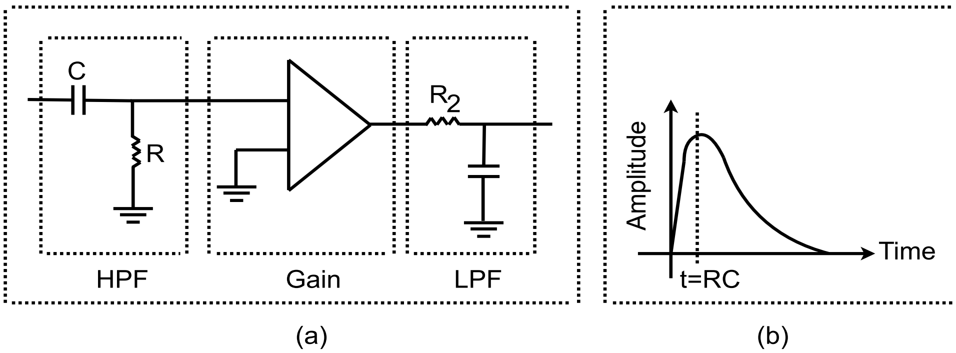


**Figure 2.19:** CR-RC (a) filter circuit and (b) output pulse [40].

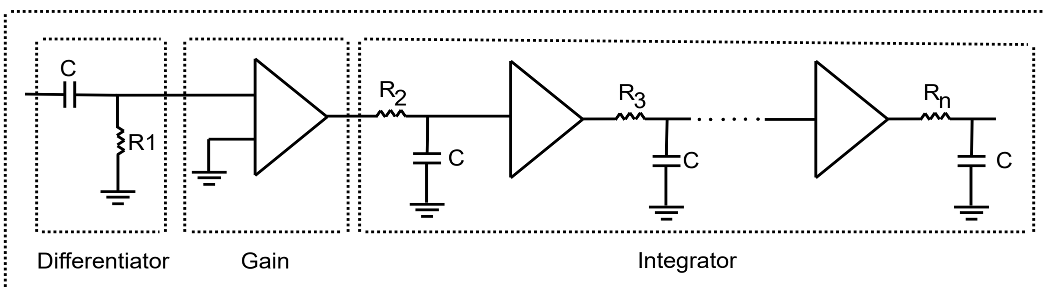


**Figure 2.20:** N order CR-RC Shaper with passive elements[40].

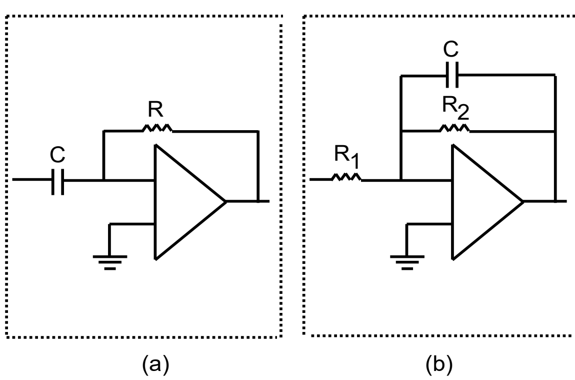


**Figure 2.21:** (a) First order active differentiator and (b) First order integrator [41].

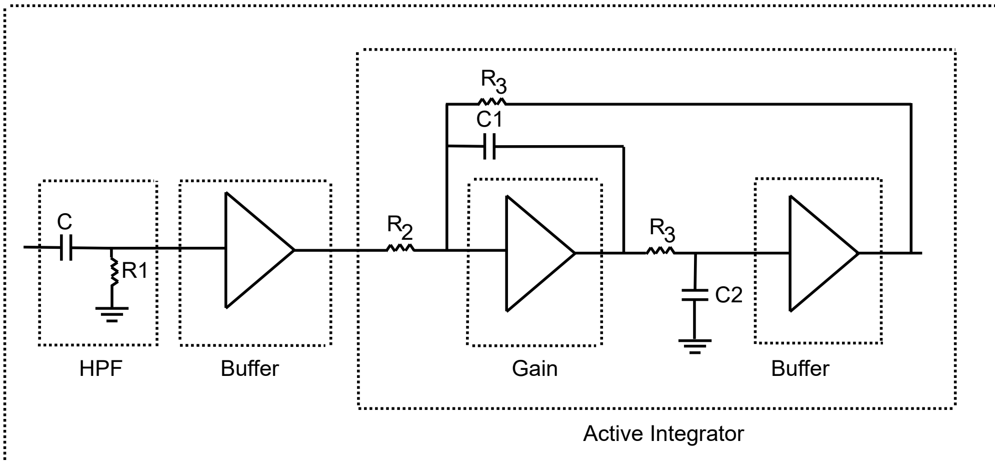


**Figure 2.22:** Gaussian shaper[33].

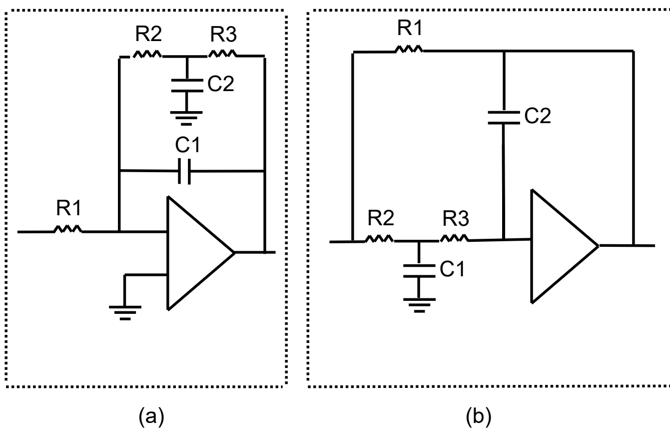


**Figure 2.23:** ASIC shaper discussed in (a) [39] and (b) in [42].

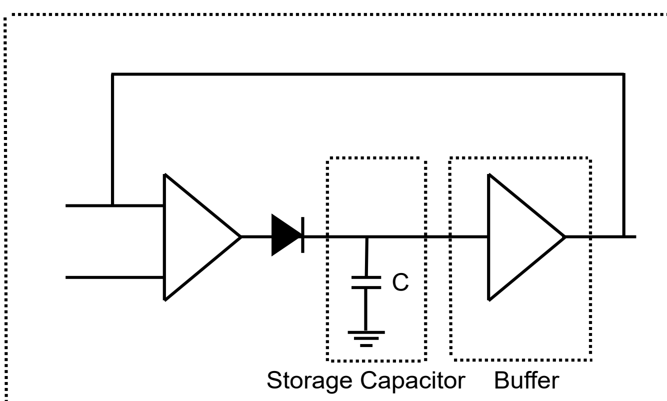


**Figure 2.24:** Simple peak stretcher discussed in [43].

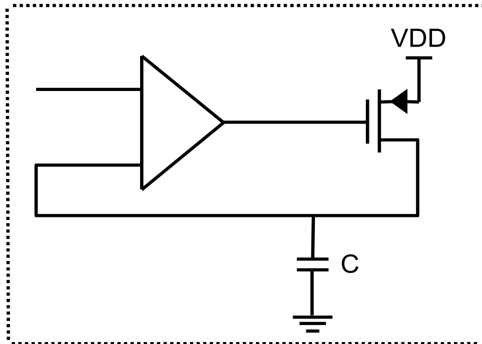


**Figure 2.25:** ASIC PDH discussed in [44].

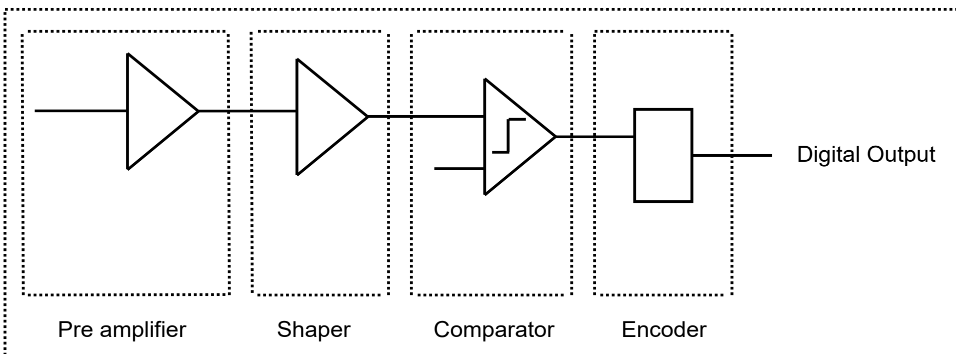


**Figure 2.26:** ASIC spectroscopy building blocks [33].

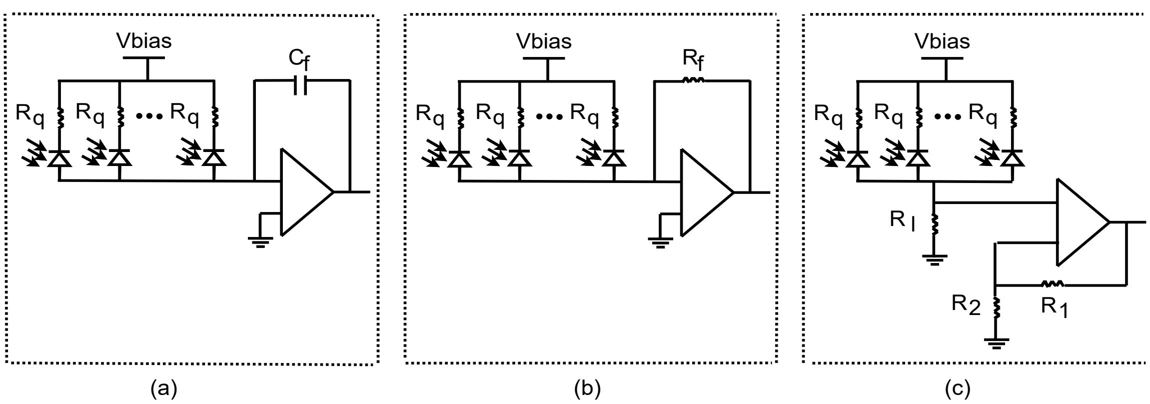


**Figure 2.27:** Typical preamplifier topologies (a) charge amplifier, (b) transimpedance amplifier, and (c) voltage amplifier.

The use of a voltage amplifier requires a resistor in series with the SiPM. The voltage developed across the resistor is then amplified. In some applications further processing may require the output voltage to be converted back into current. To avoid multiple conversions, topologies such as Fig. 2.28 (a), have been discussed in [45].

To achieve better performance, the current mirror that is used in [45], can be replaced with improved topologies with higher output impedance by cascoding or regulated drain structures. These alternative topologies employing feedback such as Fig. 2.28 (b) and (c) have also been implemented in 350 nm CMOS processes [46], where (b) achieves higher dynamic range and tunability and (c) is optimized for bandwidth and input impedance. In [225] the voltage amplifier is coupled with TIA. In this method, the width of the input current pulses is controlled by the circuit time constant which can be adjusted by TIA's feedback network. Fig. 2.29 shows a comparison of the gain and bandwidth of voltage amplifiers implemented in literature.

### 2.9.2 Charge Sensitive Amplifiers

Charge sensitive amplifiers, due to their good noise performance, are another candidate for SiPM readout circuits, spatially when dealing with low input charge and low output noise is a severe requirement. Low gain silicon photomultipliers with small sized microcell, and consequently, low equivalent capacitance, can be easily read-out with charge sensitive amplifier. Various topologies in [226, 45, 61, 227, 129, 228, 229, 230, 231, 232, 233, 234, 35, 235, 236, 237, 53, 46] used a charge amplifier as their photodetector's readout circuit. A typical charge amplifier schematic is shown in Fig. 2.30. This approach while showing good noise performance can have some significant design contraints that prevent proper representation of the the dull dynamic range of the output.

A challenge for CMOS based charge amplifiers is the relatively large area capacitor. A typical capacitor may be 10 times as large as typical analog sized transistor. The capacitor has to discharge periodically.

This can be performed using feedback resistors, transistors and other novel active devices [238, 239, 220, 240]. Passive resistance is common, however the large value has implications on the opamp DC characteristics and requires large area if implemented in integrated circuits. $R_f$ can be implemented with MOS transistors to reduce area and provide greater design flexibility [241]. The offset, bandwidth, power consumption, dynamic range, and gain of CSP, are function of the feedback components [242, 243, 58, 244].

A charge sensitive preamplifier has an output voltage that is proportional to the integrated input current. A typical architecture consists of an operational amplifier, a capacitor in the feedback path, and a reset switch or circuit. The reset circuit discharges the feedback capacitor, otherwise the output voltage eventually saturates. High input impedance guarantees the current flows primarily through the feedback capacitor. Due to Miller effect, the feedback capacitor ($C_f$), appears as large capacitance at the input ($C_{eff}$=(1+A)$C_f$) which is in parallel with other parasitic input capacitances.

Thus, the gain of this structure is proportional to the feedback capacitance and is relatively independent of the devices capacitances. The feedback network can be implemented using passive or active components.

The advantage of active feedback (transistors) over passive networks (RC) lies in the active devices' lower noise and tunability. In addition, small chip area is required to implement the circuit. An active feedback with leakage current compensation is highlighted in [238]. Ref [239] uses an active feedback network for gamma-ray tracking detectors with a low gain, noninverting amplifier between the charge amplifier and the feedback resistance. Thus, the discharge time constant can be made shorter, while leaving the RC network unchanged. In another work, an active feedback network is designed upon two different active feedbacks based on the mosfet devices and a voltage-controlled switch as reset network. Using this technique, the device can operate at as high as 4.5 MHz and can read out 1 to $10^4$ photons with an energy of 1 and 10 keV [245]. In [242], a two amplifier feedback network replaces the large resistor. One amplifier maintains the DC offset voltage at zero and the other one constitutes the negative feedback around the main amplifier.

The Opamps used for charge amplifier can be based on BJT transistors [246, 247] or MOSFET and JFET transistors [248, 249, 250]. JFET and BJT based opamps are widely available commercially. In comparison to MOSFET, JFET CSPs provide better noise performance. A noise model for JFET CSPs can be found in [248]. The result of this work revealed that at 10 kHz, the JFET amplifier's input-referred inherent noise exhibited 22 dB improvement as oppose to MOS based charge amplifier.

However, MOSFET based approaches can offer reduced size and the ability to integrate the SiPM with the amplifier on the same chip [220, 206, 55, 251, 252]. BiCMOS (Bipolar and CMOS on the same die) technologies is less radiation hard compared to CMOS [55], and in general CMOS is less radiation tolerant than SOI (Silicon on insulator) [253, 254]. The irradiation tests in [55] demonstrate that, with high input gamma-rays, the CSPs output amplitude signal and the SNR reduces up to 34.3% and 11.6 dB. Moreover, the fall time also increases significantly from 201 ns to 1730 ns. This research also indicates that MOS transistors are more tolerant to radiation sources and provide better performance than BiCMOS.

As an example, for application with large input charge, with high gain detector, large feedback capacitor is needed for charge integration. Let consider a case with 2250 photo electron, and SiPM gain of $10^6$. Eq. 2.14 indicate that this is equivalet to 360 pC charge,

$$2000 * 1.6 * 10^{-19} * 10^{6} = 360pC \tag{2.14}$$

correspond capacitor that is need for integration of this amount of charge, in 180nm CMOS process with 1.8 V power supply as is shown in Eq. 2.15 is equal to 200 picoFarad,

$$C = Q/V, C = (360 * 10^{-12}/1.8) = 200pF \tag{2.15}$$

This capacitor take a quite a large die area and is not of designer interest. Plus, for SiPM fast rising detection, the readout circuit must be able to drive large feedback capacitors and simultaneously provide large bandwidth which can be obtain at the cost of larger power consumption. Large feedback that is needed in charge amplifiers, is a limited factor spatially when we are dealing with high count rate applications.[226, 255]. Large feedback capacitor limits the dynamic range and speed of operation [45]. Fig. 2.31 and table 2.3, shows a comparison of the gain and bandwidth of charge amplifiers and SiPM readout circuit based on Charge amplifier implemented in literature.

As an alternative for CSP, In [226, 255, 226, 45], a novel prototype called BASIC based on a current buffer that avoid high input impedance in signal path, is discussed which provide both timing and energy information of SiPMs signals. The prototype is designed and fabricated in discussed circuit was designed in 0.35 $\mu$m CMOS technology and depicted in Fig. 2.28(a).

### 2.9.3 Current Sensitive Amplifiers

Depending on the application, current sensitive amplifiers which are also known as transimpedance amplifier are able to use as part of readout circuit of SiPM based detectors. [221, 256, 62, 257, 258, 259, 260, 261, 103, 63, 262, 263, 225, 69, 264]. Transimpedance preamplifiers converts input current pulses into an output voltage signal. Transimpedance preamplifiers aim to have a low input impedance which can guarantee fast timing resolution of the SiPM's output signals.

The main challenge of this approach is the usually large equivalent parasitic capacitor of SiPMs. For large value of feedback resistor and consequently large gain, the pole formed by feedback resistor and SiPM's equivalent parasitic capacitor may cause stability problem in the input of amplifier. One way to eliminate the stability problem is adding capacitance in parallel to feedback resistor [221]. The basic structure of a current-sensitive (transimpedance) amplifier is shown in Fig. 2.32. This structure is made of an operational amplifier with a feedback resistor.

The advantage of transimpedance amplifier over charge sensitive amplifier is that this structure eliminate the need for pole-zero cancellation that is needed with CSP readout circuit due to large decay time of CSP's output signals. Transfer function of transimpedance structure that is depicted in Fig. 2.32, is shown in Eq. 2.16, where $\tau$ is the RC time constant calculated through equivalent resistor and capacitor at the input port of amplifier. Input impedance of this structure can be easily calculated through the Eq. 2.16. This equation proves that by choosing a proper value for feedback resistor, one can guarantee that SiPMs output current flow directly through the feedback resistor without charging up input capacitance of preamplifier stage.

$$\frac{V_{out}(S)}{I_{in}(S)} = -\frac{R_f}{1+\tau S} \tag{2.16}$$

From 2.16, it is obvious that proper choice of $R_f$, has direct effect on gain, noise and bandwidth of transimpedance amplifier. As an example, by increasing the value of $R_f$, while the gain increase and thermal noise decreases, the bandwidth also decreases. While the discussed circuit in Fig. 2.32 looks pretty easy for implementation, there are some other consideration regarding this structure that are needs to take into account. Lets take a look at input impedance of transimpedance amplifier that is shown in Eq. 2.17.

$$Z_{in} = \frac{R_f}{g_m R_o} + \frac{sR_f C_o}{g_m} = \frac{R_f}{g_m}[\frac{1}{R_o} + sC_o] \tag{2.17}$$

The inductive behaviour of the transimpedance amplifier structure is given by $[R_f\ C_o]/g_m$ in Eq. 2.17 indicates that this structure, when dealing with SiPM detectors with large equivalent capacitance, has the potential to oscillate which needs to be addressed before implementation of the readout circuit.

As an alternative to discussed circuit in Fig. 2.32, a low noise, large bandwidth TIP depicted in Fig. 2.33, discussed in [265]. This structure has the same configuration as CSP and aim from a parallel capacitor with feedback resistor in order to block the possible oscillation due to inductive behaviour of TIPs. Transfer function of this structure is shown in Eq. 2.18. From Eq. 2.18, one can conclude that if the time constant of load (compensation) network is equal to feedback network then the output voltage is free of possible oscillation and will be equal to $R_f/R_o$ or $C_f/C_o$.

$$V_{out}(S) = -\frac{QC_o}{C_f} + R_2\frac{(S+1)R_f C_f}{(S+1)R_o C_o} \tag{2.18}$$

In [61], a transimpedance preamplifier (TIP) as part of readout circuit of SiPM based detector based on the Pole-zero cancellation technique has been implemented to optimize the performance of the NUV-HD SiPM to work with Cherenkov Telescope Array (CTA). The schematic of discreet readout circuit is depicted in Fig. 2.34.

**Table 2.3:** Comparison table of SiPM readout circuit based on charge amplifier.

| **Reference** | [226] | [45] | [61] | [227] |
|---|---|---|---|---|
| **Application** | Medical imaging | Medical imaging | Telescope Array | Hadron Therapy |
| **Measured Quantity** | Energy Time | Energy Time | Energy - | Energy Time |
| **SiPM** | FBK-irst | FBK-irst Hamamatsu | FBK | Hamamatsu |
| **Light** | LED | LED | LED | - |
| **Scintillator** | - | - | - | LaBr3 |
| **Chip** | - | - | Advansid | ASIC |
| | [228] | [229] | [230] | [231] |
| **Application** | | Gamma Camera | | Spectrometry |
| **Measured Quantity** | Energy Time | Energy | Energy | Energy |
| **SiPM** | Hamamatsu | SensL | SensL Hamamatsu Ketek | Hamamatsu |
| **Light** | - | - | Gamma-ray | - |
| **Scintillator** | LYSO | CsI(Tl) | - | LSO |
| **Chip** | ASIC | AD8048 | Cremat | ORTEC |
| | [236] | [237] | [53] | [46] |
| **Application** | TPC | PET | Calorimeter | Medical |
| **Measured Quantity** | Energy Time | Energy Time | Energy Time | Energy Time |
| **SiPM** | FBK | FBK-Irst | FBK-Irst | ITC-irst |
| **Light** | Xenon | LED | LED | laser |
| **Scintillator** | - | - | - | - |
| **Chip** | Cremat | ASIC | ASIC | - |

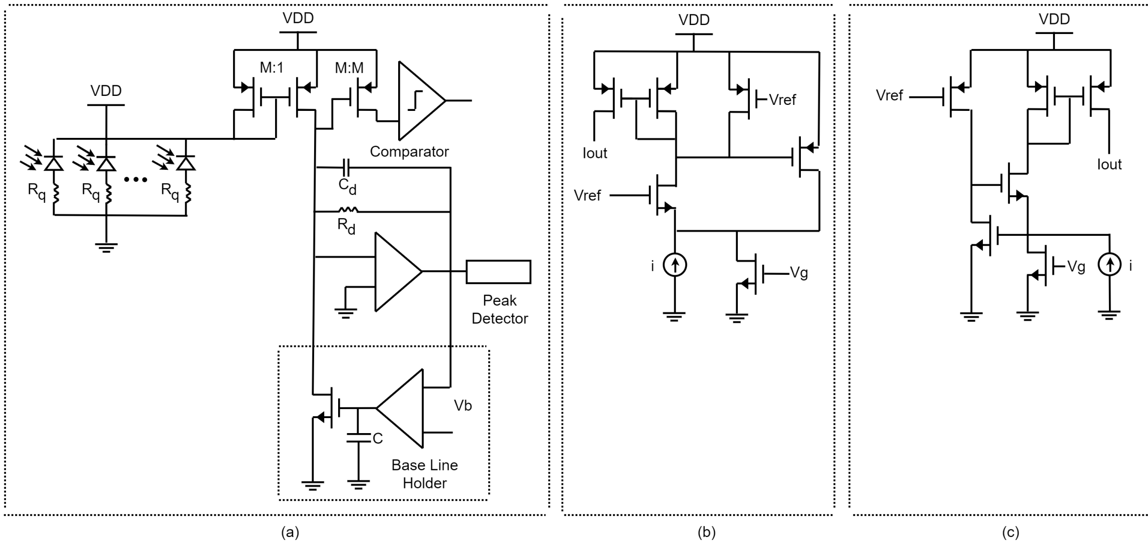


**Figure 2.28:** (a) Current mode readout circuit discussed in [45]. Alternative current mode readout toplogies for the current buffer (b) and (c) where $i$ represents the SiPM current [46].

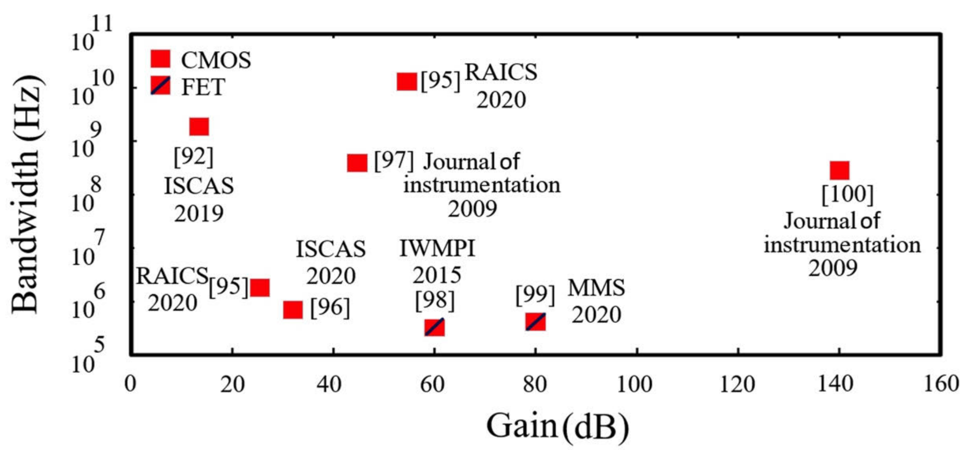


**Figure 2.29:** Gain and bandwidth of voltage amplifiers discussed in [47, 48, 49, 50, 51, 52, 53].

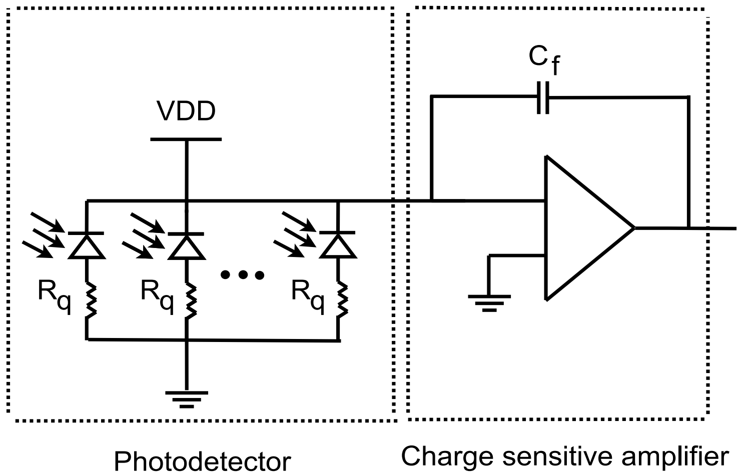


**Figure 2.30:** Charge sensitive amplifier (CSA) coupled to a SiPM.

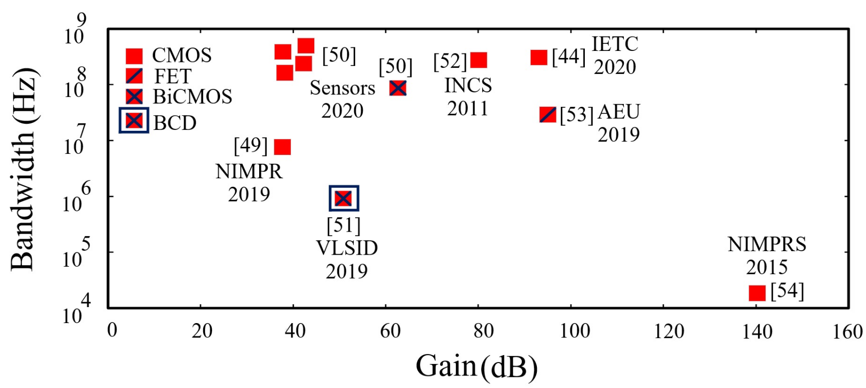


**Figure 2.31:** Gain and bandwidth of charge amplifiers discussed in [54, 55, 56, 57, 58, 59, 60].

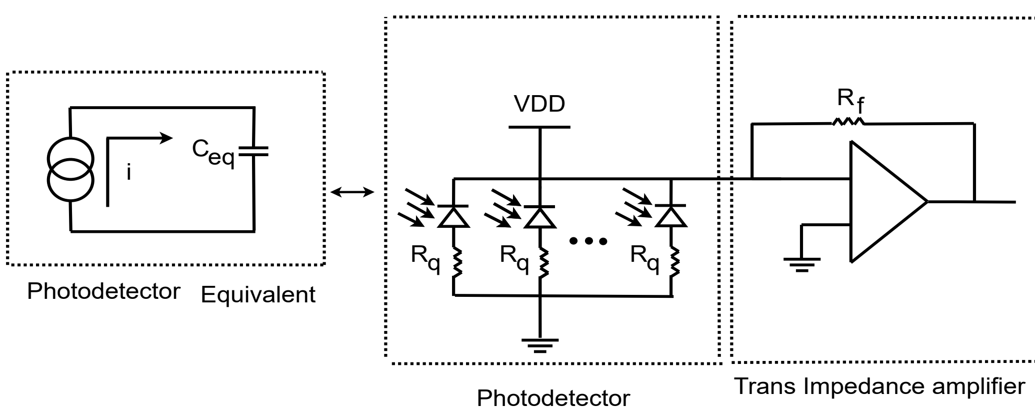


**Figure 2.32:** Transimpedance amplifier coupled with SiPM.

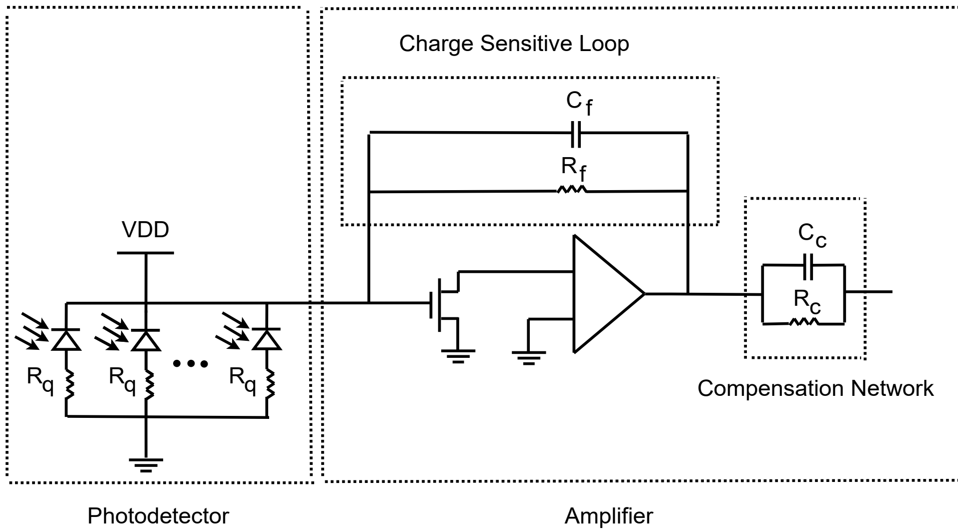


**Figure 2.33:** Transimpedance preamplifier with charge sensitive loop [33].

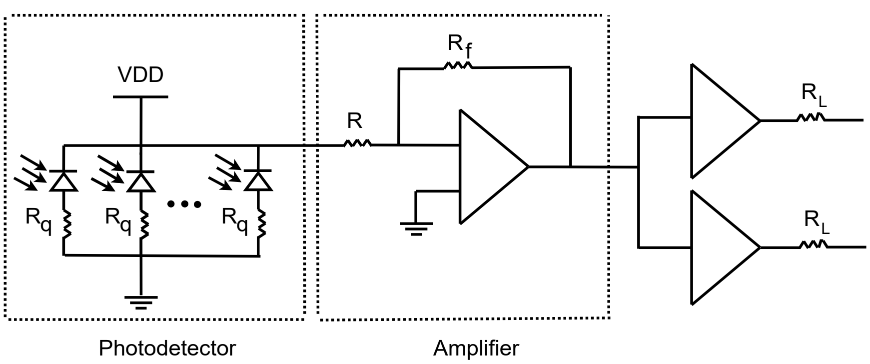


**Figure 2.34:** SiPM readout based on pole-zero cancellation technique, discussed in [61].

The SiPM is mounted on top of an evaluation circuit board from Advansid group and an LED is used as light source to test the SiPM and readout circuit. Undershoot, offset and tail of output signal, are able to modify through 3 micro switch from outside of the board. The experiment result indicated that using the discussed discreet preamplifier an output signal with few tens of ns duration and no tail and offset is achievable.

The conventional preamplifier used in nuclear imaging systems comprise charge sensitive and shaping amplifier [66]. An ideal nuclear imaging system needs to be fast, with small rise time and dynamic slew rate correction and be low power and small sized for radiation detection readout [266, 267]. However even with design techniques, the CSP's slew rate is in the microseconds range [67]. In practice, CSP and shaping amplifier can be substituted with a transimpedance amplifier, where the current can be directly converted into an output voltage [268].

In general a typical TIA implementation using off the shelf discrete components is a feedback resistor with an amplifier. For large gain, the input resistance, $R_{in}$=$R_f/(A+1)$, is minimized. The TIA input slew rate is a function of input RC time constant. Lower RC gives higher slew rate, and is suitable particularly for high count rate applications [268, 66, 62, 260, 261, 63, 225].

The input impedance of a transimpedance amplifier is,

$$Z_{in} = \tfrac{R_f}{g_m R_o} + \tfrac{sR_f C_o}{g_m} = \tfrac{R_f}{g_m}\left(\tfrac{1}{R_o} + sC_o\right) \tag{2.19}$$

where $R_f$ is the resistor in the feedback path, $g_m$ is the transconductance gain, $C_0$ is the internal capacitance of amplifier, and $R_0$ is load resistance. This can cause oscillations when coupled with the large input capacitance from a SiPM. To mitigate this, a capacitance is placed in parallel with the feedback resistor. The large feedback resistor may be implemented by a MOS device operating in triode [269, 270]. In order to detect and transform a nanosecond-wide signals, the TIA requires a large bandwidth. A TIA's bandwidth can be written as,

$$BW_{TIA} = \sqrt{\frac{GBW}{2\pi R_F C_D}} \tag{2.20}$$

where $BW_{TIA}$ is the bandwidth, $R_F$ is the resistance, $GBW$ is the gain bandwidth product, and $C_D$ is the detector capacitance. The $GBW$ is a constant for the open loop opamp or OTA structure. In [67], in order to increase the bandwidth, two inductors are series with the TIA. There are multiple approaches to implement a suitable TIA for nuclear imaging [271]. [260] proposes a TIA based on second generation voltage conveyors (VCII). This current conveyer has been implemented using discrete components [261, 63]. VCII, compared to the first generation, provides variable front-end gain and low impedance at the input of VCII that helps to decrease the effect of usually large output parasitic capacitance associated with SiPM.

Common base and common gate amplifiers provide low input impedance and do not require feedback resistances. These single transistor amplifier architectures may be modified into regulated structures or incorporate cascoding to improve performance. [69, 272]. In order to achieve the best performance with a regulated common gate TIA, such as that discussed in [272], the DC output voltage of the TIA needs to close to the overdrive voltage, $V_{DSAT}$, of the input transistor and the load resistor needs to be approximately ten times larger than the drain to source resistance. Similar to CSPs, TIAs can also be made of technologies other than CMOS. The first TIA using organic thin-film transistors was discussed in [270], where the TIA was based on voltage-controlled resistor and common gate input stage.

A multi-channel readout based on a transimpedance topology was discussed in [62] (Fig. 2.35), where in order to prevent the possible oscillations, a series resistor ($R_s$) was placed between the common anode of the SiPM and the input port of the operational amplifier. In this design, the inductors represent the parasitic inductances presented by the metal lines, wires, and printed circuit board. In order to modify offset, output signal tail and the undershoot, [61] uses trimmers. A TIA implemented in SiGe BiCMOS that used a transformer-based input stage for improved frequency response was discussed in response [273]. Fig. 2.36 shows the gain and bandwidth of a few transimpedance amplifiers that have been implemented.

## 2.10 Bulk-Driven Amplifier Design

In new advanced MOS fabrication technologies, the threshold voltage of the MOS devices have not quite changed as compared with old technologies. However, the size of gate is quite reduced and forces the designer to use lower power supply voltages in their design. One technique to overcome this difficulty is based on body-driven MOSFETs [274].

In this approach, the input signal, instead of the gate, is applied to the body terminal of MOSFET. In recent years, many low voltage body-driven analog circuits, including differential amplifiers [275, 276], voltage references [277], and current mirrors [278] have been presented. Among these, the operational amplifier is one of the most essential building blocks, that is needed in variety of applications, including analog interface with SiPM readout. Body-driven designs provide the opportunity to use supply voltages less than 1V and is thus advantageous to portable applications.

However, this benefit, comes with few drawbacks, such as lower intrinsic gain ($g_m$), as the back gate transconductance is typically smaller than the transistor transconductance by apprximately a factor of three to five. In order to mitigate the effect of low intrinsic gain, some works have proposed the concept of partial positive feedback [279], where the positive feedback loop, partially boosts the transconductance.

Another design technique that has been used in this work is based on the cross-coupled technique. This technique, was introduced in 1919 in two independent papers, where both papers exploited the cross-coupled pair to create a multivibrator. In the 1960s, it was realized that cross-coupling technique could help to amplify even small differences of applied signals in differential amplifiers [72]. Fig. 2.37, shows a typical cross-coupled amplifier.

In addition to body drive and cross-coupling technique to boost the gain of amplifier, we have applied the self biasing technique to reduce overall power consumption of readout circuit and to minimize the number of input pads and external circuitry required. A few self bias structures are shown in Fig. 2.38(a) through (c), where 10 transistors of a proposed circuit in (a) with the help of the self bias approach, is reduced to 6 transistors in (c), which can eventually reduce the overall power consumption [73].

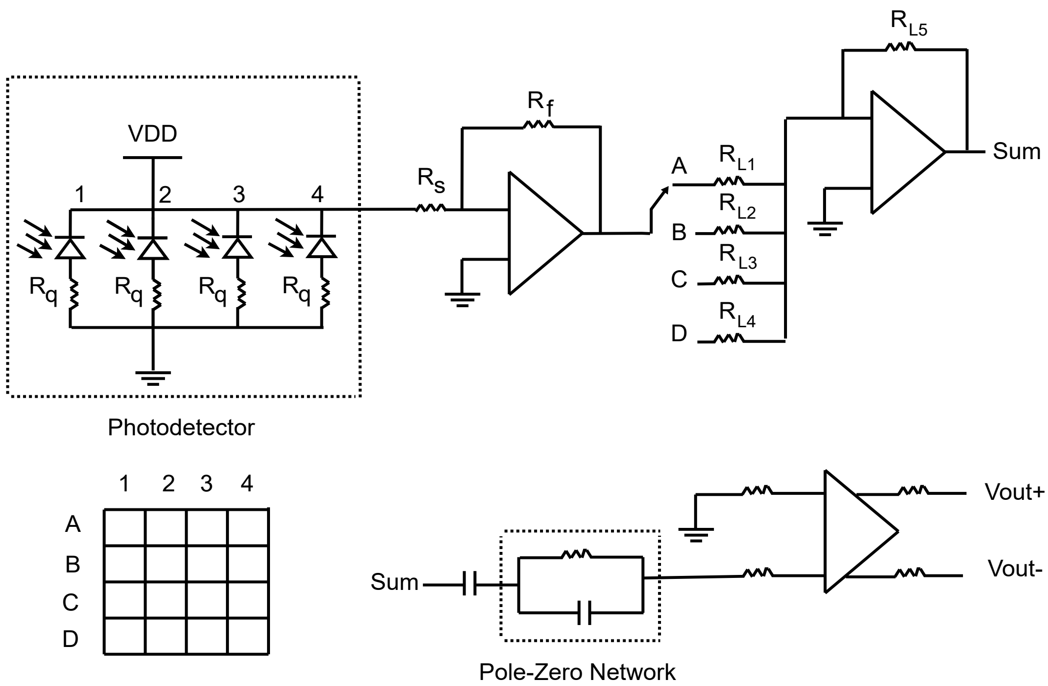


**Figure 2.35:** Multi-channel SiPM's readout based on transimpedance topology discussed in [62].

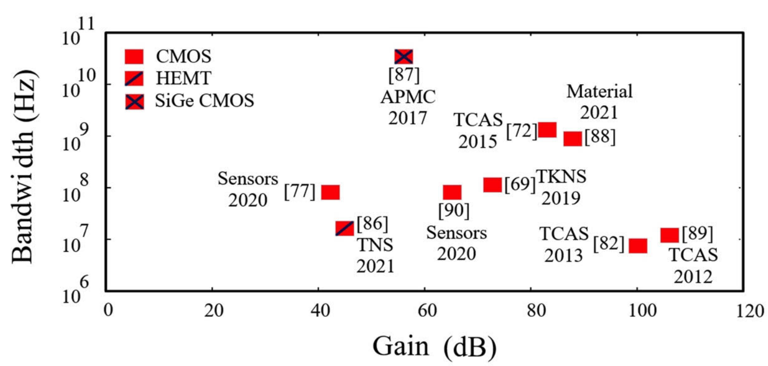


**Figure 2.36:** Gain and bandwidth of transimpedance amplifiers in [63, 64, 65, 66, 67, 68, 69, 70, 71].

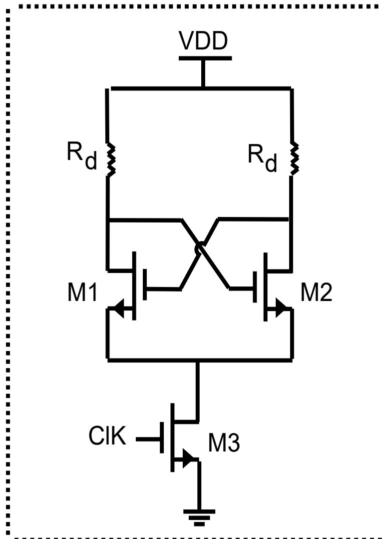


**Figure 2.37:** Typical cross-coupled amplifier, discussed in [72].

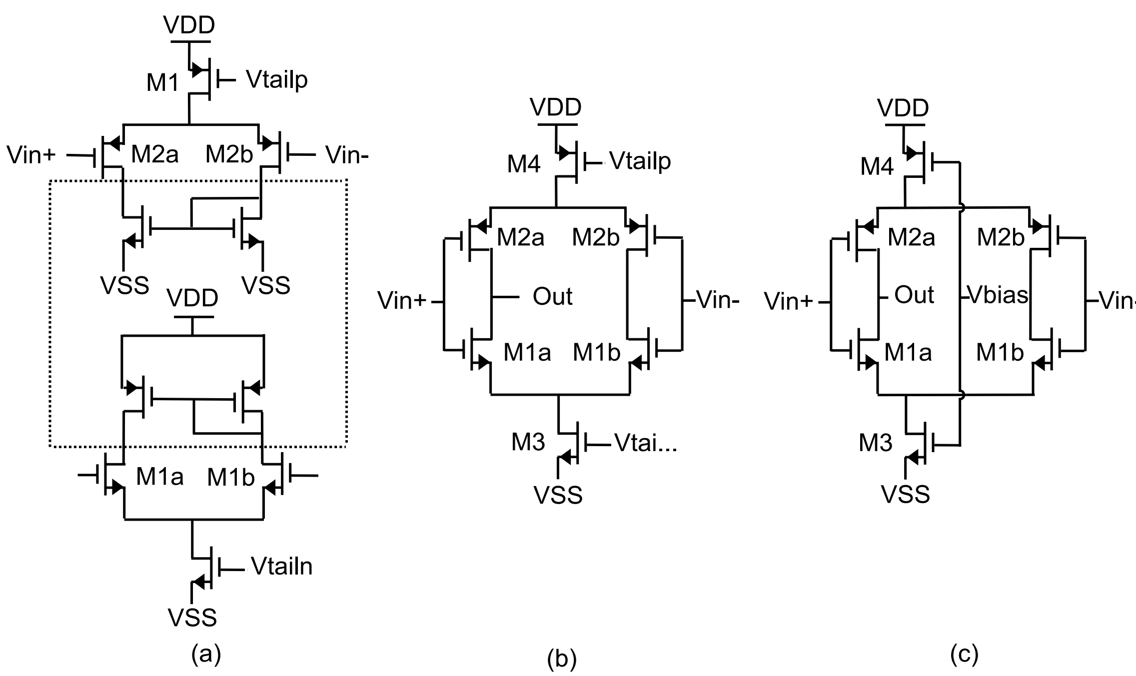


**Figure 2.38:** Self-biased strategy discussed in [73].

# Chapter 3

# A Bulk Driven OTA for Portable SiPM Based Detectors

**Portions of this chapter were previously published in:**

- S. Hesari, A. Hedayatipour, M. A. Haque, and N. McFarlane, "A Bulk Driven Transimpedance Amplifier for Portable SiPM Based Detectors," *IEEE Sensors,* p. 1-4, 2020.

## 3.1 Transimpedance amplifier design

Transimpedance amplifier is built upon an operational transimpedance amplifier (OTA) combined with a feedback resistor and capacitor. In the most typical OTA topologies, the input voltage signal, by means of a differential pair, is transformed into a current signal. Then, via a current mirror the current signal is passed to following stage and converted to an appropriate output signal. As long as the OTA is driving a capacitive or large resistive load, the voltage gain can be large. Small resistors in the TIA feedback network can load the output of the TIA. To achieve large transconductance for the proposed OTA, the input pair transistors, are biased to work in the sub-threshold region. Sub-threshold region of operation will assist the system to reach maximum transconductance to current ratio. This in turn will lead to the most efficient use of power and ability of the system to operate at a smaller power supply voltage at the expense of the bandwidth.

The operational amplifier proposed in this thesis is based on body driven operational amplifier proposed in [74] (Fig. 3.1(a)). The main advantage of body driven topology is low operating voltage. However, it is at the cost of lower intrinsic gain and large input capacitance. To alleviate this drawback, partial positive feedback is a common approach which helps to boost the transconductance and decrease the input referred noise [280].

As shown in Fig. 3.1(a), M1a and M1b are the differential pair, where both of them are biased through M2a and M2b, which are the diode connected transistors. From the schematic, it can be seen that the bulk terminal of M2a and M2b are cross connected to bulk terminal of M1a and M1b. The input signal may applied to bulk terminals of M1a, M2b on one side and M1b, M2a on the other side, therefore modulating their threshold voltages. Then M1a and M1b are feeding through the gate-drain voltage of transistor M2a and M2b. This topology enable us to control the input pairs through their bulk and gates. In addition, modification of the currents of M1a and M1b, results in increased transconductance of the structure.

One of the main advantage of this structure over the conventional approach (Fig. 3.1(b)) is better output voltage swing. The basic bulk driven approach gives,

$$\begin{gathered} V_{max,out} = V_{DD} - V_{DSsat} \\ V_{min,out} = V_{DSsat} \end{gathered} \tag{3.1}$$

This structure, in comparison with output voltage swing of conventional body driven amplifier, given by Eq. 3.2, provide better output voltage swing.

$$\begin{gathered} V_{max,out} = V_{DD} - 2V_{DSsat} \\ V_{min,out} = V_{DSsat} \end{gathered} \tag{3.2}$$

The dc differential transconductance gain of this structure is given by Eq. 3.3:

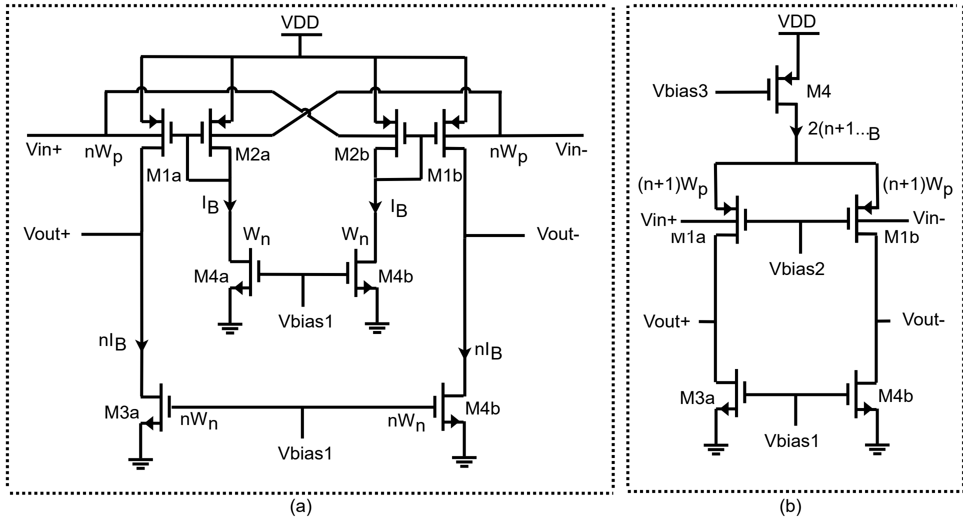


**Figure 3.1:** (a) Body driven amplifier proposed in [74], and (b) conventional body driven differential pair.

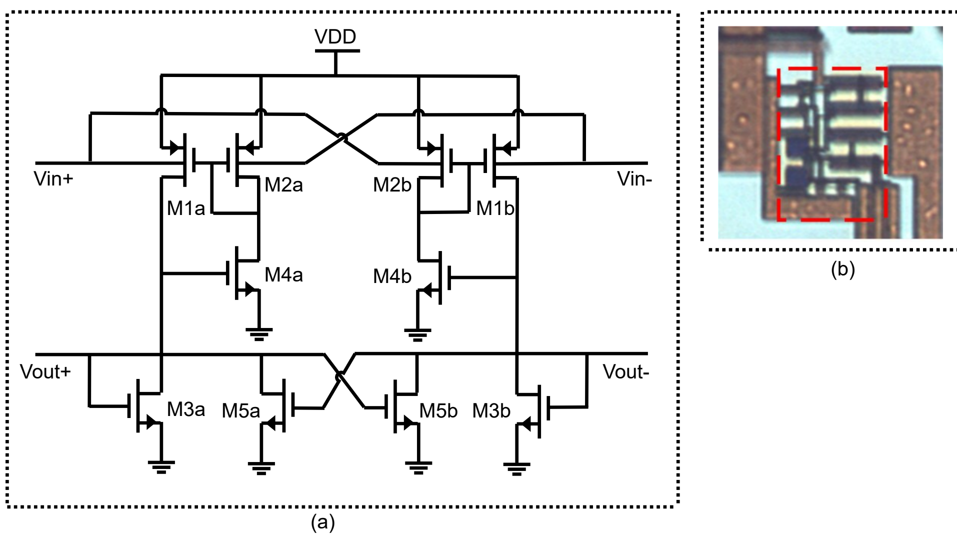


**Figure 3.2:** (a) Two stage OTA with input pair enhancement and (b) Photomicrograph of the fabricated OTA.

$$g_{meff,1a} = g_{mb1}\left(1 + \frac{g_{m1}}{g_{mb1}}\frac{g_{mb2}}{g_{m2} + g_{ds2} + g_{ds4}}\right) \tag{3.3}$$

From this expression, the effective transconductance is increased. If we compare the $g_{meff,1b}$ and considering $g_{meff,1b}$ equal to $2g_{mb1}$, then we obtain Eq. 3.4.

$$g_{meff,1a} = 2\left(\frac{n}{n+1}\right) g_{meff,1b} \tag{3.4}$$

Where n is the biasing currents ratio for transistors M1a,b and M2a,b. From the equation it can be seen that for n=1, M1a,b and M2a,b have the same transconductance. However for higher value of n, $g_{meff,1a}$ will increases and approaches to $2g_{meff,1b}$. Considering that output conductance of transistors are about their drain current value, then the output conductance of structure in Fig. 3.1(a) and (b) can be given by Eq. 3.5.

$$g_{out,1a} = (g_{ds1} + g_{ds3}) = 2\left(\frac{n}{n+1}\right) g_{out,1b} \tag{3.5}$$

Therefore from Eq. 3.4 and Eq. 3.5, dc voltage gain of Fig. 3.1(a) is twice as conventional body driven amplifier.

Although proposed design in [74], depicted in Fig. 3.1(a), provide higher gain value, in comparison with conventional body driven amplifier(Fig. 3.1(b)), but it is noticeable that in bulk driven topologies, the gain can be significantly reduced since the transconductance of the body is 3 to 5 times less than the trans-conductance of gate. Our approach to mitigate this drawback is the cross connection of transistors M3a, M5a, M3b and M5b. The schematic of the operational amplifier proposed in this work is shown in Fig. 3.2.

In this structure, the differential input signal is applied to the body of MOSFET transistors $M_{1a,2b}$ and $M_{1b,2a}$. $M_1$ and $M_2$ are also current mirrors. $M_{4a}$ and $M_{4b}$ are an amplification stage and the cross coupled transistors $M_{3a}$, $M_{3b}$, $M_{5a}$ and $M_{5b}$, provide partial positive feedback to improve the transconductance. The biasing currents have been chosen to be equal to 3 $\mu$A, which, assumed for W/L value of transistors. From small signal analysis, the dc voltage gain of proposed amplifier can be approximated by Eq. 3.6,

$$\frac{V_{out}}{V_{in}} = \frac{g_{mb1}+\frac{g_{m1}g_{mb2}}{g_{m2}}}{g_{m3}-g_{m5}+\frac{g_{m1}g_{mb4}}{g_{m2}}} \tag{3.6}$$

where $g_m$ is the transconductance, $g_{mb}$ is the back gate transconductance, and $r_o$ is the output resistance of each transistor. The gain increase is due to the subtraction of the terms $g_{m3}$ and $g_{m5}$. Assuming large $r_o$, the other terms are small. The aspect ratios are chosen to minimize the denominator and increase the gain. A 10 kΩ feedback resistor provided 10 kΩ transimpedance gain. This combined with the 10 pF capacitor resulted in a 1.5 MHz bandwidth. If we consider the effect of back gate transconductance and output resistance of each transistor, The gain is, can be given by Eq. 3.7.

$$A_v = \frac{g_{mb1} + \frac{g_{m1}g_{mb2}r_{o2}}{1+g_{m2}r_{o2}}}{\frac{g_{m4}g_{m1}r_{o2}}{1+g_{m2}r_{o2}} + g_{m3} - g_{m5} + \frac{1}{r_{o1}}} \tag{3.7}$$

Transistor sizes of this structure for $M_{1a}$, $M_{2a}$, $M_{1b}$, $M_{2b}$ is (W/L)=(8 $\mu$m/0.18 $\mu$), for $M_{4a}$ and $M_{4b}$ is (W/L)=(3 $\mu$m/3 $\mu$) and for $M_{3a}$, $M_{3b}$, $M_{5a}$ and $M_{5b}$ is (W/L)=(1 $\mu$m/0.18 $\mu$m).

From the small signal analysis it is obvious that proposed structure, compared to conventional amplifiers is able to provide higher output voltage swing which is important when the TIA is coupled with SiPM.

The common-mode rejection ratio (CMRR) and power supply rejection ratio (PSRR) for the TIA of this work, can be determined considering the single outputs as it is given by Eq. 3.8.

$$CMRR = \frac{g_{m2} + (g_{ds2} + g_{ds4})/2}{g_{ds2} + g_{ds4}} \tag{3.8}$$

The dc PSRR for this structure when the inputs shorted to ground for ac signals can be given by Eq. 3.9. Where n is the biasing currents ratio for transistors M1a,b and M2a,b.

$$PSRR = \frac{2g_{mb1}}{g_{ds1} + n[g_{ds4}(1 + ((g_{mb2})/(g_{m2})) + g_{ds2}(g_{mb2})/(g_{m2}))]} \tag{3.9}$$

## 3.2 TIA Noise Analysis

In a SiPM, the major source of noise is the dark current due to thermally generated carriers that start an avalanche in the high field areas. The dark current can also be caused due to band to band tunneling and minority carrier diffusion. The RMS output noise voltage of a TIA is,

$$V_{no_{rms}}^2 = \frac{R_f^2 C_d^2 kT}{g_m(\tau_1 + \tau_2)\tau_1\tau_2} \tag{3.10}$$

where $V_{no_{rms}}^2$ is the rms output noise voltage, $k$ is Boltzmann's constant, $T$ is the temperature, $\tau_1$ and $\tau_2$ are time constants ($R_f$, $C_f$, and $C_d$ ). $C_d$ is SiPM parasitic capacitance of the device and is explicitly shown in Fig. 3.3 and $R_f$ can be in the range of 100 $\Omega$ to 1 $M\Omega$ depending on the input current levels.[70] To minimize the noise of TIAs, $g_m$ should be high. However, a high $g_m$ requires more current, increases the power consumption, transistor area, and parasitics. Bulk driven techniques have been used to alleviate some of these issues [281].

Other solutions have incorporated techniques such as quasi-floating gate techniques, auxiliary amplifiers, and source degeneration. This work seeks to ultimately integrate the TIA with a SiPM on the same chip. While the SiPM operates at a relatively high reverse bias voltages, for a portable detector the TIA should operate at low voltages and should be compact so as not to reduce the active area of the SiPM. Therefore, in this work bulk-driven and subthreshold region operating transistors were used to develop the OTA for the TIA. The amplifier is fully differential to help compensate for variations from SiPM to SiPM by using a reference device. The TIA characteristics were experimentally verified, and the integrated TIA with the SiPM was simulated to verify the operation.

### 3.2.1 Input Reffered Noise

Input referred noise of the amplifier is due to thermal noise and flicker noise. The thermal noise is the effect of the random moving of electrons in conductors and the flicker noise is the result of interface between gate oxide and the silicon substrate. Thermal noise is given by,

$$\overline{I_{nT}}^2 = 4kTR \tag{3.11}$$

where, $R$ is the resistance represented by the channel, $k$ is Boltzmann's constant, and $T$ is the absolute temperature in Kelvin.

Flicker noise is given by,

$$\overline{I_{nf}}^2 = K_f \frac{I}{f} \Delta f \tag{3.12}$$

where, $K_f$ is a process dependent constant, $I$ is the bias current, and $f$ is frequency. $K_f$ is a function of the aspect ratio of the device as well as the density of traps at the oxide interface.

The transconductance gain of this structure is,

$$g_{m_{eff}} = g_{mb1} \left( 1 + \frac{g_{m1}}{g_{mb1}} \frac{g_{mb2}}{g_{m2} + g_{ds2} + g_{ds4}} \right) \tag{3.13}$$

Assuming

$$\frac{g_{m1}}{g_{mb1}} = \frac{g_{m2}}{g_{mb2}} \tag{3.14}$$

and

$$g_{m2} \gg g_{ds2} + g_{ds4} \tag{3.15}$$

the body transconductance is,

$$g_{mb1} = \frac{1}{2} g_{m_{eff}}, \tag{3.16}$$

Thus, the input referred thermal noise is,

$$\overline{V_{nT}}^2 = \frac{1}{2} \frac{8KT}{3g_{mb1}} \left( \frac{g_{m1}}{g_{mb1}} + \frac{g_{m3}}{g_{mb1}} + \frac{g_{m5}}{g_{mb1}} \right) \tag{3.17}$$

The input referred flicker noise is,

$$\overline{V_{\frac{1}{f}}}^{2} = \frac{1}{2}\frac{1}{g_{mb1}^{2}C_{ox}f}\left(\frac{K_{fp}g_{m1}^{2}}{W_1L_1} + \frac{K_{fn}g_{m3}^{2}}{W_3L_3} + \frac{K_{fn}g_{m5}^{2}}{W_5L_5}\right). \tag{3.18}$$

## 3.3 TIA Simulations and Experimental Measurements

In this work, we have designed a TIA that can be integrated with a SiPM on the same chip. This will improve the power, noise, and area of the system while decreasing the parasitics which affect the speed and other characteristics of the system. There are a number of topologies which can be used for implementing the readout with a TIA. These include the shunt feedback with resistor topology and shunt feedback with resistor and capacitor topology. The simplified circuit of a SiPM and TIA in these configurations are shown in Fig. 3.3.

In a single photon avalanche diode (SPAD), high values of reverse bias voltages over the device will cause impact ionization and eventually an avalanche current. A SPAD needs to be biased above its breakdown voltage for an avalanche to occur. Implementing the SiPMs in CMOS will allow for lower operating voltages than typical PMTs and commercial SiPMs. Fig. 3.4 (a) and (b) show a CMOS SiPM in a standard 180 nm process and a commercially available SiPM (Hamamatsu S13360) [282]. The custom CMOS SiPM active area is 2 mm $\times$ 2 mm and the microcells dimensions are 20 $\mu$m. The Hamamatsu S13360 is 6 mm $\times$ 6 mm and with microcells dimensions of 50 $\mu$m. Thus, the output voltage transient response of the TIA with the Hamamatsu SiPM is greater than the CMOS SiPM. The TIA was also fabricated in the same 180 nm process. Fig. 3.5 shows the simulation and measurement result of the open loop and closed loop gain of the TIA. The open loop and closed loop gain are 65 dB and 7.1 dB and the gain-margin and phase-margin are 18.69 dB and 93 degree respectively.

The TIA uses an 0.8 V power supply, the total current of the structure is 524 nA, and the total power is 419 nW. Simulation of the TIA with the SiPM was performed in Cadence using a SPAD SPICE model. The model accurately simulates both the IV characteristic and the avalanche and quench process. The transient output current and IV characteristic simulation of a single SPAD is shown in Fig. 3.6 (a) and (b) respectively. The simulated output voltage transient response of the custom SiPM (an array of $3 \times 3$ SPAD) and commercially available SiPM (Hamamatsu S13360) through the TIA is shown in Fig. 3.7 (a) and (b) respectively. A 0.4 V voltage reference is applied to the other input of the fully differential amplifier to simulate a calibrated SiPM. In the simulated experiment, the SiPMs avalanche at different times, simulating a pulsed uniform light source.

Table 3.1 compares the two amplifier systems to other front end amplifiers in recent literature. Although [120] lists better performance than our CMOS implementation, the topology (a pseudo differential common gate structure) was not fabricated. The CMOS implementation shows acceptable performance when compared to others and is comparable to the commercial implementation.

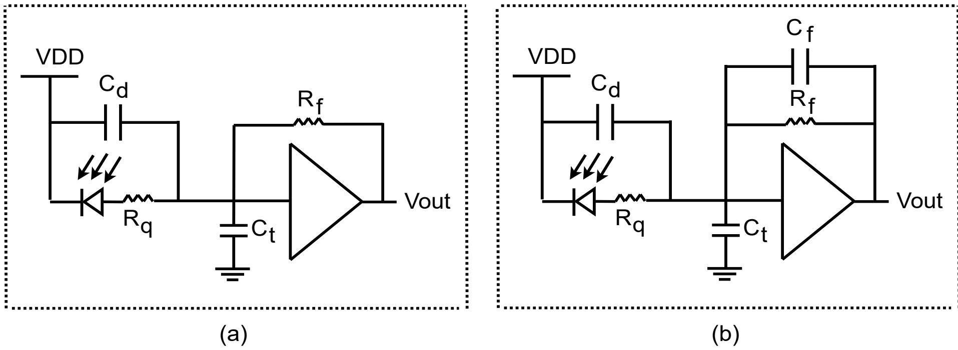


**Figure 3.3:** (a) Shunt-feedback TIA and (b) shunt-feedback TIA with feedback capacitor.

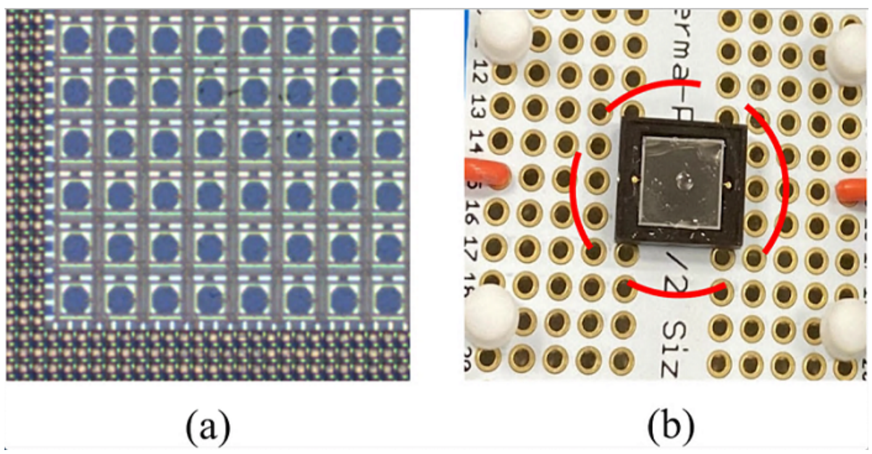


**Figure 3.4:** (a) Custom CMOS SiPM and (b) Hamamatsu SiPM.

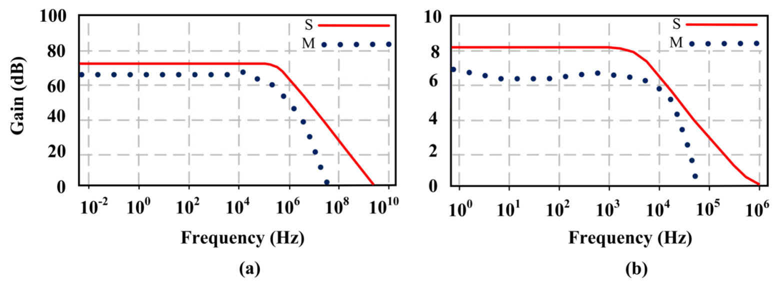


**Figure 3.5:** Simulated and experimental (a) TIA open loop gain and (b) TIA closed loop gain (solid line=simulation, dots=experimental).

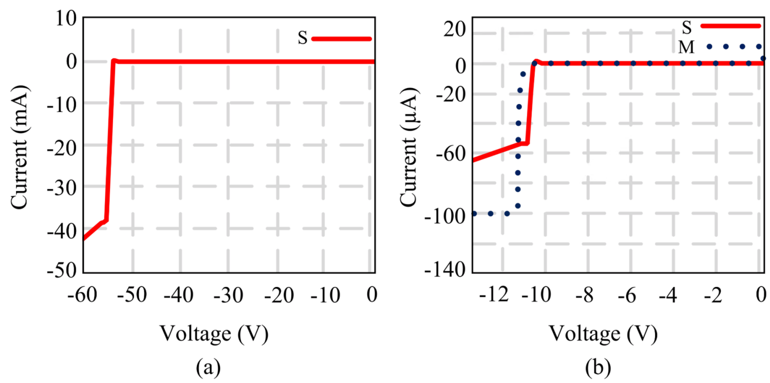


**Figure 3.6:** Single SPAD IV characteristic (a) Hamamatsu simulation (b) Custom CMOS SPAD (solid line=simulation, dots=experimental).

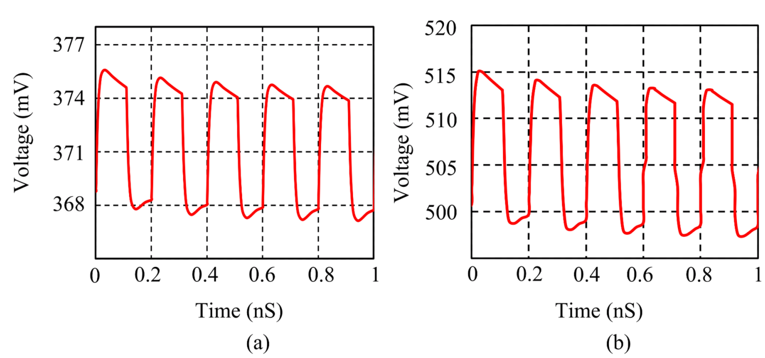


**Figure 3.7:** Simulated output voltage transient response of TIA with (a) CMOS SiPM (3 $\times$ 3 SPAD array) and (b) commercially available SiPM (Hamamatsu S13360).

**Table 3.1:** Comparison table of transimpedance amplifier of this work with other works through literature

| **Reference** | [283] | [69] | [284] | [232] | [110] | [75] | **This work** |
|---|---|---|---|---|---|---|---|
| **Supply (V)** | ±5 | 1.2 | 3 | ±5 | 3.3 | ±13 | 0.8 |
| **Power ($\mu$W)** | 227.5 | 11 | - | 231 | 198 | 7000 | 9 |
| **Area (mm$^2$)** | Dis | 0.72 | Dis | Dis | 9 | Dis | 0.019 |
| **Process** | Dis | 0.13 (*s) | Dis | Dis | 0.35 | Dis | 0.18 |
| **Input Ref Noise (/Hz)** | 0.9 $\mu V^2$ | 0.065 $\mu V^2$ | 0.64 $nV^2$ | 7 $nV^2$ | - | 0.8 $\mu V^2$ | 1.26 $\mu V^2$ |
| **Topology** | TIA | TIA | TIA | TIA | TIA | CA | TIA |
| **Slew Rate** (/ns) | 0.6 mV | 20 mV | 750 $\mu$V | - | 48 V | 1.5 mV | 150 $\mu$V |
| **Gain** | 60 dB | - | - | 65 dB | - | 69 dB | 70 dB |

# Chapter 4

# SiPM Based Sensor For Nuclear Detection Applications

**Portions of this chapter were previously published in:**

- S. Hesari and N. McFarlane., "A SiPM Based Sensor For Nuclear Detection Applications," *IEEE International System-on-Chip Conference,* p. 57-62, 2021.

## 4.1 Nuclear Readout Electronics Requirements

A typical output current pulse of a SiPM is shown in Fig. 4.1. A SiPM's avalanche current depends on the particle flux and the photon yield of a specific scintillator and SiPM characteristics. The maximum current that can be generated with each SiPM is a function of the applied reverse bias voltage, breakdown voltage, and the quenching and parasitic resistances. The rise time and fall time are an RC time constant, where the rise time is a function of the parasitic resistance and the fall time is a function of the quenching resistance. Many SiPMs, such as the Hammatsu-S13360, have a pulse width in the ns range [282]. Thus, a readout circuit with slew rate higher than tens of $\mu$V/ns is suitable for typical SiPM readout circuit.

The noise sources of the detection system include the thermal and flicker noise of the transistors, thermal noise of the resistor, noise of the diodes, and $1/f$ noise of the printed circuit board. For energy measurement, the resolution is mainly affected by large SiPM gain and not the electronic noise [120]. Where intrinsic noise associated with SiPM are SiPM gain fluctuation, dark current, optical crosstalk and afterpulsing [120]. Initially the OTA was only simulated with SiPM models [71]. Here, the two amplifier structures, one a custom transimpedance amplifier designed and fabricated in a 180 nm commerical CMOS process, and the second a discrete commercially available charge amplifier were investigated. The amplifiers were experimentally verified with a source, scintillator, and commerical SiPM and the energy resolution determined. The CMOS amplifier can be easily integrated with a SiPM on the same chip.

## 4.2 Readout Systems

### 4.2.1 Bulk-Driven TIA Based Readout

Fig. 4.2 (a) shows the transimpedance amplifier where, for stability, a feedback capacitor, ($C_f$), is in parallel with feedback resistor ($R_f$). As discussed in previous chapters, this amplifier is based on a bulk driven topology (Fig. 4.2 (b)).

In experimental measurements, as it was shown in previous chapter, the amplifier had an open loop gain of 70 dB (over three chips, 68, 69, and 71dB), slew rate of 150 $\mu$V/ns, and input referred noise of 1.26 $\mu V^2$/Hz. The power of the OTA was 9 $\mu$W.

Generally, if the bulk and source of PMOS are not tied together, the threshold voltage and consequently the drain current changes. For PMOS transistors implemented in a commercial 0.18 $\mu$m CMOS process, increasing the bulk-source voltage from 0 to 300 mV, decreases $V_{TH}$ by 100 mV Fig. 4.3 [285].

This reduction corresponds to less than 20% reduction in drain current and consequently the gain. Moreover, if the $V_{DS}$ is well above the $V_{GS}$-$V_{TH}$, then the effect of the $V_{TH}$ variation on the drain current is significantly decreased.

In addition to regular simulation, Monte Carlo simulation also performed through Cadence to investigate about the output gain and frequency of proposed transimpedance amplifier over process variation. Monte Carlo simulation take the advantage of repeated statistical and random sampling to compute the results. This type of simulation is quite similar to random experiments, where depend on random environmental and non environmental phenomena, the specific results are not known in advance and may not be quite the same. Monte Carlo simulation helps us to test the process variation and mismatching between devices in a single chip or wafer.

Monte Carlo simulations of the amplifier is shown in Fig. 4.4. The results of Monte Carlo simulation with 100 runs, that the majority of open loop gain of proposed structure fall in between 66 and 70 dB.

### 4.2.2 Commercial Discrete Amplifier Based Readout

Fig. 4.5 shows a Cremat CR-113-R2.1 configured as a charge amplifier [75]. CR-113-R2.1, is a 8-pin SIP package charge amplifier module that is used with many radiation detectors such as SiPMs. This is one of the four series of charge amplifier offered by Cremat. The rise time of output pulses of this amplifier is about 1 ns. However rise time is under the effects of amplifier's input capacitance. Where added capacitance at input terminal of amplifier, 9 ns/pF slows the rise time. The other factor that affect the rise time is the SiPM's speed. For example if the duration of generated current pulse from SiPM coupled with scintillator is in the range of $\mu$s, then the rise time of amplifier will be at least equal to duration of generated pulse.

The amplifier's gain is the reciprocal of the feedback capacitance. A 750 pF feedback capacitor provided 1.3 mV/pC closed loop gain.

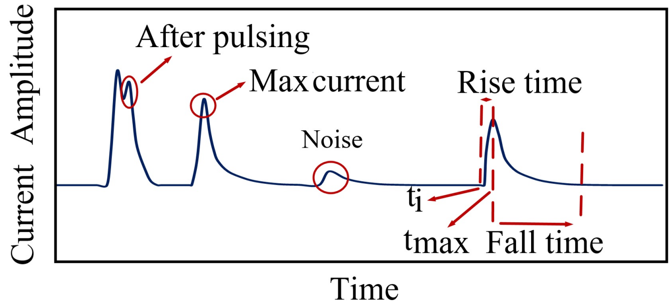


**Figure 4.1:** Example SiPM current pulse showing the various parts of the signal [1].

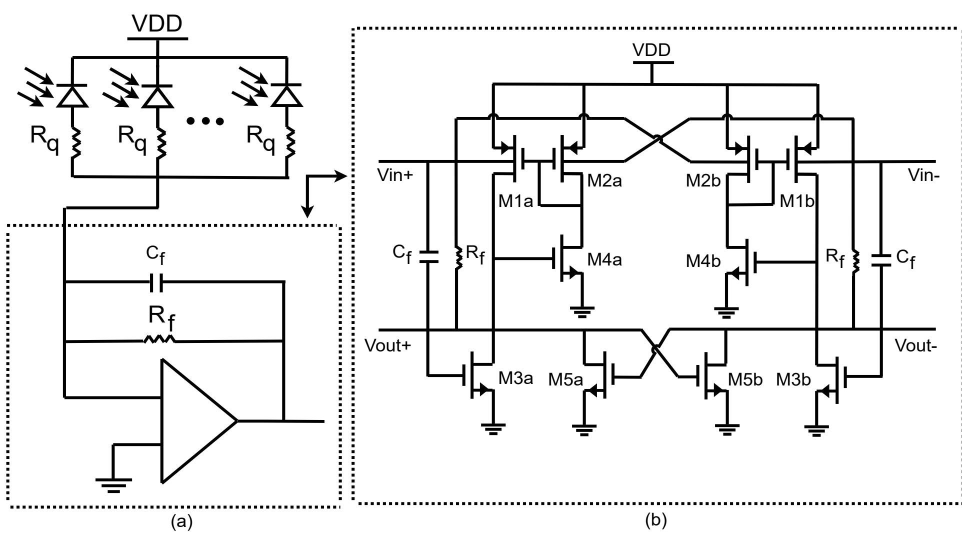


**Figure 4.2:** (a) Transimpedance amplifier coupled with SiPM. (b) Bulk driven TIA schematic used in (a).

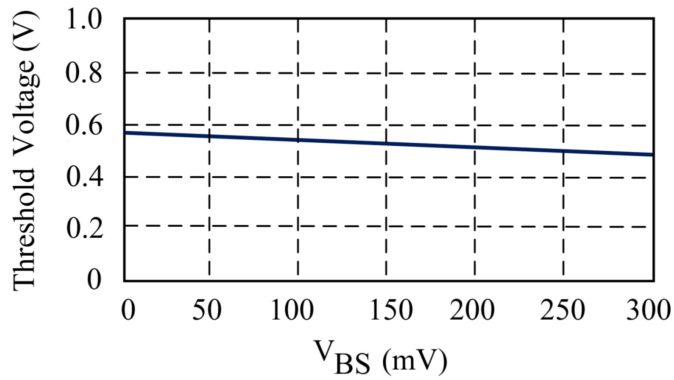


**Figure 4.3:** Typical PMOS threshold voltage variation.

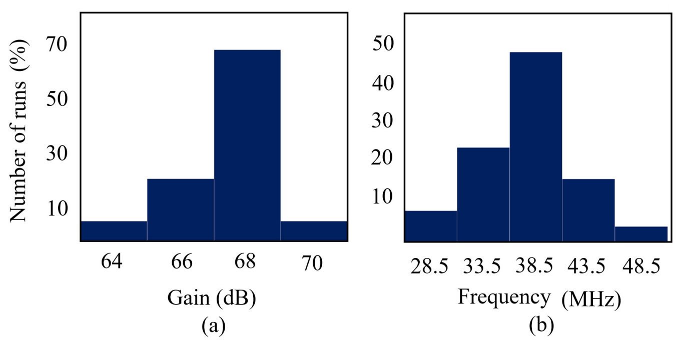


**Figure 4.4:** Monte Carlo simulation of the OTA.

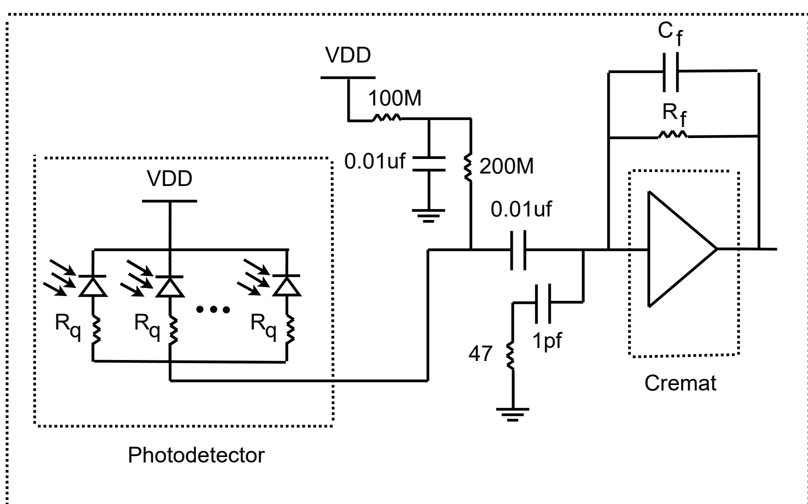


**Figure 4.5:** Commercially available Cremat CR-113-R2.1 amplifier [75].

With the feedback resistor of 68 k$\Omega$, the time constant was 50 $\mu$s [75]. The amplifier had 69 dB open loop gain, slew rate of 1.5 mV/ns and input referred noise of 0.8 $\mu V^2/Hz$.

Simulations of the amplifiers were performed using SPICE models for the SPADs with experimentally derived parameters. The SPICE models consist of switches, resistor, voltage controlled voltage sources and cpacitances [286, 32]. The models can be used to simulate both the DC current-voltage characteristic curve and the transient avalanche quench and noise processes. A Hammamatsu S13360 SiPM with 14,400 microcells and 6 mm $\times$ 6 mm active area was used. The IV characteristic and dynamic simulation showed good agreement with the experimentally measured breakdown values. Both systems were experimentally verified with SiPMs using a pulsed light emitting diode (LED) and a scintillator coupled with a gamma source.

## 4.3 Nuclear Readout Measurements

A commercial LED was used to perform initial characterizations. The LED photon output was characterized as a function of applied voltage and applied frequency. The LED was placed in a light tight box and its intensity verified with an optical power meter (Newport-1936-R). A function generator (Tektronix-AFG3022C) was used to modulate the light intensity and frequency simulating a pulsed light source (Fig. 4.6).
Measurement results of this experiment are shown in Fig. 4.7 (a) and (b).

Implementing the SiPMs in CMOS will allow for lower operating voltages than typical PMTs and commercial SiPMs. The custom CMOS SiPM active area is 2 mm $\times$ 2 mm and the microcells dimensions are 20 $\mu$m. The Hamamatsu S13360 is 6 mm $\times$ 6 mm and with microcells dimensions of 50 $\mu$m. Thus, the output voltage transient response of the TIA with the Hamamatsu SiPM is greater than the CMOS SiPM. The Hamamatsu SiPM was biased using a CAEN power supply at 55V. The excess bias voltage for the Hamamatsu SiPM was 2 V. Fig. 4.8 shows the output of the CMOS and Cremat amplifier (both with the Hamamatsu SiPM) using the pulsed LED at a frequency of 1KHz and an applied voltage varying from 3 to 5 V on the LED.

The Cremat CR113 power supply voltage was ±6 volts while the bulk driven amplifier used a 1.8V power supply rail. This test was performed to determine the relationship between the number of photons and the measured output for calibration purposes.

Fig. 4.9 (a) and (b) show the output of the TIA and Cremat with the Hammatsu SiPM for a fixed light intensity (5 V amplitude applied to the LED) and varying pulse frequency. In these figures, the signals are not pure sine signals due to improper probe compensation.

Both amplifiers were coupled to the Hammatsu SiPM and characterized with a gamma check source. Fig. 4.10 shows the experimental setup where the SiPM was coupled first to the scintillator and gamma source and all were placed inside a light tight box.

The gamma source used was Caesium-137 (CS-137). The scintillator used was a Caesium Hafnium Chloride (CHC) scintillating crystal with dimensions 5 mm $\times$ 5 mm $\times$ 5 $mm^3$ wrapped in Teflon tape. CHC has a generic cubic crystal structure and is a non-hygroscopic compounds with light yield up to 54,000 photons/MeV where 1 MeV is equal to $1.6\times10^{-9}$ J [287]. This is equivalent to $8.64\times10^{-9}$ J when measured by a photodetector [288]. Most of the kinetic energy generated by gamma ray is turned into heat as the electron collides with atoms in the crystal and only about 10 percent of the gamma ray energies emerges as photons. Since CS-137 has energy of 662 keV (from Ba moving to the ground state) [289], the amount of photons generated by CS-137 coupled with CHC scintillator, is approximately 3600 photons.

Fig. 4.11 (a) and (b) show the output transient output voltage of transimpedance amplifier and the Cremat amplifier. In this figure the Hamamatsu SiPM was coupled with a CS137 gamma source. The output was measured multiple times in sequential windows. The majority of spikes are between 0.4 and 0.6V for the bulk driven architecture and 1 to 1.5V for the Creamat amplifier.

Fig. 4.12 (a) and (b) shows the spectrum for the output. For the bulk driven amplifier, the average spike value was 460 mV with a full width half max of 40mV. For the commerical amplifier, the full width half max was 200 mV with an average peak of 1.4V. Therefore, the energy resolution for the commercial amplifier based system with the CHC scintillator was $(200/1400)\times100=14.2\%$ while the energy resolution for the bulk driven amplifier with the

CHC scintillator was $(40/460)\times100=8.6\%$. Table 4.1 compares the readout characteristic and energy resolution of the proposed system with other readout strategies found in literature.

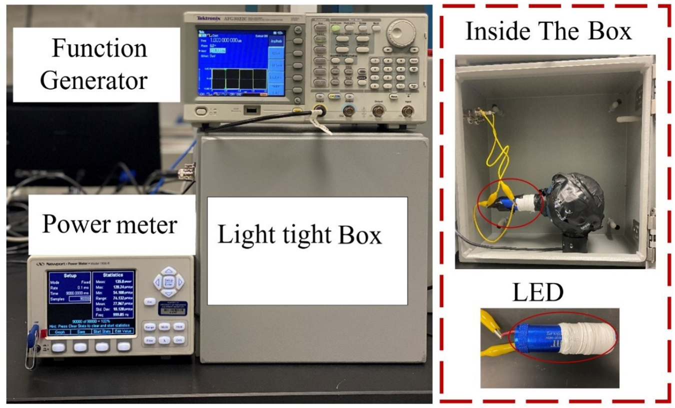


**Figure 4.6:** Experimental setup of light source initial characterizations.

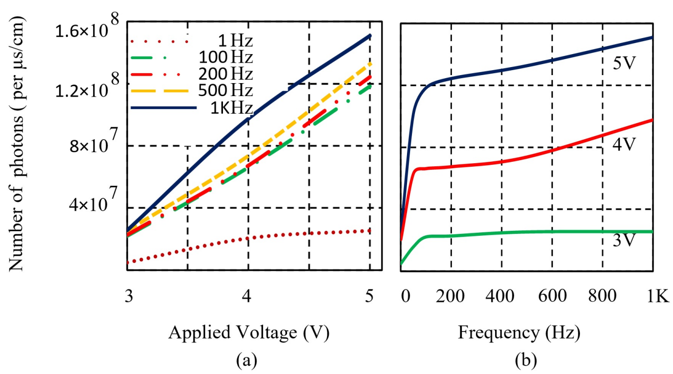


**Figure 4.7:** Experimental measurements of photon flux as a function of (a) frequency and (b) voltage applied to the LED.

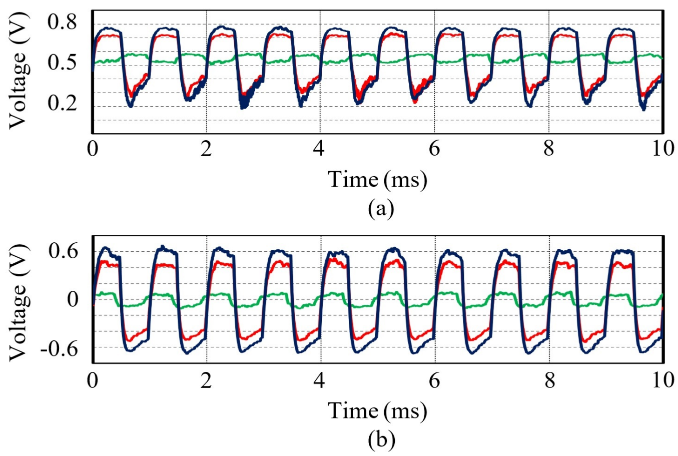


**Figure 4.8:** (a) Output voltage of the TIA and the SiPM for different light intensities and (b) output voltage of the Cremat amplifier and the SiPM for different light intensities. (At 1kHz and 3, 4, and 5 V amplitude applied to LED).

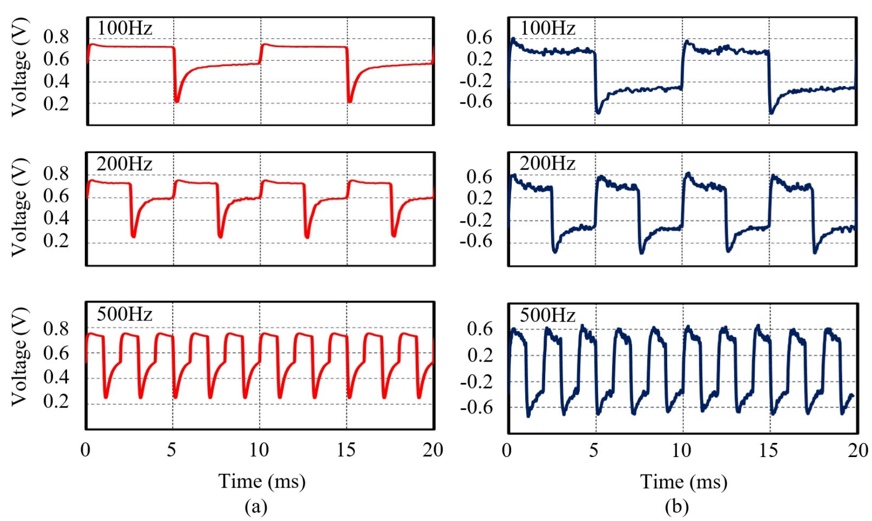


**Figure 4.9:** (a) TIA transient response and (b) Cremat Inc amplifier transient response to the Hamamatsu SiPM coupled with the pulsed LED (5V amplitude applied to LED).

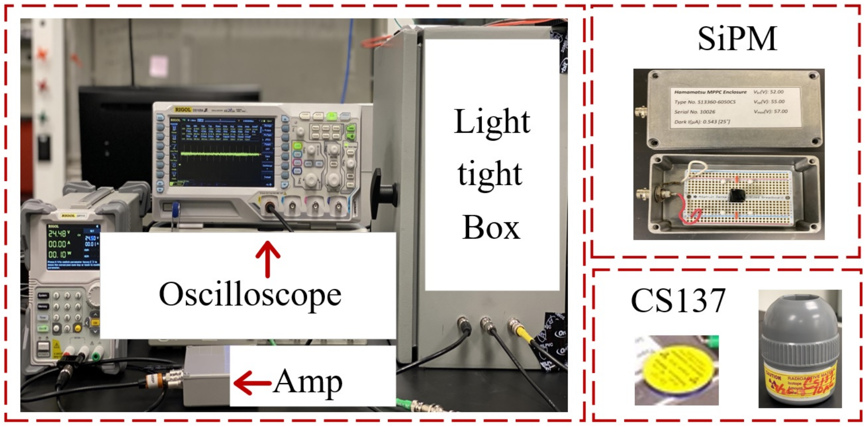


**Figure 4.10:** Experimental setup of the amplifiers with a check source and scintillator coupled to the Hamamatsu SiPM.

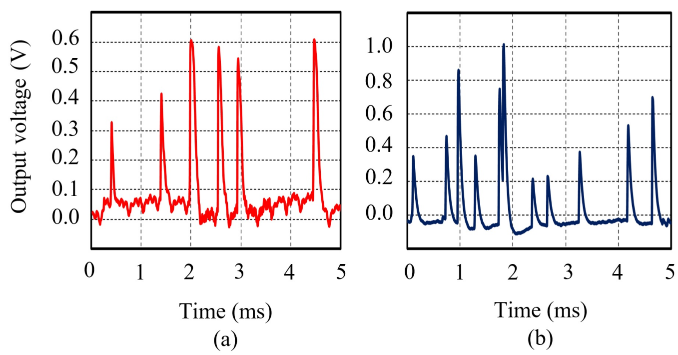


**Figure 4.11:** Experimental response to a CS-137 gamma source and CHC scintillator coupled to a Hammatsu SiPM with (a) the bulk driven TIA and (b) the Cremat CR-113-R2.1 readout electronics.

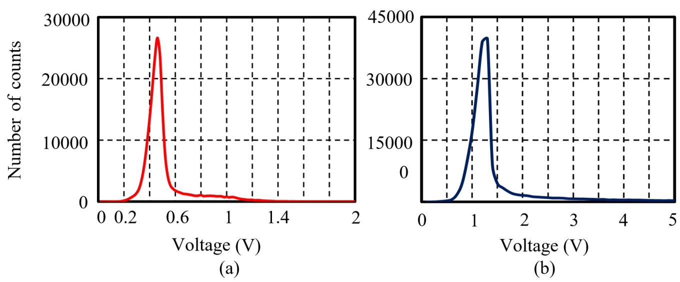


**Figure 4.12:** Experimental spectrum of a CS-137 gamma source and CHC scintillator coupled to a Hammatsu SiPM with (a) the bulk driven TIA and (b) the Cremat CR-113-R2.1.

**Table 4.1:** Energy Resolution of the System Compared with other Readout Systems.

| Reference | SiPM | Scintillator | Source | Readout | Energy Resolution |
|---|---|---|---|---|---|
| [11] | Ketek | LYSO:Ce | Na22 | ASIC (MADPET) | 13.7 (%) |
| [13] | Hamamatsu | LFS | CS137 | ASIC (TOF-PET) | 11.8 (%) |
| [14] | Ketek | LYSO | Na22 | ASIC (TOFPET2) | 10 (%) |
| [16] | SensL | LYSO | Na22 | $\Sigma\Delta$ ADC | 10.5 (%) |
| [24] | Hamamatsu | LYSO | Na22 | $\Sigma\Delta$ | 18.7 (%) |
| [30] | Hamamatsu | LYSO | Na22 | ASIC (TOFPET2) | 13.08 (%) |
| [290] | SensL | CHC | AmBe | Digitizer (Caen V1730C) | 6.27 (%) |
| [291] | Hamamatsu | CHC | CS137 | MCA (Canberra MP2) | 4.5 (%) |
| **This work (Cremat)** | Hamamatsu | CHC | CS137 | CSP (CR113) | 14.2 (%) |
| **This work (Cremat)** | Hamamatsu | CHC | CS137 | TIA (CMOS 180nm) | 8.6 (%) |

# Chapter 5

# Conclusion

In this work a SiPM based nuclear detection system was developed using a custom OTA developed in standard CMOS in transimpedance configuration and a separate SiPM and scintillator. While the SiPM operates at a relatively high reverse bias voltages, for a portable detector the TIA should operate at low voltages and should be compact so as to reduce the size of the system. Therefore, in this work bulk-driven and subthreshold region operating transistors were used to develop the OTA for the TIA. The amplifier is fully differential to help compensate for variations from SiPM to SiPM by using a reference device.

The transimpedance amplifier was designed and fabricated in a commercial 180 nm CMOS and used cross coupled loads in addition to body driving. The OTA and a discrete amplifier setup were experimentally characterized with a Hamamatsu SiPM. The CMOS based OTA has an open loop gain of 70 dB, slew rate of 150 $\mu$V/ns, and input referred noise of 1.26 $\mu V^2/Hz$.

The transimpedance amplifier has 7.1 dB closed loop gain and the closed loop gain can be improved by adjusting the feedback network. The amplifier is fully differential allowing for the difference between a detecting SiPM and a reference device to account for process variations.

The commercial amplifier has 69 dB open loop gain, slew rate of 1.5 mV/ns and input referred noise of $0.8 \mu V^2/Hz$. The CMOS amplifier consumes much less power (9 $\mu$W) than the commercial amplifier. The systems were characterized with a pulsed LED and a gamma source with scintillator.

The energy resolution for the commercial amplifier based system with a CHC scintillator was 14.2% while the energy resolution for the bulk driven amplifier was 8.6%. Initial experimental results indicate that the proposed systems are suitable for portable CMOS based nuclear detectors and the amplifier can be integrated with on-chip SiPMs for miniaturization, compactness, and reduced power. By integrating the SiPM with the OTA on the same chip this work enable a future path for portable SiPM based detectors.

# Bibliography


[1] S. H. Hesari and N. McFarlane, "A SiPM based sensor for nuclear detection applications," in *IEEE International System-on-Chip Conference*. IEEE, 2021, pp. 57–62. ix, xi, 2, 3, 67

[2] S. Hatefi Hesari, M. A. Haque, and N. McFarlane, "A comprehensive survey of readout strategies for SiPMs used in nuclear imaging systems," in *Photonics*, vol. 8, no. 7. Multidisciplinary Digital Publishing Institute, 2021, p. 266. ix, 2, 3

[3] M. D. Rolo, R. Bugalho, F. Gonçalves, A. Rivetti, G. Mazza, J. C. Silva, R. Silva, and J. Varela, "A 64-channel ASIC for TOFPET applications," in *IEEE Nuclear Science Symposium and Medical Imaging Conference*. IEEE, 2012, pp. 1460–1464. ix, 12

[4] M. Rolo, R. Bugalho, F. Goncalves, G. Mazza, A. Rivetti, J. Silva, R. Silva, and J. Varela, "TofPet ASIC for PET applications," *Journal of Instrumentation*, vol. 8, no. 02, p. C02050, 2013. ix, 12

[5] I. Sacco, P. Fischer, and M. Ritzert, "PETA4: a multi-channel TDC/ADC ASIC for SiPM readout," *Journal of Instrumentation*, vol. 8, no. 12, p. C12013, 2013. ix, x, 12, 33

[6] J. Fleury, S. Callier, C. de La Taille, N. Seguin, D. Thienpont, F. Dulucq, S. Ahmad, and G. Martin, "Petiroc, a new front-end ASIC for time of flight application," in *IEEE Nuclear Science Symposium and Medical Imaging Conference*. IEEE, 2013, pp. 1–5. ix, x, 2, 12, 33

[7] H. Chen, K. Briggl, P. Fischer, A. Gil, T. Harion, Y. Munwes, M. Ritzert, D. Schimansky, H.-C. Schultz-Coulon, W. Shen *et al.*, "A dedicated readout ASIC for time-of-flight positron emission tomography using silicon photomultiplier (SiPM)," in *IEEE Nuclear Science Symposium and Medical Imaging Conference*. IEEE, 2014, pp. 1–5. ix, x, 12, 33

[8] S. Ahmad, J. Fleury, C. de la Taille, N. Seguin-Moreau, F. Dulucq, G. Martin-Chassard, S. Callier, D. Thienpont, and L. Raux, "Triroc: A multi-channel SiPM read-out ASIC for PET/PET-ToF application," *IEEE Transactions on Nuclear Science*, vol. 62, no. 3, pp. 664–668, 2015. ix, 12

[9] R. Becker, C. Casella, S. Corrodi, G. Dissertori, J. Fischer, A. Howard, M. Ito, and W. Lustermann, "Studies of the high rate coincidence timing response of the STiC and TOFPET ASICs for the SAFIR PET scanner," *Journal of Instrumentation*, vol. 11, no. 12, pp. P12 001–P12 001, dec 2016. [Online]. Available: https://doi.org/10.1088/1748-0221/11/12/p12001 ix, 12

[10] G. Sportelli, S. Ahmad, N. Belcari, M. G. Bisogni, N. Camarlinghi, A. Di Pasquale, S. Dussoni, J. Fleury, M. Morrocchi, E. Zaccaro, and A. Del Guerra, "The trimage pet data acquisition system: Initial results," *IEEE Transactions on Radiation and Plasma Medical Sciences*, vol. 1, no. 2, pp. 168–177, 2017. ix, x, 12, 33

[11] N. Omidvari, J. Cabello, G. Topping, F. R. Schneider, S. Paul, M. Schwaiger, and S. I. Ziegler, "PET performance evaluation of MADPET4: a small animal PET insert for a 7 T MRI scanner," *Physics in Medicine & Biology*, vol. 62, no. 22, p. 8671, 2017. ix, x, 12, 33, 75

[12] P. Trigilio, P. Busca, R. Quaglia, M. Occhipinti, and C. Fiorini, "A SiPM-readout ASIC for SPECT applications," *IEEE Transactions on Radiation and Plasma Medical Sciences*, vol. 2, no. 5, pp. 404–410, 2018. ix, 12

[13] A. L. Goertzen and D. Van Elburg, "Performance characterization of MPCC modules for TOF-PET applications," *IEEE Transactions on Radiation and Plasma Medical Sciences*, vol. 3, no. 4, pp. 475–482, 2018. ix, x, 2, 12, 33, 75

[14] D. Schug, V. Nadig, B. Weissler, P. Gebhardt, and V. Schulz, "Initial measurements with the PETsys TOFPET2 ASIC evaluation kit and a characterization of the ASIC TDC," *IEEE Transactions on Radiation and Plasma Medical Sciences*, vol. 3, no. 4, pp. 444–453, 2018. ix, x, 12, 33, 75

[15] M. Carminati, G. L. Montagnani, M. Occhipinti, A. Kuehne, T. Niendorf, K. Nagy, A. Nagy, M. Czeller, and C. Fiorini, "SPECT/MRI INSERT compatibility: Assessment, solutions, and design guidelines," *IEEE Transactions on Radiation and Plasma Medical Sciences*, vol. 2, no. 4, pp. 369–379, 2018. ix, 12

[16] Z. Zhao, S. Xie, X. Zhang, J. Yang, Q. Huang, J. Xu, and Q. Peng, "An advanced 100-channel readout system for nuclear imaging," *IEEE Transactions on Instrumentation and Measurement*, vol. 68, no. 9, pp. 3200–3210, 2018. ix, 2, 12, 75

[17] M. Carminati, F. Baratelli, M. Occhipinti, K. Erlandsson, K. Nagy, Z. Nyitrai, M. Czeller, A. Kühne, T. Niendorf, S. Valtorta *et al.*, "Validation and performance assessment of a preclinical SiPM-based SPECT/MRI insert," *IEEE Transactions on Radiation and Plasma Medical Sciences*, vol. 3, no. 4, pp. 483–490, 2019. ix, 12

[18] L. Buonanno, G. Montagnani, D. Di Vita, F. Castelli, M. Carminati, and C. Fiorini, "GAMMA: a high dynamic range 16-ch ASIC for large scintillators readout with SiPM array," in *IEEE Nuclear Science Symposium and Medical Imaging Conference*. IEEE, 2019, pp. 1–3. ix, 12

[19] G. Montagnani, L. Buonanno, D. Di Vita, M. Carminati, F. Camera, A. Gola, V. Regazzoni, and C. Fiorini, "Spectroscopic performance of a sr co-doped 3" LaBr3 scintillator read by a SiPM array," *Nuclear Instruments and Methods in Physics Research Section A: Accelerators, Spectrometers, Detectors and Associated Equipment*, vol. 931, pp. 158–161, 2019. ix, 12, 32

[20] D. Di Vita, L. Buonanno, G. Montagnani, A. Minerva, A. Giannoni, M. Carminati, F. Camera, and C. Fiorini, "A high dynamic range 144-SiPM detection module for gamma spectroscopy and imaging with 3" LaBr 3," in *IEEE Nuclear Science Symposium and Medical Imaging Conference*. IEEE, 2019, pp. 1–3. ix, 12

[21] G. L. Montagnani, L. Buonanno, D. Di Vita, C. Fiorini, and M. Carminati, "A compact 4-decade dynamic range readout module for gamma spectroscopy and imaging," in *IEEE International Symposium on Circuits and Systems*. IEEE, 2019, pp. 1–5. ix, 12

[22] M. Carminati, I. D'Adda, A. Morahan, K. Erlandsson, K. Nagy, M. Czeller, B. Tölgyesi, Z. Nyitrai, A. Savi, P. van Mullekom *et al.*, "Clinical SiPM-based MRI-compatible SPECT: Preliminary characterization," *IEEE Transactions on Radiation and Plasma Medical Sciences*, vol. 4, no. 3, pp. 371–377, 2019. ix, 12

[23] X. Yue, C. Liu, and Z. Deng, "An energy-resolved photon-counting readout electronics for scintillator based on pole-zero compensation and tot method," in *IEEE Nuclear Science Symposium and Medical Imaging Conference*. IEEE, 2019, pp. 1–3. ix, 12

[24] X. Cheng, K. Hu, and Y. Shao, "Dual-polarity SiPM readout electronics based on 1-bit sigma-delta modulation circuit for PET detector applications," *IEEE Transactions on Nuclear Science*, vol. 66, no. 9, pp. 2107–2113, 2019. ix, 2, 12, 75

[25] A. LaBella, P. Vaska, W. Zhao, and A. H. Goldan, "Convolutional neural network for crystal identification and gamma ray localization in PET," *IEEE Transactions on Radiation and Plasma Medical Sciences*, vol. 4, no. 4, pp. 461–469, 2020. ix, 12

[26] J. Barrio, N. Cucarella, A. J. Gonzalez, M. Freire, V. Ilisie, and J. M. Benlloch, "Characterization of a high-aspect ratio detector with lateral sides readout for compton PET," *IEEE Transactions on Radiation and Plasma Medical Sciences*, vol. 4, no. 5, pp. 546–554, 2020. ix, 2, 12

[27] N. Kratochwil, E. Auffray, and S. Gundacker, "Exploring cherenkov emission of bgo for TOF-PET," *IEEE Transactions on Radiation and Plasma Medical Sciences*, pp. 1–1, 2020. ix, 12

[28] D. Sánchez, S. Gómez, J. M. Fernández-Tenllado, R. Ballabriga, M. Campbell, and D. Gascón, "Multimodal simulation of large area silicon photomultipliers for time resolution optimization," *Nuclear Instruments and Methods in Physics Research Section A: Accelerators, Spectrometers, Detectors and Associated Equipment*, vol. 1001, p. 165247, 2021. ix, 12

[29] J. Boo, M. D. Hammig, and M. Jeong, "Row–column readout method to mitigate radiographic-image blurring from multipixel events in a coded-aperture imaging

system," *IEEE Transactions on Nuclear Science*, vol. 68, no. 5, pp. 1175–1183, 2021. ix, 12

[30] V. Nadig, D. Schug, B. Weissler, and V. Schulz, "Evaluation of the PETsys TOFPET2 ASIC in multi-channel coincidence experiments," *EJNMMI physics*, vol. 8, no. 1, pp. 1–21, 2021. ix, x, 2, 12, 33, 75

[31] F. Licciulli and C. Marzocca, "Parameter extraction method for the electrical model of a silicon photomultiplier," *IEEE Transactions on Nuclear Science*, vol. 63, no. 5, pp. 2517–2526, 2016. ix, 6, 12

[32] F. Zappa, A. Tosi, A. Dalla Mora, and S. Tisa, "SPICE modeling of single photon avalanche diodes," *Sensors and Actuators A: Physical*, vol. vol. 153, no. 2, pp. 197–204, 2009. ix, 9, 10, 13, 69

[33] M. Nakhostin, *Signal processing for radiation detectors.* John Wiley & Sons, 2017. ix, x, 13, 16, 17, 18, 19, 22, 23, 24, 25, 26, 27, 34, 35, 36, 37, 46

[34] Z. Wu, Y. Xu, and Z. Ma, "A time-to-amplitude converter with high impedance switch topology for single-photon time-of-flight measurement," *IEEE Access*, vol. 9, pp. 16 672–16 678, 2021. x, 21, 24

[35] F. Powolny, E. Auffray, S. Brunner, E. Garutti, M. Goettlich, H. Hillemanns, P. Jarron, P. Lecoq, T. Meyer, H. Schultz-Coulon *et al.*, "Time-based readout of a silicon photomultiplier (SiPM) for time of flight positron emission tomography (TOF-PET)," *IEEE Transactions on Nuclear Science*, vol. 58, no. 3, pp. 597–604, 2011. x, 20, 24, 38

[36] E. Ermis and C. Celiktas, "Time resolution investigations for general purpose plastic scintillation detectors in different thicknesses," *Journal of Radioanalytical and Nuclear Chemistry*, vol. 295, no. 1, pp. 523–536, 2013. x, 21, 24

[37] M. S. Lee, J. W. Cates, M. Kapusta, M. Schmand, and C. S. Levin, "Study of lutetium-based scintillators for PET system design with 100-ps coincidence time resolution," in *IEEE Nuclear Science Symposium and Medical Imaging Conference.* IEEE, 2019, pp. 1–2. x, 2, 33

[38] J. Du, X. Bai, and S. R. Cherry, "A depth-encoding PET detector for high resolution PET using 1 mm SiPMs," *Physics in Medicine & Biology*, vol. 65, no. 16, p. 165011, 2020. x, 25, 33

[39] G. Gramegna, P. O'connor, P. Rehak, and S. Hart, "CMOS preamplifier for low-capacitance detectors," *Nuclear Instruments and Methods in Physics Research Section A: Accelerators, Spectrometers, Detectors and Associated Equipment*, vol. 390, no. 1-2, pp. 241–250, 1997. x, 26, 29, 34, 36

[40] Y. Liu, J. Zhang, L. Liu, S. Li, and R. Zhou, "Implementation of real-time digital CR–RCm shaping filter on FPGA for gamma-ray spectroscopy," *Nuclear Instruments and Methods in Physics Research Section A: Accelerators, Spectrometers, Detectors and Associated Equipment*, vol. 906, pp. 1–9, 2018. x, 20, 27, 28, 35

[41] A. Silva-Juárez, E. Tlelo-Cuautle, L. G. De La Fraga, and R. Li, "FPAA-based implementation of fractional-order chaotic oscillators using first-order active filter blocks," *Journal of advanced research*, vol. 25, pp. 77–85, 2020. x, 27, 35

[42] A. Rivetti, *CMOS: front-end electronics for radiation sensors.* CRC press, 2018. x, 29, 36

[43] V. Rasmussen, "Nuclear electronics: by PW nicholson. 388 pages, diagrams, 6× 9 in. john wiley, new york, 1974. price, $24.95.(approx.£ 12.50)." 1976. x, 29, 36

[44] M. Kruiskamp and D. Leenaerts, "A CMOS peak detect sample and hold circuit," *IEEE Transactions on Nuclear Science*, vol. vol. 41, no. 1, pp. 295–298, 1994. x, 29, 37

[45] A. Argentieri, F. Corsi, M. Foresta, C. Marzocca, and A. Del Guerra, "Design and characterization of CMOS multichannel front-end electronics for silicon photomultipliers," *Nuclear Instruments and Methods in Physics Research Section A: Accelerators, Spectrometers, Detectors and Associated Equipment*, vol. 652, no. 1, pp. 516–519, 2011. x, 38, 40, 41, 43, 44

[46] F. Corsi, M. Foresta, C. Marzocca, G. Matarrese, and A. Del Guerra, "Current-mode front-end electronics for silicon photo-multiplier detectors," in *International Workshop on Advances in Sensors and Interface*, 2007, pp. 1–6. x, 38, 43, 44

[47] M. Wang, Y. Wang, Q. Cao, L. Wang, J. Kuang, and Y. Xiao, "Comparison of three pre-amplifier circuits for time readout of SiPM in TOF-PET detectors," in *International Symposium on Circuits and Systems* , 2019, pp. 1–5. x, 31, 44

[48] V. Lakshmy and E. Shajahan, "Performance analysis of low power low voltage amplifier designs in 45nm CMOS technology by incorporating miller compensation," in *IEEE Recent Advances in Intelligent Computational Systems*. IEEE, 2020, pp. 18–22. x, 44

[49] L. H. Rodovalho, "Schmitt trigger based single-ended voltage amplifier with positive feedback control for ultra-low-voltage supplies," in *IEEE Nordic Circuits and Systems Conference*. IEEE, 2020, pp. 1–6. x, 44

[50] N. Dinu, P. Barrillon, C. Bazin, N. Belcari, M. G. Bisogni, S. Bondil-Blin, M. Boscardin, V. Chaumat, G. Collazuol, C. De La Taille *et al.*, "Characteristics of a prototype matrix of silicon photomultipliers (SiPM)," *Journal of Instrumentation*, vol. 4, no. 03, p. P03016, 2009. x, 44

[51] W. Zhang, B. Zheng, P. Goodwill, and S. Conolly, "A custom low-noise preamplifier for magnetic particle imaging," in *International Workshop on Magnetic Particle Imaging*. IEEE, 2015, pp. 1–1. x, 44

[52] K. Achtenberg, J. Mikołajczyk, and Z. Bielecki, "FET input voltage amplifier for low frequency noise measurements," *Metrology and Measurement Systems*, pp. 531–540, 2020. x, 44

[53] F. Corsi, M. Foresta, C. Marzocca, G. Matarrese, and A. Del Guerra, "ASIC development for SiPM readout," *Journal of Instrumentation*, vol. 4, no. 03, p. P03004, 2009. x, 38, 43, 44

[54] I. Yadav and H. Shrimali, "Noise and crosstalk models of the particle detector with zero-pole transformation charge sensitive amplifier," *Nuclear Instruments and Methods*

*in Physics Research Section A: Accelerators, Spectrometers, Detectors and Associated Equipment*, vol. 937, pp. 107–116, 2019. x, 45

[55] C. Lee, G. Cho, T. Unruh, S. Hur, and I. Kwon, "Integrated circuit design for radiation-hardened charge-sensitive amplifier survived up to 2 mrad," *Sensors*, vol. 20, no. 10, p. 2765, 2020. x, 40, 45

[56] I. Yadav, A. Joshi, E. Ruscino, V. Liberali, A. Andreazza, and H. Shrimali, "Design of a charge sensitive amplifier for silicon particle detector in BCD 180 nm process," in *International Conference on VLSI Design and International Conference on Embedded Systems*. IEEE, 2019, pp. 541–542. x, 45

[57] M. Beikahmadi and S. Mirabbasi, "A low-power low-noise CMOS charge-sensitive amplifier for capacitive detectors," in *IEEE International New Circuits and systems conference*. IEEE, 2011, pp. 450–453. x, 45

[58] Y. Song, J. Rozsa, J. Magalhaes, S. Smith, B. Karlinsey, W. Kinnison, E. Gustafson, D. Austin, A. R. Hawkins, and S.-h. W. Chiang, "Design of common-mode feedback for high-gain charge amplifier," in *Intermountain Engineering, Technology and Computing Conference*. IEEE, 2020, pp. 1–5. x, 31, 39, 45

[59] Z. Gu and X. Bi, "A charge amplifier with noise peaking suppression and gain drop compensation utilizing a quasi-miller rc network," *AEU-International Journal of Electronics and Communications*, vol. 107, pp. 252–256, 2019. x, 45

[60] I. Kwon, T. Kang, B. T. Wells, J. Lawrence, and M. D. Hammig, "Compensation of the detector capacitance presented to charge-sensitive preamplifiers using the miller effect," *Nuclear Instruments and Methods in Physics Research Section A: Accelerators, Spectrometers, Detectors and Associated Equipment*, vol. 784, pp. 220–225, 2015. x, 45

[61] G. Ambrosi, M. Ambrosio, C. Aramo, E. Bissaldi, A. Boiano, C. Bonavolontà, C. de Lisio, L. Di Venere, E. Fiandrini, N. Giglietto *et al.*, "Development of a charge preamplifier to improve nuv-hd SiPM performances," *Nuclear and Particle Physics Proceedings*, vol. 291, pp. 40–43, 2017. x, 38, 42, 43, 46, 48

[62] J. Kaspar, A. Fienberg, D. Hertzog, M. Huehn, P. Kammel, K. Khaw, D. Peterson, M. Smith, T. Van Wechel, A. Chapelain *et al.*, "Design and performance of SiPM-based readout of PbF2 crystals for high-rate, precision timing applications," *Journal of Instrumentation*, vol. 12, no. 01, p. P01009, 2017. xi, 31, 41, 47, 48, 50

[63] V. Stornelli, L. Pantoli, G. Barile, A. Leoni, and E. D'Amico, "Silicon photomultiplier sensor interface based on a discrete second generation voltage conveyor," *Sensors*, vol. 20, no. 7, p. 2042, 2020. xi, 41, 47, 48, 50

[64] V. K. Pandey and C. M. Tan, "Application of gallium nitride technology in particle therapy imaging," *IEEE Transactions on Nuclear Science*, 2021. xi, 50

[65] S. Giannakopoulos, Z. S. He, I. Darwazeh, and H. Zirath, "Differential common base TIA with 56 dB Ohm gain and 45 GHz bandwidth in 130 nm SiGe," in *IEEE Asia Pacific Microwave Conference*. IEEE, 2017, pp. 1107–1110. xi, 50

[66] M. Seung, W. Choi, S. Hur, and I. Kwon, "Design of a transimpedance amplifier for a radiation detector to observe a nuclear reactor under severe accidents," *Simulation*, vol. 2, p. 3, 2019. xi, 47, 50

[67] I. Kwon, T. Kang, B. T. Wells, J. Lawrence, and M. D. Hammig, "A high-gain 1.75-GHz dual-inductor transimpedance amplifier with gate noise suppression for fast radiation detection," *IEEE Transactions on Circuits and Systems II: Express Briefs*, vol. 63, no. 4, pp. 356–360, 2015. xi, 47, 48, 50

[68] S. Kodam, A. Arashanapalli, J. Kolla, and G. Dheeraj, "Design and implementation of CMOS transimpedance amplifier as a photodetector," *Materials Today: Proceedings*, 2021. xi, 50

[69] M. de Medeiros Silva and L. B. Oliveira, "Regulated common-gate transimpedance amplifier designed to operate with a silicon photo-multiplier at the input," *IEEE Transactions on Circuits and Systems I: Regular Papers*, vol. 61, no. 3, pp. 725–735, 2013. xi, 41, 48, 50, 63

[70] L. B. Oliveira, C. M. Leitão, and M. M. Silva, "Noise performance of a regulated cascode transimpedance amplifier for radiation detectors," *IEEE Transactions on Circuits and Systems I: Regular Papers*, vol. 59, no. 9, pp. 1841–1848, 2012. xi, 50, 57

[71] S. H. Hesari, A. Hedayatipour, M. A. Haque, and N. McFarlane, "A bulk driven transimpedance amplifier for portable SiPM based detectors," in *IEEE Sensors Conference*. IEEE, 2020, pp. 1–4. xi, 2, 50, 65

[72] B. Razavi, "The cross-coupled pair - part i [a circuit for all seasons]," *IEEE Solid-State Circuits Magazine*, vol. 6, no. 3, pp. 7–10, 2014. xi, 49, 51

[73] M. Bazes, "Two novel fully complementary self-biased CMOS differential amplifiers," *IEEE Journal of Solid-State Circuits*, vol. 26, no. 2, pp. 165–168, 1991. xi, 49, 51

[74] T. Kulej, "0.5-V bulk-driven CMOS operational amplifier," *IET Circuits, Devices & Systems*, vol. 7, no. 6, pp. 352–360, 2013. xi, 53, 54, 55

[75] "Cremat (CR-113-R2.1)," Available online: https://www.cremat.com/CR-113-R2.1.pdf, (Accessed on 05/26/2021). xi, 17, 63, 66, 68, 69

[76] C. Alispach, J. Borkowski, F. R. Cadoux, N. De Angelis, D. Della Volpe, Y. Favre, M. Heller, J. Juryšek, E. Lyard, D. Mandat *et al.*, "Large scale characterization and calibration strategy of a SiPM-based camera for gamma-ray astronomy," *Journal of Instrumentation*, vol. 15, no. 11, p. P11010, 2020. 1

[77] F. Henningsen, M. Boehmer, A. Gärtner, L. Geilen, R. Gernhäuser, H. Heggen, K. Holzapfel, C. Fruck, L. Papp, I. Rea *et al.*, "A self-monitoring precision calibration light source for large-volume neutrino telescopes," *Journal of Instrumentation*, vol. 15, no. 07, p. P07031, 2020. 1

[78] Y. Sun and J. Maricic, "SiPMs characterization and selection for the dune far detector photon detection system," *Journal of Instrumentation*, vol. 11, no. 01, p. pp. C01078, 2016. 1

[79] M. P. Unterweger, M. Cox, and J. Santulli, "American national standard performance requirements for spectroscopic personal radiation detectors (SPRDs) for homeland security," *ANSI N42.48-2018 (Revision of ANSI N42.48-2008)*, pp. 1–39, 2019. 1

[80] L. Pibida, M. Mille, and B. Norman, "Recommendations for improving consistency in the radiation fields used during testing of radiation detection instruments for homeland security applications," *Journal of research of the National Institute of Standards and Technology*, vol. 118, p. 292, 2013. 1

[81] T. Huang, Q. Fu, C. Yuan, and S. Lin, "A gamma and neutron phoswich read out with SiPM for SPRD," *Nuclear Instruments and Methods in Physics Research Section A: Accelerators, Spectrometers, Detectors and Associated Equipment*, vol. 881, pp. 48–52, 2018. 1

[82] G. Romanchek, Y. Wang, H. Marupudi, and S. Abbaszadeh, "Performance of optical coupling materials in scintillation detectors post temperature exposure," *Sensors*, vol. 20, no. 21, p. 6092, 2020. 1

[83] S. Dey, E. Myers, T. K. Lewellen, R. S. Miyaoka, and J. C. Rudell, "A row-column summing readout architecture for SiPM based PET imaging systems," in *IEEE Nuclear Science Symposium and Medical Imaging Conference*. IEEE, 2013, pp. 1–5. 4

[84] J. W. Cates, M. F. Bieniosek, and C. S. Levin, "Highly multiplexed signal readout for a time-of-flight positron emission tomography detector based on silicon photomultipliers," *Journal of Medical Imaging*, vol. 4, no. 1, p. 011012, 2017. 4

[85] H. Kim, C.-M. Kao, Y. Hua, Q. Xie, and C.-T. Chen, "Multiplexing readout for time-of-flight (TOF) PET detectors using striplines," *IEEE Transactions on Radiation and Plasma Medical Sciences*, 2021. 4

[86] Q. Yang, Z. Kuang, Z. Sang, Y. Yang, and J. Du, "Performance comparison of two signal multiplexing readouts for SiPM-based PET detector," *Physics in Medicine & Biology*, vol. 64, no. 23, p. 23NT02, 2019. 4

[87] M.-A. Tétrault, E. D. Lamy, A. Boisvert, C. Thibaudeau, M. Kanoun, F. Dubois, R. Fontaine, and J.-F. Pratte, "Real-time discrete SPAD array readout architecture for time of flight PET," *IEEE Transactions on Nuclear Science*, vol. 62, no. 3, pp. 1077–1082, 2015. 4

[88] M. Jeong and M. Hammig, "Development of hand-held coded-aperture gamma ray imaging system based on GAGG (Ce) scintillator coupled with SiPM array," *Nuclear Engineering and Technology*, vol. 52, no. 11, pp. 2572–2580, 2020. 4

[89] K. Shimazoe, M. Yoshino, Y. Ohshima, M. Uenomachi, K. Oogane, T. Orita, H. Takahashi, K. Kamada, A. Yoshikawa, and M. Takahashi, "Development of simultaneous PET and compton imaging using GAGG-SiPM based pixel detectors," *Nuclear Instruments and Methods in Physics Research Section A: Accelerators, Spectrometers, Detectors and Associated Equipment*, vol. 954, p. 161499, 2020. 4

[90] Z. Liang, T. Hu, X. Li, Y. Wu, C. Li, and Z. Tang, "A cosmic ray imaging system based on plastic scintillator detector with SiPM readout," *Journal of Instrumentation*, vol. 15, no. 07, p. C07033, 2020. 4

[91] G. Maira, A. M. Chiarelli, S. Brafa, S. Libertino, G. Fallica, A. Merla, and S. Lombardo, "Imaging system based on silicon photomultipliers and light emitting diodes for functional near-infrared spectroscopy," *Applied Sciences*, vol. 10, no. 3, p. 1068, 2020. 4

[92] V. J. Kitsmiller and T. D. O'Sullivan, "Next-generation frequency domain diffuse optical imaging systems using silicon photomultipliers," *Optics letters*, vol. 44, no. 3, pp. 562–565, 2019. 4

[93] M. Heller, E. jr Schioppa, A. Porcelli, I. T. Pujadas, K. Zietara, D. Della Volpe, T. Montaruli, F. Cadoux, Y. Favre, J. Aguilar *et al.*, "An innovative silicon photomultiplier digitizing camera for gamma-ray astronomy," *The European Physical Journal C*, vol. 77, no. 1, pp. 1–31, 2017. 4

[94] J. Zhang, R. Zhou, S. Zhang, H. Xiong, G. Hu, Y. Li, Z. Liu, and C. Yang, “Data acquisition and trigger system for imaging atmospheric cherenkov telescopes of the LHAASO,” *Journal of Instrumentation*, vol. 15, no. 02, p. T02004, 2020. 4

[95] H. Xiong, R. Zhou, J. Chen, Y. Li, C. Yang, B. Bi, J. Zhang, J. Zhang, X. Cao, S. Zhang *et al.*, “Design and performance of analog circuit for the wide field of view cherenkov telescope array of lhaaso,” *Nuclear Instruments and Methods in Physics Research Section A: Accelerators, Spectrometers, Detectors and Associated Equipment*, vol. 925, pp. 156–163, 2019. 4

[96] A. Berti, A. Chiavassa, D. Corti, D. Depaoli, F. Di Pierro, L. Lessio, M. Mallamaci, M. Mariotti, C. Perennes, R. Rando *et al.*, “Development and test of a SiPM cluster for a SiPM version of the cherenkov telescope array lst camera,” *Nuclear Instruments and Methods in Physics Research Section A: Accelerators, Spectrometers, Detectors and Associated Equipment*, vol. 982, p. 164373, 2020. 4

[97] J. Boo, M. D. Hammig, and M. Jeong, “Row–column readout method to mitigate radiographic-image blurring from multipixel events in a coded-aperture imaging system,” *IEEE Transactions on Nuclear Science*, vol. 68, no. 5, pp. 1175–1183, 2021. 4

[98] S. Jiang, J. Lu, S. Meng, F. Ye, J. Ning, Q. Yi, J. Yang, R. Yang, and X. Yan, “A prototype of SiPM-based scintillator compton camera with capacitive multiplexing readout,” *Journal of Instrumentation*, vol. 16, no. 01, p. P01027, 2021. 4, 16, 28

[99] S. Aldawood, P. Thirolf, A. Miani, M. B ohmer, G. Dedes, R. Gernh auser, C. Lang, S. Liprandi, L. Maier, T. Marinšek *et al.*, “Development of a compton camera for prompt-gamma medical imaging,” *Radiation Physics and Chemistry*, vol. 140, pp. 190–197, 2017. 4

[100] Y. Nakamura, K. Shimazoe, H. Takahashi, S. Yoshimura, Y. Seto, S. Kato, M. Takahashi, and T. Momose, “Development of a novel handheld intra-operative laparoscopic compton camera for 18f-fluoro-2-deoxy-2-d-glucose-guided surgery,” *Physics in Medicine & Biology*, vol. 61, no. 15, p. 5837, 2016. 4

[101] H. Lee, T. Lee, and W. Lee, "Development of a position-sensitive $4\pi$ compton camera based on a single segmented scintillator," *IEEE Transactions on Nuclear Science*, vol. 67, no. 12, pp. 2511–2522, 2020. 4

[102] G. Cozzi, P. Busca, M. Carminati, C. Fiorini, A. Gola, C. Piemonte, and V. Regazzoni, "Development of a SiPM-based detection module for prompt gamma imaging in proton therapy," in *IEEE Nuclear Science Symposium, Medical Imaging Conference and Room-Temperature Semiconductor Detector Workshop*, 2016, pp. 1–5. 4

[103] M. G. Giacomelli, "Evaluation of silicon photomultipliers for multiphoton and laser scanning microscopy," *Journal of biomedical optics*, vol. 24, no. 10, p. 106503, 2019. 4, 41

[104] C. Martin, T. Li, E. Hegarty, P. Zhao, S. Mondal, and A. Ben-Yakar, "Line excitation array detection fluorescence microscopy at 0.8 million frames per second," *Nature Communications*, vol. 9, no. 1, pp. 1–10, 2018. 4

[105] P. Dorosz, M. Baszczyk, and W. Kucewicz, "The study of single cells in a system based on silicon photomultipliers," in *IEEE Nuclear Science Symposium and Medical Imaging Conference*, 2018, pp. 1–2. 4

[106] E. Martinenghi, L. Di Sieno, D. Contini, M. Sanzaro, A. Pifferi, and A. Dalla Mora, "Time-resolved single-photon detection module based on silicon photomultiplier: A novel building block for time-correlated measurement systems," *Review of Scientific Instruments*, vol. 87, no. 7, p. 073101, 2016. 4

[107] B. Li, Q. Miao, S. Wang, D. Hui, T. Zhao, K. Liang, R. Yang, and D. Han, "Time-correlated photon counting (tcpc) technique based on a photon-number-resolving photodetector," in *Advanced Photon Counting Techniques X*, vol. 9858, 2016, p. 98580L. 4

[108] G. Acconcia, A. Cominelli, M. Ghioni, and I. Rech, "Fast fully-integrated front-end circuit to overcome pile-up limits in time-correlated single photon counting with single photon avalanche diodes," *Optics express*, vol. 26, no. 12, pp. 15 398–15 410, 2018. 4

[109] J. Du, X. Bai, A. Gola, F. Acerbi, A. Ferri, C. Piemonte, Y. Yang, and S. R. Cherry, “Performance of a high-resolution depth-encoding PET detector module using linearly-graded SiPM arrays,” *Physics in Medicine & Biology*, vol. 63, no. 3, p. 035035, 2018. 4

[110] A. Muntean, A. Sachdeva, E. Venialgo, S. Gnecchi, D. Palubiak, C. Jackson, and E. Charbon, “A fully integrated state-of-the-art analog sipm with on-chip time conversion,” in *IEEE Nuclear Science Symposium and Medical Imaging Conference*, 2018, pp. 1–3. 5, 6, 63

[111] R. J. Walker, E. A. Webster, J. Li, N. Massari, and R. K. Henderson, “High fill factor digital silicon photomultiplier structures in 130nm CMOS imaging technology,” in *IEEE Nuclear Science Symposium and Medical Imaging Conference* , 2012, pp. 1945–1948. 5

[112] G. Paternoster, L. Ferrario, F. Acerbi, A. G. Gola, and P. Bellutti, “Silicon photomultipliers technology at fondazione bruno kessler and 3d integration perspectives,” in *European Solid-State Device Research Conference* , 2019, pp. 50–53. 5

[113] E. Vilella, O. Alonso, and A. Dieguez, “3d integration of geiger-mode avalanche photodiodes aimed to very high fill-factor pixels for future linear colliders,” *Nuclear Instruments and Methods in Physics Research Section A: Accelerators, Spectrometers, Detectors and Associated Equipment*, vol. 731, pp. 103–108, 2013. 5

[114] J. M. Brown, “In-silico optimisation of tileable philips digital SiPM based thin monolithic scintillator detectors for SPECT applications,” *Applied Radiation and Isotopes*, vol. 168, p. 109368, 2021. 5, 17

[115] Y. Zou, F. Villa, D. Bronzi, S. Tisa, A. Tosi, and F. Zappa, “Fully CMOS analog and digital SiPMs,” in *Optical Components and Materials XII*, vol. vol. 9359, 2015, p. 93591B. 6, 10, 11

[116] A. Muntean, E. Venialgo, S. Gnecchi, C. Jackson, and E. Charbon, "Towards a fully digital state-of-the-art analog SiPM," in *IEEE Nuclear Science Symposium and Medical Imaging Conference*, 2017, pp. 1–4. 6

[117] A. Muntean, E. Venialgo, A. Ardelean, A. Sachdeva, E. Ripiccini, D. Palubiak, C. Jackson, and E. Charbon, "Blumino: the first fully integrated analog SiPM with on-chip time conversion," *IEEE Transactions on Radiation and Plasma Medical Sciences*, 2020. 6

[118] F. Corsi, A. Dragone, C. Marzocca, A. Del Guerra, P. Delizia, N. Dinu, C. Piemonte, M. Boscardin, and G. F. Dalla Betta, "Modelling a silicon photomultiplier (SiPM) as a signal source for optimum front-end design," *Nuclear Instruments and Methods in Physics Research Section A: Accelerators, Spectrometers, Detectors and Associated Equipment*, vol. 572, no. 1, pp. 416–418, 2007. 6

[119] D. Marano, M. Belluso, G. Bonanno, S. Billotta, A. Grillo, S. Garozzo, G. Romeo, O. Catalano, G. La Rosa, G. Sottile *et al.*, "Silicon photomultipliers electrical model extensive analytical analysis," *IEEE Transactions on Nuclear Science*, vol. 61, no. 1, pp. 23–34, 2013. 6

[120] P. P. Calò, F. Ciciriello, S. Petrignani, and C. Marzocca, "SiPM readout electronics," *Nuclear Instruments and Methods in Physics Research Section A: Accelerators, Spectrometers, Detectors and Associated Equipment*, vol. 926, pp. 57–68, 2019. 8, 60, 65

[121] D. Bronzi, S. Tisa, F. Villa, S. Bellisai, A. Tosi, and F. Zappa, "Fast sensing and quenching of CMOS SPADs for minimal afterpulsing effects," *IEEE Photonics Technology Letters*, vol. vol. 25, no. 8, pp. 776–779, 2013. 11

[122] C. Xu, E. Garutti, S. Mandai, and E. Charbon, "Comparison of digital and analog silicon photomultiplier for positron emission tomography application," in *IEEE Nuclear Science Symposium and Medical Imaging Conference*, 2013, pp. 1–7. 11

[123] "WB series silicon photomultipliers (SiPM) - Ketek Gmbh," Available online: https://www.ketek.net/sipm/sipm-modules/tia-modules/, (Accessed on 02/04/2021). 11

[124] "PETsys SiPM readout system," Available online: https://www.petsyselectronics.com/web/public/products/6, (Accessed on 04/02/2021). 11

[125] "A1702 - 32-channel SiPM readout front-end board - CAEN - tools for discovery," Available online: https://www.caen.it/products/a1702/, (Accessed on 04/02/2021). 11

[126] "PhotoniQ multi-channel data acquisition systems," Available online: https://vertilon.com/pdf/UM6177.pdf, (Accessed on 04/02/2021). 11

[127] T. SensL, "Readout methods for arrays of silicon photomultipliers. technical note," 2014. 11

[128] A. Selfridge, S. Cherry, and R. Badawi, "Characterization of four readout circuits for an MR compatible, preclinical PET detector," *Physics in Medicine & Biology*, vol. 65, no. 12, p. 125008, 2020. 11

[129] C. Mihai, G. Pascovici, G. Ciocan, C. Costache, V. Karayonchev, A. Lungu, N. Mărginean, R. Mihai, C. Neacşu, J.-M. Régis *et al.*, "Development of large area silicon photomultipliers arrays for $\gamma$-ray spectroscopy applications," *Nuclear Instruments and Methods in Physics Research Section A: Accelerators, Spectrometers, Detectors and Associated Equipment*, vol. 953, p. 163263, 2020. 11, 38

[130] H. Poladyan, O. Bubon, A. Teymurazyan, S. Senchurov, and A. Reznik, "Gaussian position-weighted center of gravity algorithm for multiplexed readout," *Physics in Medicine & Biology*, vol. 65, no. 16, p. 165003, 2020. 11

[131] E. Roncali and S. R. Cherry, "Application of silicon photomultipliers to positron emission tomography," *Annals of biomedical engineering*, vol. 39, no. 4, pp. 1358–1377, 2011. 14

[132] R. Gómez-Reino Garrido, "The distributed control system of lhc-cms: study of the stability and dynamic range of the new sipm detector for the hcal," 2014. 16

[133] M. Carminati, I. D'Adda, A. J. Morahan, K. Erlandsson, K. Nagy, M. Czeller, B. Tölgyesi, Z. Nyitrai, A. Savi, P. van Mullekom, B. F. Hutton, and C. Fiorini, "Clinical sipm-based mri-compatible spect: Preliminary characterization," *IEEE Transactions on Radiation and Plasma Medical Sciences*, vol. 4, no. 3, pp. 371–377, 2020. 16

[134] B. Kim, K. Lee, J. Lee, S. Hwang, D. Heo, and K. Han, "Design of optimal digital filter and digital signal processing for a CdZnTe high resolution gamma-ray system," *Applied Radiation and Isotopes*, vol. 162, p. 109171, 2020. 16

[135] M. Sammartini, M. Gandola, F. Mele, B. Garavelli, D. Macera, P. Pozzi, and G. Bertuccio, "X-ray spectroscopy with a CdTe pixel detector and sirio preamplifier at deep submicrosecond signal-processing time," *IEEE Transactions on Nuclear Science*, vol. 68, no. 1, pp. 70–75, 2020. 16

[136] M. Lee, D. Lee, E. Ko, K. Park, J. Kim, K. Ko, M. Sharma, and G. Cho, "Pulse pileup correction method for gamma-ray spectroscopy in high radiation fields," *Nuclear Engineering and Technology*, vol. 52, no. 5, pp. 1029–1035, 2020. 16

[137] P. Adrich and I. Zychor, "Least-squares fitting algorithm for peak pile-up correction in gamma-ray spectroscopy," *Nuclear Instruments and Methods in Physics Research Section A: Accelerators, Spectrometers, Detectors and Associated Equipment*, p. 164962, 2020. 16

[138] M. Pocaterra and M. Ciappa, "Experimental setup to monitor non-destructive single events triggered by ionizing radiation in power devices," *Microelectronics Reliability*, vol. 114, p. 113755, 2020. 16

[139] J. W. Cates, S. Gundacker, E. Auffray, P. Lecoq, and C. S. Levin, "Improved single photon time resolution for analog SiPMs with front end readout that reduces influence

of electronic noise," *Physics in Medicine & Biology*, vol. 63, no. 18, p. 185022, 2018. 17, 20

[140] P. Lecoq and S. Gundacker, "SiPM applications in positron emission tomography: toward ultimate PET time-of-flight resolution," *The European Physical Journal Plus*, vol. 136, no. 3, pp. 1–16, 2021. 17

[141] S. Surti and J. S. Karp, "Update on latest advances in time-of-flight PET," *Physica Medica*, vol. 80, pp. 251–258, 2020. 17

[142] H. Wieczorek, A. Thon, T. Dey, V. Khanin, and P. Rodnyi, "Analytical model of coincidence resolving time in TOF-PET," *Physics in Medicine & Biology*, vol. 61, no. 12, p. 4699, 2016. 17

[143] M. Crotti, I. Rech, and M. Ghioni, "Four channel, 40 ps resolution, fully integrated time-to-amplitude converter for time-resolved photon counting," *IEEE Journal of Solid-State Circuits*, vol. 47, no. 3, pp. 699–708, 2012. 18

[144] N. D'Ascenzo, E. Antonecchia, M. Gao, X. Zhang, G. Baumgartner, A. Brensing, Z. Li, Q. Liu, G. Rose, X. Shi *et al.*, "Evaluation of a digital brain positron emission tomography scanner based on the plug&imaging sensor technology," *IEEE Transactions on Radiation and Plasma Medical Sciences*, vol. 4, no. 3, pp. 327–334, 2019. 18

[145] M. A. Nelson, B. D. Rooney, D. R. Dinwiddie, and G. S. Brunson, "Analysis of digital timing methods with baf2 scintillators," *Nuclear Instruments and Methods in Physics Research Section A: Accelerators, Spectrometers, Detectors and Associated Equipment*, vol. 505, no. 1-2, pp. 324–327, 2003. 19

[146] Y. Kawada, A. Yunoki, T. Yamada, and Y. Hino, "Effect of time walk in the use of single channel analyzer/discriminator for saturated pulses in the $4\pi\beta$–$\gamma$ coincidence experiments," *Applied Radiation and Isotopes*, vol. 109, pp. 369–373, 2016. 19

[147] V. Bespal'ko, I. Burak, and K. Salmins, "Estimating the precision of a leading-edge discriminator with amplitude correction," *Instruments and Experimental Techniques*, vol. 62, no. 6, pp. 788–793, 2019. 19, 21

[148] L.-Q. Li and L. M. Davis, "Single photon avalanche diode for single molecule detection," *Review of Scientific Instruments*, vol. 64, no. 6, pp. 1524–1529, 1993. 19

[149] M. Bertolaccini and S. Cova, "A fast single channel pulse height analyzer for precision timing with scintillation counters," *IEEE Transactions on Nuclear Science*, vol. 19, no. 3, pp. 423–430, 1972. 19

[150] H. Lima, G. Guedes, A. Barbosa, and J. Seixas, "A fast multichannel analyzer for radiation detection applications," *IEEE Transactions on Instrumentation and Measurement*, vol. 53, no. 2, pp. 378–383, 2004. 20

[151] B. Swann, B. Blalock, L. Clonts, D. Binkley, J. Rochelle, E. Breeding, and K. Baldwin, "A 100-ps time-resolution cmos time-to-digital converter for positron emission tomography imaging applications," *IEEE Journal of Solid-State Circuits*, vol. 39, no. 11, pp. 1839–1852, 2004. 20

[152] L. Martinazzoli, N. Kratochwil, S. Gundacker, and E. Auffray, "Scintillation properties and timing performance of state-of-the-art gd3al2ga3o12 single crystals," *Nuclear Instruments and Methods in Physics Research Section A: Accelerators, Spectrometers, Detectors and Associated Equipment*, vol. 1000, p. 165231, 2021. 20

[153] A. Rivetti, M. Alexeev, R. Bugalho, F. Cossio, M. D. R. Rolo, A. Di Francesco, M. Greco, W. Cheng, M. Maggiora, S. Marcello *et al.*, "TIGER: A front-end ASIC for timing and energy measurements with radiation detectors," *Nuclear Instruments and Methods in Physics Research Section A: Accelerators, Spectrometers, Detectors and Associated Equipment*, vol. 924, pp. 181–186, 2019. 20

[154] D. Impiombato, A. Segreto, O. Catalano, S. Giarrusso, and T. Mineo, "Use of the peak-detector mode for gain calibration of SiPM sensors with ASIC CITIROC read-out," *Journal of Instrumentation*, vol. 15, no. 04, p. C04007, 2020. 20

[155] M. Parsakordasiabi, I. Vornicu, Á. Rodríguez-Vázquez, and R. Carmona-Galán, "A low-resources TDC for multi-channel direct tof readout based on a 28-nm FPGA," *Sensors*, vol. 21, no. 1, p. 308, 2021. 20

[156] A. Lobanov, "Precision timing calorimetry with the cms hgcal," *Journal of Instrumentation*, vol. 15, no. 07, p. C07003, 2020. 20

[157] A. T. Susanto, P. Prajitno, S. K. Wijaya, S. Soekirno, and I. P. Susila, "A systematic literature reviews of multichannel analyzer based on FPGA for gamma spectroscopy," in *Journal of Physics: Conference Series*, vol. 1528, 2020, p. 012016. 20

[158] J. A. Schmitz, M. K. Gharzai, S. Balkir, M. W. Hoffman, and M. Bauer, "A low-power 10-bit multichannel analyzer chip for radiation detection," in *International Symposium on Circuits and Systems*, 2017, pp. 1–4. 20

[159] Z.-j. Qin, C. Chen, J.-s. Luo, X.-h. Xie, L.-q. Ge, and Q.-f. Wu, "A pulse-shape discrimination method for improving gamma-ray spectrometry based on a new digital shaping filter," *Radiation Physics and Chemistry*, vol. 145, pp. 193–201, 2018. 20

[160] C. Sundberg, M. U. Persson, M. Sjölin, J. J. Wikner, and M. Danielsson, "Silicon photon-counting detector for full-field ct using an ASIC with adjustable shaping time," *Journal of Medical Imaging*, vol. 7, no. 5, p. 053503, 2020. 20

[161] R. R. Jogdand, P. Dakhole, and P. Palsodkar, "Low power flash ADC using multiplexer based encoder," in *International Conference on Innovations in Information, Embedded and Communication Systems* , 2017, pp. 1–5. 20

[162] V. K. Pandey, C. M. Tan, and S. Sharma, "Design of GaN based comparator circuit for radiation detectors," in *India Council International Conference* , 2020, pp. 1–6. 20

[163] L. Qiu, K. Wang, K. Tang, L. Siek, and Y. Zheng, "A 10-bit 300 MS/s 5.8 mW SAR ADC with two-stage interpolation for PET imaging," *IEEE Sensors Journal*, vol. 18, no. 5, pp. 2006–2014, 2018. 20

[164] S. Gundacker, F. Acerbi, E. Auffray, A. Ferri, A. Gola, M. Nemallapudi, G. Paternoster, C. Piemonte, and P. Lecoq, "State of the art timing in TOF-PET detectors with luag, GAGG and L(Y)SO scintillators of various sizes coupled to FBK-SiPMs," *Journal of Instrumentation*, vol. 11, no. 08, p. P08008, 2016. 20, 21

[165] S. Gundacker, R. Turtos, E. Auffray, and P. Lecoq, "Precise rise and decay time measurements of inorganic scintillators by means of x-ray and 511 keV excitation," *Nuclear Instruments and Methods in Physics Research Section A: Accelerators, Spectrometers, Detectors and Associated Equipment*, vol. 891, pp. 42–52, 2018. 20

[166] M. Nemallapudi, S. Gundacker, P. Lecoq, and E. Auffray, "Single photon time resolution of state of the art SiPMs," *Journal of Instrumentation*, vol. 11, no. 10, p. P10016, 2016. 21

[167] J. Zhang, M. I. Knopp, and M. V. Knopp, "Sparse detector configuration in SiPM digital photon counting PET: a feasibility study," *Molecular Imaging and Biology*, vol. 21, no. 3, pp. 447–453, 2019. 21

[168] P. Cattaneo, M. De Gerone, F. Gatti, M. Nishimura, W. Ootani, M. Rossella, S. Shirabe, and Y. Uchiyama, "Time resolution of time-of-flight detector based on multiple scintillation counters readout by SiPMs," *Nuclear Instruments and Methods in Physics Research Section A: Accelerators, Spectrometers, Detectors and Associated Equipment*, vol. 828, pp. 191–200, 2016. 21

[169] G. Akamatsu, S. Takyu, E. Yoshida, Y. Iwao, H. Tashima, F. Nishikido, and T. Yamaya, "Evaluation of a hamamatsu TOF-PET detector module with 3.2 mm pitch lfs scintillators and a 256-channel SiPM array," *IEEE Transactions on Radiation and Plasma Medical Sciences*, 2020. 21

[170] M. Sadik, X. Ai, Y. Lu, and R. Nock, "Real-time time correlated photon counters for photon number resolving detectors," in *Optical Sensing and Detection VI*, vol. 11354, 2020, p. 1135406. 21

[171] D. R. Schaart, "Physics and technology of time-of-flight PET detectors," *Physics in Medicine & Biology*, 2021. 21

[172] C.-M. Du, J.-D. Chen, X.-L. Zhang, H.-B. Yang, K. Cheng, J. Kong, Z.-G. Hu, Z.-Y. Sun, H. Su, and H.-S. Xu, "Study of time resolution by digital methods with a DRS4 module," *Chinese Physics C*, vol. 40, no. 4, p. 046101, 2016. 21

[173] T. Xu, J. Wen, Q. Wang, Q. Wei, T. Ma, Y. Liu, and Y. Tai, "A novel sub-millimeter resolution PET detector with TOF capability," in *Nuclear Science Symposium and Medical Imaging Conference*, 2013, pp. 1–5. 21

[174] H. Zhang, X. Wang, L. Zhang, and Z. Zhang, "A 10-bit 120-MS/s SAR ADC in 90nm CMOS with redundancy compensation," in *Proceeedings of the MTT-S International Wireless Symposium* , 2018, pp. 1–3. 21

[175] S. Xie, X. Zhang, Q. Huang, Z. Gong, J. Xu, and Q. Peng, "Methods to compensate the time walk errors in timing measurements for PET detectors," *IEEE Transactions on Radiation and Plasma Medical Sciences*, vol. 4, no. 5, pp. 555–562, 2020. 21

[176] A. Oberstedt, A. Gatera, A. Göök, and S. Oberstedt, "Time response and its impact on prompt fission $\gamma$-ray spectra characteristics," *The European Physical Journal A*, vol. 56, no. 7, pp. 1–8, 2020. 21

[177] H. Wang, Q. Zhao, H. Liang, B. Gu, J. Liu, H. Zhang, and B. Ye, "A new SiPM-based positron annihilation lifetime spectrometer using LYSO and LFS-3 scintillators," *Nuclear Instruments and Methods in Physics Research Section A: Accelerators, Spectrometers, Detectors and Associated Equipment*, vol. 960, p. 163662, 2020. 21

[178] S. Krishnan, C. Webster, A. Duffy, G. Brooks, R. Clay, and J. Mould, "Improving the energy resolution while mitigating the effects of dark-noise, for a microcontroller based SiPM sensor," *Journal of Instrumentation*, vol. 15, no. 09, p. P09028, 2020. 21, 28

[179] P. Calò, S. Petrignani, C. Marzocca, B. Markovic, and A. Dragone, "A CMOS front-end for timing and charge readout of silicon photomultipliers," in *Proceedgins of the Nuclear Science Symposium and Medical Imaging Conference*, 2019, pp. 1–5. 21

[180] J. Yang, Y. Li, Y. Tian, Y. Fu, L. Xu, Y. Cai, and Y. Li, “Performance optimization of pixelated CdZnTe detector readout by analog ASIC using cathode waveform,” *Journal of Instrumentation*, vol. 15, no. 04, p. P04005, 2020. 21

[181] Q. Yang, X. Wang, Z. Kuang, C. Zhang, Y. Yang, and J. Du, “Evaluation of two SiPM arrays for depth-encoding PET detectors based on dual-ended readout,” *IEEE Transactions on Radiation and Plasma Medical Sciences*, 2020. 21

[182] S. Saxena and A. I. Hawari, “Digital pulse deconvolution with adaptive shaping for real-time high-resolution high-throughput gamma spectroscopy,” *Nuclear Instruments and Methods in Physics Research Section A: Accelerators, Spectrometers, Detectors and Associated Equipment*, vol. 954, p. 161288, 2020, symposium on Radiation Measurements and Applications XVII. 21

[183] N. G. Abdallah, M. Rashdan, and A. A. Khalaf, “High resolution time-to-digital converter for PET imaging,” in *International Conference on Innovative Trends in Communication and Computer Engineering* , 2020, pp. 295–298. 21

[184] H. Chen and D. D.-U. Li, “Multichannel, low nonlinearity time-to-digital converters based on 20 and 28 nm FPGAs,” *IEEE Transactions on Industrial Electronics*, vol. 66, no. 4, pp. 3265–3274, 2018. 21

[185] S. Gundacker, E. Auffray, P. Jarron, T. Meyer, and P. Lecoq, “On the comparison of analog and digital SiPM readout in terms of expected timing performance,” *Nuclear Instruments and Methods in Physics Research Section A: Accelerators, Spectrometers, Detectors and Associated Equipment*, vol. 787, pp. 6–11, 2015. 25

[186] A. Brogna, F. D’Andria, C. Marzocca, X. Selmani, and Q. Weitzel, “Time-performance design and study of ultra-wideband amplifiers for SiPM,” *Journal of Instrumentation*, vol. 15, no. 02, p. C02015, 2020. 25

[187] P. Lecoq, C. Morel, J. O. Prior, D. Visvikis, S. Gundacker, E. Auffray, P. Križan, R. M. Turtos, D. Thers, E. Charbon *et al.*, “Roadmap toward the 10 ps time-of-flight PET challenge,” *Physics in Medicine & Biology*, vol. 65, no. 21, p. 21RM01, 2020. 25

[188] S. M. Decker, M. Pizzichemi, A. Polesel, M. Paganoni, E. Auffray, and S. Gundacker, "The digital-analog SiPM approach: a story of electronic and excess noise," in *IEEE Nuclear Science Symposium and Medical Imaging Conference*, 2019, pp. 1–5. 25

[189] H. G. Kang, T. Yamaya, Y. B. Han, S. H. Song, G. B. Ko, J. S. Lee, and S. J. Hong, "Crystal surface and reflector optimization for the SiPM-based dual-ended readout TOF-doi PET detector," *Biomedical Physics & Engineering Express*, vol. 6, no. 6, p. 065028, 2020. 25

[190] A. Berkovich, T. Datta-Chaudhuri, and P. Abshire, "A scalable 20× 20 fully asynchronous SPAD-based imaging sensor with AER readout," in *International Symposium on Circuits and Systems* , 2015, pp. 1110–1113. 25

[191] J. Lin and A. G. Andreou, "A 32× 32 single photon avalanche diode imager with delay-insensitive address-event readout," in *International Symposium of Circuits and Systems* , 2011, pp. 1824–1827. 25

[192] M. S. Ara Shawkat and N. McFarlane, "A CMOS perimeter gated SPAD based digital silicon photomultiplier with asynchronous AER readout for PET applications," in *IEEE Biomedical Circuits and Systems Conference* , 2018, pp. 1–4. 25

[193] M. S. A. Shawkat and N. Mcfarlane, "A digital CMOS silicon photomultiplier using perimeter gated single photon avalanche diodes with asynchronous AER readout," *IEEE Transactions on Circuits and Systems I: Regular Papers*, vol. 67, no. 12, pp. 4818–4828, 2020. 25

[194] J. A. Leñero-Bardallo, R. Carmona-Galán, and A. Rodríguez-Vázquez, "Applications of event-based image sensors—review and analysis," *International Journal of Circuit Theory and Applications*, vol. 46, no. 9, pp. 1620–1630, 2018. 25

[195] J. A. Lenero-Bardallo, F. Pérez-Pena, R. Carmona-Galán, and Á. Rodríguez-Vázquez, "Pipeline AER arbitration with event aging," in *International Symposium on Circuits and Systems* , 2017, pp. 1–4. 25

[196] G. L. Montagnani, "Development of a 3" labr3 sipm-based detection module for high resolution gamma ray spectroscopy and imaging," in *Special Topics in Information Technology.* Springer, Cham, 2021, pp. 77–82. 26

[197] Y. Tomita, Y. Shirayanagi, S. Matsui, M. Misawa, H. Takahashi, T. Aoki, and Y. Hatanaka, "X-ray color scanner with multiple energy differentiate capability," in *IEEE Symposium Conference Record Nuclear Science 2004.*, vol. 6, 2004, pp. 3733–3737 Vol. 6. 26

[198] A. Torralba, C. Lujan-Martinez, R. G. Carvajal, J. Galan, M. Pennisi, J. Ramirez-Angulo, and A. Lopez-Martin, "Tunable linear mos resistors using quasi-floating-gate techniques," *IEEE Transactions on Circuits and Systems II: Express Briefs*, vol. 56, no. 1, pp. 41–45, 2009. 26

[199] C. Arnaboldi and G. Pessina, "A very simple baseline restorer for nuclear applications," *Nuclear Instruments and Methods in Physics Research Section A: Accelerators, Spectrometers, Detectors and Associated Equipment*, vol. 512, no. 1-2, pp. 129–135, 2003. 26

[200] G. Panjkovic, "Alternative circuit topologies for charge preamplifiers and pulse shapers," in *2013 IEEE Nuclear Science Symposium and Medical Imaging Conference (2013 NSS/MIC)*, 2013, pp. 1–6. 27

[201] H. Wu, H. Xu, Q. Zhang, X. Meng, R. Di, and Y. Liu, "Implementation of a straight-line shaper on an FPGA for a UAVAGS," *Journal of Instrumentation*, vol. 15, no. 10, p. T10011, 2020. 28

[202] M. Y. Kantor and A. Sidorov, "Shaping pulses of radiation detectors into a true gaussian form," *Journal of Instrumentation*, vol. 14, no. 01, p. P01004, 2019. 28

[203] G. Zeng, J. Yang, T. Hu, L. Ge, X. Ouyang, Q. Zhang, and Y. Gu, "Baseline restoration technique based on symmetrical zero-area trapezoidal pulse shaper," *Nuclear Instruments and Methods in Physics Research Section A: Accelerators, Spectrometers, Detectors and Associated Equipment*, vol. 858, pp. 57–61, 2017. 28

[204] S. Saxena and A. I. Hawari, "Investigation of FPGA-based real-time adaptive digital pulse shaping for high-count-rate applications," *IEEE Transactions on Nuclear Science*, vol. 64, no. 7, pp. 1733–1738, 2017. 28

[205] J. Wang, X. Luo, X. Wei, R. Zheng, C. Feng, and Y. Hu, "Design of a low-noise, high-linearity, readout ASIC for CdZnTe-based gamma-ray spectrometers," *Nuclear Instruments and Methods in Physics Research Section A: Accelerators, Spectrometers, Detectors and Associated Equipment*, vol. 988, p. 164927, 2021. 28

[206] P. Grybos, M. Idzik, K. Swientek, and P. Maj, "Integrated charge sensitive amplifier with pole-zero cancellation circuit for high rates," in *IEEE International Symposium on Circuits and Systems*, 2006, pp. 4–pp. 28, 40

[207] C. Zhao, Z. Wang, M. Zhao, and C. Yang, "Characteristics and comparison of two digital quasi-gauss filters for gamma spectroscopy," *Journal of Instrumentation*, vol. 16, no. 01, p. P01021, 2021. 28

[208] S. Saxena and A. I. Hawari, "Digital pulse deconvolution with adaptive shaping for real-time high-resolution high-throughput gamma spectroscopy," *Nuclear Instruments and Methods in Physics Research Section A: Accelerators, Spectrometers, Detectors and Associated Equipment*, vol. 954, p. 161288, 2020. 28

[209] C. Liu, X. Luo, R. Zheng, J. Wang, X. Wei, F. Xue, and Y. Hu, "A low noise APD readout ASIC for electromagnetic calorimeter in hiepa," *Nuclear Instruments and Methods in Physics Research Section A: Accelerators, Spectrometers, Detectors and Associated Equipment*, vol. 985, p. 164686, 2021. 28

[210] M. Carminati, D. Di Vita, L. Buonanno, G. L. Montagnani, and C. Fiorini, "A lightweight SiPM-based gamma-ray spectrometer for environmental monitoring with drones," in *International Conference on Applications in Electronics Pervading Industry, Environment and Society*, 2020, pp. 55–61. 28

[211] Y. Tang, R. Zhang, and J. Chen, "A low-power 16-channel SiPM readout front-end with a shared SAR ADC in 180 nm CMOS," in *International Conference on Solid-State & Integrated Circuit Technology* , 2020, pp. 1–3. 28

[212] H. Zhang, H. Xu, Y. Fan, X. Xing, H. Liu, and J. Wu, "A time-interleaved pipelined ADC with ultra high speed sampling," *Sādhanā*, vol. 45, no. 1, pp. 1–8, 2020. 28

[213] H. Wang, J. Liu, H. Zhang, H. Liang, and B. Ye, "Multiple time-over-threshold readout electronics for fast timing and energy resolving in a SiPM-based positron annihilation lifetime spectrometer," *Journal of Instrumentation*, vol. 15, no. 11, p. P11006, 2020. 28

[214] M.-D. Zhu, X. Qin, L. Wang, W.-Z. Zhang, Y. Lin, X. Rong, and J. Du, "A time-to-digital-converter utilizing bits-counters to decode carry-chains and dsp48e1 slices in a field-programmable-gate-array," *Journal of Instrumentation*, vol. 16, no. 02, p. P02009, 2021. 28

[215] J.-F. Pratte, F. Nolet, S. Parent, F. Vachon, N. Roy, T. Rossignol, K. Deslandes, H. Dautet, R. Fontaine, and S. A. Charlebois, "3d photon-to-digital converter for radiation instrumentation: Motivation and future works," *Sensors*, vol. 21, no. 2, p. 598, 2021. 28

[216] S. Gundacker and A. Heering, "The silicon photomultiplier: fundamentals and applications of a modern solid-state photon detector," *Physics in Medicine & Biology*, vol. vol. 65, no. 17, p. 17TR01, 2020. 28

[217] M. N. Ullah, J. H. Park, E. Pratiwi, G. B. Kim, and J.-Y. Yeom, "Wavelength discrimination (WLD) detector optimization for time-of-flight positron emission tomography with depth of interaction information," *Nuclear Instruments and Methods in Physics Research Section A: Accelerators, Spectrometers, Detectors and Associated Equipment*, vol. 982, p. 164498, 2020. 29

[218] I. Kipnis, T. Collins, J. DeWitt, S. Dow, A. Frey, A. Grillo, R. Johnson, W. Kroeger, A. Leona, L. Luo *et al.*, "A time-over-threshold machine: the readout integrated circuit

for the babar silicon vertex tracker," *IEEE Transactions on Nuclear Science*, vol. 44, no. 3, pp. 289–297, 1997. 30

[219] T. Orita, K. Shimazoe, and H. Takahashi, "The dynamic time-over-threshold method for multi-channel APD based gamma-ray detectors," *Nuclear Instruments and Methods in Physics Research Section A: Accelerators, Spectrometers, Detectors and Associated Equipment*, vol. 775, pp. 154–161, 2015. 30

[220] M. Saukoski, L. Aaltonen, K. Halonen, and T. Salo, "Fully integrated charge sensitive amplifier for readout of micromechanical capacitive sensors," in *IEEE International Symposium on Circuits and Systems*, 2005, pp. 5377–5380. 30, 38, 40

[221] J. Huizenga, S. Seifert, F. Schreuder, H. Van Dam, P. Dendooven, H. L ohner, R. Vinke, and D. Schaart, "A fast preamplifier concept for SiPM-based time-of-flight PET detectors," *Nuclear Instruments and Methods in Physics Research Section A: Accelerators, Spectrometers, Detectors and Associated Equipment*, vol. 695, pp. 379–384, 2012. 31, 41

[222] A. Ulyanov, O. Morris, L. Hanlon, S. McBreen, S. Foley, O. J. Roberts, I. Tobin, D. Murphy, C. Wade, N. Nelms *et al.*, "Performance of a monolithic LaBr3: Ce crystal coupled to an array of silicon photomultipliers," *Nuclear Instruments and Methods in Physics Research Section A: Accelerators, Spectrometers, Detectors and Associated Equipment*, vol. 810, pp. 107–119, 2016. 32

[223] C. Lavelle, W. Shanks, C. Chiang, M. Nichols, J. Osborne Jr, A. Herschelman, B. Brown, and M. Cho, "Approaches for single channel large area silicon photomultiplier array readout," *AIP Advances*, vol. 9, no. 3, p. 035123, 2019. 32

[224] G. Cozzi, P. Busca, M. Carminati, C. Fiorini, G. L. Montagnani, F. Acerbi, A. Gola, G. Paternoster, C. Piemonte, V. Regazzoni *et al.*, "High-resolution gamma-ray spectroscopy with a SiPM-based detection module for 1" and 2" LaBr 3: Ce readout," *IEEE Transactions on Nuclear Science*, vol. 65, no. 1, pp. 645–655, 2017. 32

[225] M. Ren, J. Zhou, B. Song, C. Zhang, M. Dong, and R. Albarracín, "Towards optical partial discharge detection with micro silicon photomultipliers," *Sensors*, vol. 17, no. 11, p. 2595, 2017. 38, 41, 47

[226] F. Corsi, M. Foresta, C. Marzocca, G. Matarrese, and A. Del Guerra, "BASIC: An 8-channel front-end ASIC for silicon photomultiplier detectors," in *IEEE Nuclear Science Symposium Conference*, 2009, pp. 1082–1087. 38, 40, 41, 43

[227] M. Trovato, J. Barrio, P. Botas, J. Cabello, J. Gillam, C. Lacasta, J. Oliver, M. Rafecas, C. Solaz, P. Solevi *et al.*, "Development of a three layer compton telescope prototype based on continuous LaBr 3 crystals and silicon photomultipliers," in *IEEE Nuclear Science Symposium and Medical Imaging Conference*, 2013, pp. 1–3. 38, 43

[228] F. Corsi, A. Argentieri, M. Foresta, C. Marzocca, G. Matarrese, and A. Del Guerra, "Front-end electronics for silicon photo-multipliers coupled to fast scintillators," in *IEEE Nuclear Science Symposuim & Medical Imaging Conference*, 2010, pp. 1332–1339. 38, 43

[229] A. Tao and T. Farncombe, "Investigating silicon photomultipliers for use in a gamma camera," in *IEEE Nuclear Science Symposium Conference*, 2011, pp. 3372–3377. 38, 43

[230] C. Lavelle, D. Raimi-Zlatic, J. Kalter, C. Chiang, T. Haard, and B. Fisher, "Sensitivity of silicon photomultipliers to direct gamma ray irradiation," *IEEE Transactions on Nuclear Science*, vol. 67, no. 1, pp. 389–399, 2019. 38, 43

[231] A. Nassalski, M. Moszynski, A. Syntfeld-Kazuch, T. Szczesniak, L. Swiderski, D. Wolski, T. Batsch, and J. Baszak, "Silicon photomultiplier as an alternative for APD in PET/MRI applications," in *IEEE Nuclear Science Symposium Conference*. IEEE, 2008, pp. 1620–1625. 38, 43

[232] S. Callier, F. Dulucq, R. Fabbri, C. de La Taille, B. Lutz, G. Martin-Chassard, L. Raux, and W. Shen, "Silicon photomultiplier integrated readout chip (SPIROC) for the ILC:

measurements and possible further development," in *IEEE Nuclear Science Symposium Conference*. IEEE, 2009, pp. 42–46. 38, 63

[233] C. de La Taille, G. Martin-Chassard, L. Raux *et al.*, "FLC- SIPM: Front-end chip for SIPM readout for ILC analog HCAL," in *International Linear Collider Workshop-Stanford, USA 2005*, 2005. 38

[234] S. Blin, P. Barrillon, and C. de La Taille, "Maroc, a generic photomultiplier readout chip," *Journal of Instrumentation*, vol. vol. 5, no. 12, p. C12007, 2010. 38

[235] M. Ippolitov, V. Lebedev, V. Manko, Y. G. Sibiriak, A. Akindinov, A. Vodopyanov, N. Gorbunov, S. Zaporozhets, P. Nomokonov, and I. Rufanov, "The use of silicon photomultipliers for improving the time resolution of an electromagnetic calorimeter based on lead tungstate crystals," *Instruments and Experimental Techniques*, vol. 60, no. 1, pp. 28–34, 2017. 38

[236] A. Jamil, T. Ziegler, P. Hufschmidt, G. Li, L. Lupin-Jimenez, T. Michel, I. Ostrovskiy, F. Retière, J. Schneider, M. Wagenpfeil *et al.*, "VUV-sensitive silicon photomultipliers for xenon scintillation light detection in nEXO," *IEEE Transactions on Nuclear Science*, vol. 65, no. 11, pp. 2823–2833, 2018. 38, 43

[237] F. Corsi, M. Foresta, C. Marzocca, G. Matarrese, and A. Del Guerra, "A self-triggered CMOS front-end for silicon photo-multiplier detectors," in *International Workshop on Advances in sensors and Interfaces*. IEEE, 2009, pp. 79–84. 38, 43

[238] P. Kmon, G. Deptuch, F. Fahim, P. Grybos, P. Maj, R. Szczygiel, and T. Zimmerman, "Active feedback with leakage current compensation for charge sensitive amplifier used in hybrid pixel detector," *IEEE Transactions on Nuclear Science*, vol. 66, no. 3, pp. 664–673, 2019. 38, 39

[239] R. Bassini, C. Boiano, and A. Pullia, "A low-noise charge amplifier with fast rise time and active discharge mechanism," *IEEE Transactions on Nuclear Science*, vol. 49, no. 5, pp. 2436–2439, 2002. 38, 39

[240] M. Manghisoni, D. Comotti, L. Gaioni, L. Ratti, and V. Re, "Dynamic compression of the signal in a charge sensitive amplifier: Experimental results," *IEEE Transactions on Nuclear Science*, vol. 65, no. 1, pp. 636–644, 2018. 38

[241] R. R. Harrison and C. Charles, "A low-power low-noise CMOS amplifier for neural recording applications," *IEEE Journal of solid-state circuits*, vol. 38, no. 6, pp. 958–965, 2003. 39

[242] E. Alnasser, "A novel low output offset voltage charge amplifier for piezoelectric sensors," *IEEE Sensors Journal*, vol. 20, no. 10, pp. 5360–5367, 2020. 39

[243] P. Giannelli, G. Calabrese, G. Frattini, M. Granato, and L. Capineri, "A buffered single-supply charge amplifier for high-impedance piezoelectric sensors," *IEEE Transactions on Instrumentation and Measurement*, vol. 68, no. 2, pp. 368–376, 2018. 39

[244] S. Capra and A. Pullia, "Design and experimental validation of an integrated multichannel charge amplifier for solid-state detectors with innovative spectroscopic range booster," *IEEE Transactions on Nuclear Science*, vol. 67, no. 8, pp. 1877–1884, 2020. 39

[245] M. Manghisoni, D. Comotti, L. Gaioni, L. Ratti, and V. Re, "Dynamic compression of the signal in a charge sensitive amplifier: Experimental results," *IEEE Transactions on Nuclear Science*, vol. 65, no. 1, pp. 636–644, 2017. 39

[246] S. Jeong, D. Shin, and J. Kim, "A transformer-isolated common-mode active emi filter using a low-cost BJT amplifier with feedforward structure," in *International Conference on Power Electronics and ECCE Asia*, 2019, pp. 2088–2094. 39

[247] D. J. Comer and D. T. Comer, "Bipolar junction transistor amplifiers." *In Fundamentals of Circuits and Filters,*, 2018. 39

[248] P. Durdaut, V. Penner, C. Kirchhof, E. Quandt, R. Kn ochel, and M. H oft, "Noise of a SPIROC charge amplifier for piezoelectric sensors," *IEEE Sensors Journal*, vol. 17, no. 22, pp. 7364–7371, 2017. 39

[249] G. Scandurra, G. Giusi, and C. Ciofi, "Single SPIROC front-end amplifier for low frequency noise measurements with cross correlation-based gain calibration," *Electronics*, vol. 8, no. 10, p. 1197, 2019. 39

[250] Z. He, C. Wang, G. Fan, Y. Zhou, and Y. Yang, "Design of a high input impedance OPA with Bi-SPIROC technology," in *IEEE International Conference on Electronics Technology* , 2019, pp. 233–236. 39

[251] K. Kasinski and R. Kleczek, "A flexible, low-noise charge-sensitive amplifier for particle tracking application," in *International Conference Mixed Design of Integrated Circuits and Systems*. IEEE, 2016, pp. 124–129. 40

[252] M. Manghisoni, D. Comotti, L. Gaioni, L. Ratti, and V. Re, "Dynamic compression of the signal in a charge sensitive amplifier: From concept to design," *IEEE Transactions on Nuclear Science*, vol. 62, no. 5, pp. 2318–2326, 2015. 40

[253] M. Manghisoni, L. Ratti, V. Re, V. Speziali, G. Traversi, and G. Fallica, "Gamma-ray response of soi bipolar junction transistors for fast, radiation tolerant front-end electronics," *Nuclear Instruments and Methods in Physics Research Section A: Accelerators, Spectrometers, Detectors and Associated Equipment*, vol. 518, no. 1-2, pp. 477–481, 2004. 40

[254] T. D. England, "Silicon-germanium BiCMOS and silicon-on-insulator CMOS analog circuits for extreme environment applications," Ph.D. dissertation, Georgia Institute of Technology, 2014. 40

[255] F. Corsi, M. Foresta, C. Marzocca, G. Matarrese, and A. Del Guerra, "Experimental results from an analog front-end channel for silicon photomultiplier detectors," in *IEEE Nuclear Science Symposium Conference*, 2008, pp. 2010–2014. 40, 41

[256] M. Caccia, A. Bulgheroni, C. Cappellini, V. Chmill, M. Ramilli, and F. Risigo, "Response of silicon photo-multipliers to a constant light flux," *Nuclear Physics B-Proceedings Supplements*, vol. 197, no. 1, pp. 30–34, 2009. 41

[257] G. Barbarino, L. Campajola, R. de Asmundis, G. De Rosa, G. Fiorillo, P. Migliozzi, F. Barbato, C. Mollo, A. Russo, and D. Vivolo, "Proof of feasibility of the vacuum silicon photomultiplier tube (vsipmt)," *Journal of Instrumentation*, vol. 8, no. 04, p. P04021, 2013. 41

[258] A. Kryemadhi, L. Barner, A. Grove, J. Mohler, and A. Roth, "A LYSO crystal array readout by silicon photomultipliers as compact detector for space applications," *Nuclear Instruments and Methods in Physics Research Section A: Accelerators, Spectrometers, Detectors and Associated Equipment*, vol. 912, pp. 93–96, 2018. 41

[259] N. Eggert, "A measurement of the cosmic muon decoherence curve with silicon photomultipliers," *Methods of Experimental Physics, University of Minnesota.*, 2008. 41

[260] G. Barile, A. Leoni, L. Pantoli, L. Safari, and V. Stornelli, "A new vcii based low-power low-voltage front-end for silicon photomultipliers," in *International Conference on Smart and Sustainable Technologies*, 2018, pp. 1–4. 41, 47, 48

[261] L. Pantoli, G. Barile, A. Leoni, M. Muttillo, and V. Stornelli, "A novel electronic interface for micromachined Si-based photomultipliers," *Micromachines*, vol. 9, no. 10, p. 507, 2018. 41, 47, 48

[262] G. Zappalà, F. Acerbi, A. Ferri, A. Gola, G. Paternoster, V. Regazzoni, N. Zorzi, and C. Piemonte, "Study of the photo-detection efficiency of fbk high-density silicon photomultipliers," *Journal of Instrumentation*, vol. 11, no. 11, p. P11010, 2016. 41

[263] S. Cecchini, I. D'Antone, L. Degli Esposti, I. Lax, G. Mandrioli, N. Mauri, L. Pasqualini, L. Patrizii, M. Pozzato, G. Sirri *et al.*, "Test of scintillator bars coupled to silicon photomultipliers for a charged particle tracking device," *Nuclear Instruments and Methods in Physics Research Section A: Accelerators, Spectrometers, Detectors and Associated Equipment*, vol. 846, pp. 1–7, 2017. 41

[264] R. Zimmermann, F. Braun, T. Achtnich, O. Lambercy, R. Gassert, and M. Wolf, "Silicon photomultipliers for improved detection of low light levels in miniature near-infrared spectroscopy instruments," *Biomedical optics express*, vol. 4, no. 5, pp. 659–666, 2013. 41

[265] A. Pullia, "How to derive the optimum filter in presence of arbitrary noises, time-domain constraints, and shaped input signals: A new method," *Nuclear Instruments and Methods in Physics Research Section A: Accelerators, Spectrometers, Detectors and Associated Equipment*, vol. 397, no. 2-3, pp. 414–425, 1997. 42

[266] F. Zocca, A. Pullia, and G. Pascovici, "Design and optimization of low-noise wide-bandwidth charge preamplifiers for high purity germanium detectors," *IEEE Transactions on Nuclear Science*, vol. 55, no. 2, pp. 695–702, 2008. 47

[267] H. M. Ip, S. Thomas, M. Hart, M. Prydderch, and M. French, "A dynamic slew correction circuit for low noise silicon detector pre-amplifiers," *IEEE Transactions on Nuclear Science*, vol. 59, no. 3, pp. 642–646, 2012. 47

[268] M. V. Montenegro, "Front-end CMOS transimpedance amplifiers on a silicon photomultiplier resistant to fast neutron fluence," Ph.D. dissertation, University of Nevada, Las Vegas, 2020. 47

[269] T. L. Naing, T. O. Rocheleau, E. Alon, and C. T.-C. Nguyen, "A 78-microwatt GSM phase noise-compliant pierce oscillator referenced to a 61-MHz wine-glass disk resonator," in *Joint European Frequency and Time Forum & International Frequency Control Symposium* , 2013, pp. 562–565. 47

[270] S. Elsaegh, H. Zappe, Y. Manoli, H. Klauk, and U. Zschieschang, "A 1.6 $\mu$W tunable organic transimpedance amplifier for photodetector applications based on gain-boosted common-gate input stage and voltage-controlled resistor with $\pm 0.5\%$ nonlinearity," in *European Solid State Circuits Conference*, 2017, pp. 75–78. 47, 48

[271] D. C. Dias, F. S. de Melo, L. B. Oliveira, and J. P. Oliveira, "Regulated common-gate transimpedance amplifier for radiation detectors and receivers," in *International*

*Conference Mixed Design of Integrated Circuits and Systems*. IEEE, 2014, pp. 540–545. 48

[272] D. C. Dias, F. S. de Melo, L. B. Oliveira, and J. P. Oliveira, "Regulated common-gate transimpedance amplifier for radiation detectors and receivers," in *International Conference of Mixed Design Integrated Circuits and Systems* , 2014, pp. 540–545. 48

[273] A. Karimi-Bidhendi, H. Mohammadnezhad, M. M. Green, and P. Heydari, "A silicon-based low-power broadband transimpedance amplifier," *IEEE Transactions on Circuits and Systems I: Regular Papers*, vol. 65, no. 2, pp. 498–509, 2017. 48

[274] A. Guzinski, "Body-driven differential amplifier for application in continuous-time active-c filer," in *Proc. European Conf. Circuit Theory and Design*, 1987, pp. 315–320. 49

[275] D. Panchal and A. Naik, "0.25v bulk driven variable gain amplifier using g¡inf¿mb¡/inf¿/i¡inf¿drain¡/inf¿ method for ultra-low power low voltage biomedical applications," in *International Conference on Communication and Electronics Systems*, 2020, pp. 166–170. 49

[276] M. Kumngern, U. Torteanchai, S. Yutthanaboon, and F. Khateb, "Sub-volt bulk-driven transconductance amplifier and filter application," in *IEEE Asia Pacific Conference on Circuits and Systems*, 2018, pp. 1–4. 49

[277] Y.-T. Lin, W.-Y. Chung, D.-S. Wu, H.-C. Lin, and R. Lin, "A low voltage CMOS bandgap reference," in *IEEE-NEWCAS Conference*, 2005, pp. 227–230. 49

[278] X. Zhang and E. El-Masry, "A regulated body-driven CMOS current mirror for low-voltage applications," *IEEE Transactions on Circuits and Systems II: Express Briefs*, vol. 51, no. 10, pp. 571–577, 2004. 49

[279] J. Rosenfeld, M. Kozak, and E. G. Friedman, "A bulk-driven CMOS OTA with 68 dB DC gain," in *IEEE International Conference on Electronics, Circuits and Systems*. IEEE, 2004, pp. 5–8. 49

[280] G. Raikos and S. Vlassis, "Low-voltage bulk-driven input stage with improved transconductance," *International Journal of Circuit Theory and Applications*, vol. 39, no. 3, pp. 327–339, 2011. 53

[281] S. M. Chaudhry, U. M. Minhas, and F. Abbas, "A high gain, bulk driven operational transconductance amplifier (OTA) for wireless body area networks," *National Academy Science Letters*, vol. 41, no. 1, pp. 41–45, 2018. 57

[282] "MPPC S13360-6050CS — hamamatsu photonics: MPPC (SiPM) S13360-6050CS," https://www.hamamatsu.com/us/en/product/type/S13360-6050CS/index.html, (Accessed on 07/12/2020). 59, 64

[283] O. V. Dvornikov, N. N. Prokopenko, V. A. Tchekhovski, Y. D. Galkin, A. E. Titov, and A. V. Bugakova, "Silicon photomultipliers' analog interface with wide dynamic range," in *IEEE East-West Design & Test Symposium*. IEEE, 2019, pp. 1–4. 63

[284] M. D'Incecco, C. Galbiati, G. K. Giovanetti, G. Korga, X. Li, A. Mandarano, A. Razeto, D. Sablone, and C. Savarese, "Development of a very low-noise cryogenic preamplifier for large-area SiPM devices," *IEEE Transactions on Nuclear Science*, vol. 65, no. 4, pp. 1005–1011, 2018. 63

[285] H. Su, H. Wang, T. Xu, and R. Zeng, "Effects of forward body bias on high-frequency noise in 0.18$\mu$m CMOS transistors," *IEEE Transactions on Microwave Theory and Techniques*, vol. 57, no. 4, pp. 972–979, 2009. 65

[286] M. S. A. Shawkat, M. H. U. Habib, and N. McFarlane, "An analog CMOS silicon photomultiplier using perimeter-gated single-photon avalanche diodes," *IEEE Transactions on Circuits and Systems I: Regular Papers*, vol. 65, no. 11, pp. 3830–3841, 2018. 69

[287] A. Burger, E. Rowe, M. Groza, K. Morales Figueroa, N. J. Cherepy, P. R. Beck, S. Hunter, and S. A. Payne, "Cesium hafnium chloride: A high light yield, non-hygroscopic cubic crystal scintillator for gamma spectroscopy," *Applied Physics Letters*, vol. 107, no. 14, p. 143505, 2015. 70

[288] R. Král, P. Zemenová, V. Vaněček, A. Bystřickỳ, M. Kohoutková, V. Jarỳ, S. Kodama, S. Kurosawa, Y. Yokota, A. Yoshikawa *et al.*, "Thermal analysis of cesium hafnium chloride using DSC–TG under vacuum, nitrogen atmosphere, and in enclosed system," *Journal of Thermal Analysis and Calorimetry*, vol. 141, no. 3, pp. 1101–1107, 2020. 70

[289] T. S. Whiteside, A. D. Brand, T. J. Aucott, and D. P. DiPrete, "Improved field-portable system to measure CS-137 in wildlife," *Journal of Environmental Radioactivity*, vol. 223, p. 106394, 2020. 70

[290] M. Taggart, J. Henderson, J. O'Neill, and P. Sellin, "Fast-neutron response of the novel scintillator caesium hafnium chloride," *Nuclear Instruments and Methods in Physics Research Section A: Accelerators, Spectrometers, Detectors and Associated Equipment*, p. 165224, 2021. 75

[291] E. Rowe, W. Goodwin, P. Bhattacharya, G. Cooper, N. Schley, M. Groza, N. Cherepy, S. Payne, and A. Burger, "Preparation, structure and scintillation of cesium hafnium chloride bromide crystals," *Journal of Crystal Growth*, vol. 509, pp. 124–128, 2019. 75

# Vita

Shahram Hatefi Hesari received his BS in Electronics-Control Engineering from Shiraz University in 2008. Then he completed his MS in Electrical Engineering from Amirkabir University (Tehran Poly Technique) in 2011. His research interests include semiconductor fabrication, integrated circuit fabrication, and sensor design.